UNIVERSIDAD DE CÓRDOBA

EIDA3 - Ingeniería Agraria, Alimentaria, Forestal y del Desarrollo Rural Sostenible

TESIS **DOCTORAL**

MODELIZACIÓN DE LA DERIVA DE SENSORES TERMOGRÁFICOS EMBARCADOS EN UAV PARA UN MANEJO EFICIENTE DEL RIEGO. MODELLING THE DRIFT OF THERMOGRAPHIC SENSORS UAV FOR EFFICIENT IRRIGATION MANAGEMENT

Directores:

D. Alfonso García-Ferrer Porras

D. Francisco Javier Mesas Carrascosa

Fernando Juan Pérez Porras

Marzo 2021

TITULO: *MODELIZACIÓN DE LA DERIVA DE SENSORES TERMOGRÁFICOS EMBARCADOS EN UAV PARA UN MANEJO EFICIENTE DEL RIEGO*

AUTOR: *Fernando Juan Pérez Porras*

Campus de Rabanales
Ctra. Nacional IV, Km. 396 A
14071 Córdoba

https://www.uco.es/ucopress/index.php/es/
ucopress@uco.es

TÍTULO DE LA TESIS: MODELIZACIÓN DE LA DERIVA DE SENSORES TERMOGRÁFICOS EMBARCADOS EN UAV PARA UN MANEJO EFICIENTE DEL RIEGO.

DOCTORANDO/A: Fernando Juan Pérez Porras

1 INFORME RAZONADO DEL/DE LOS DIRECTOR/ES DE LA TESIS

Dr. ALFONSO GARCÍA-FERRER, Catedrático del Departamento de Ingeniería Gráfica y Geomática, y **FRANCISCO JAVIER MESAS CARRASCOSA**, Profesor Titular del Departamento de Ingeniería Gráfica y Geomática, pertenecientes a la Universidad de Córdoba, directores de la presente tesis doctoral

INFORMAN:

Que la investigación desarrollada por **D. Fernando Pérez Porras**, bajo la dirección de **los Doctores Alfonso García-Ferrer** y **Francisco Javier Mesas Carrascosa**, ha sido desarrollada con éxito y alcanzando los objetivos inicialmente propuestos.

Publicaciones científicas

1. Mesas-Carrascosa, F. J., Pérez-Porras, F., Meroño de Larriva, J. E., Mena Frau, C., Agüera-Vega, F., Carvajal-Ramírez, F., ... & García-Ferrer, A. (2018). Drift correction of lightweight microbolometer thermal sensors on-board unmanned aerial vehicles. Remote Sensing, 10(4), 615; https://doi.org/10.3390/rs10040615.

   Datos de 2018 (JCR): índice de impacto 4.118, índice de impacto de los últimos 5 años 4.740 y 1er cuartil en el área temática en el área temática de Remote Sensing

2. Mesas-Carrascosa, F. J., Pérez Porras, F., Triviño-Tarradas, P., Meroño de Larriva, J. E., & García-Ferrer, A. (2019). Project-based learning applied to unmanned aerial systems and remote sensing. Remote Sensing, 11(20), 2413; https://doi.org/10.3390/rs11202413.

   Datos de 2019 (JCR): índice de impacto 4.509, índice de impacto de los últimos 5 años 5.001 y 2º cuartil en el área temática en el área temática de Remote Sensing

3. Mesas-Carrascosa, F. J., Pérez Porras, F., Triviño-Tarradas, P., García-Ferrer, A., & Meroño-Larriva, J. E. (2020). Effect of lockdown measures on atmospheric nitrogen dioxide during SARS-CoV-2 in Spain. Remote Sensing, 12(14), 2210; https://doi.org/10.3390/rs12142210.

   Datos de 2019 (JCR): índice de impacto 4.509, índice de impacto de los últimos 5 años 5.001 y 2º cuartil en el área temática en el área temática de Remote Sensing

Otras aportaciones destacables que han surgido de la presente tesis doctoral en revistas indexadas son:

1. Mesas-Carrascosa, F. J., Verdú Santano, D., **Pérez Porras, F.**, Meroño-Larriva, J. E., & García-Ferrer, A. (2017). The development of an open hardware and software system onboard unmanned aerial vehicles to monitor concentrated solar power plants. Sensors, 17(6), 1329.

Datos de 2017 (JCR): índice de impacto 2.475, índice de impacto de los últimos 5 años 3.014 y 2º cuartil en el área temática en el área temática de Instruments & Instrumentarion.

2. Martínez-Carricondo, P., Agüera-Vega, F., Carvajal-Ramírez, F., Mesas-Carrascosa, F. J., García-Ferrer, A., & **Pérez-Porras, F. J.** (2018). Assessment of UAV-photogrammetric mapping accuracy based on variation of ground control points. International journal of applied earth observation and geoinformation, 72, 1-10.

   Datos de 2018 (JCR): índice de impacto 4,846, índice de impacto de los últimos 5 años 5.194 y 1er cuartil en el área temática en el área temática de Remote Sensing.

3. Agüera-Vega, F., Carvajal-Ramírez, F., Martínez-Carricondo, P., López, J. S. H., Mesas-Carrascosa, F. J., García-Ferrer, A., & **Pérez-Porras, F. J.** (2018). Reconstruction of extreme topography from UAV structure from motion photogrammetry. Measurement, 121, 127-138.

   Datos de 2018 (JCR): índice de impacto 2.791, índice de impacto de los últimos 5 años 2.826 y 2º cuartil en el área temática en el área temática de Instruments & Instrumentarion

Por todo ello, se autoriza la presentación de la tesis doctoral.

Córdoba, a 19 de marzo de 2021

Firma de los directores

Firmado por GARCIA FERRER PORRAS ALFONSO - 30417127H el día 24/03/2021 con un certificado emitido por AC FNMT Usuarios

Firmado por MESAS CARRASCOSA FRANCISCO JAVIER - 26032358S el día 24/03/2021 con un certificado emitido por AC FNMT Usuarios

Fdo.: Alfonso García-Ferrer Porras Fdo.: F. Javier Mesas Carrascosa

Agradecimientos

En primer lugar, quiero agradecer a todos los que me han ayudado de forma desinteresada a la consecución de esta tesis doctoral que, aunque mía, también es un poquito de todos vosotros.

En especial quiero agradecérselo a mis directores de tesis, Alfonso García-Ferrer por su gran apoyo y Javier Mesas, Javi para los amigos. Amigos porque además de guiarme en la tesis durante el proceso de doctorando, me llevo un gran amigo para toda la vida, gracias Javi, sin ti todo esto y lo que nos queda sería imposible.

A todos los compañeros con los que he compartido el departamento de Ingeniería Gráfica y Geomática, Nacho, José Emilio, Isabel, Juanjo y Mara por haberme ayudado de una forma u otra a la consecución de los objetivos de la tesis.

A José Luis Sáiz, mi responsable en I+D en Babcock Fleet Management, por permitirme compatibilizar la Universidad con la empresa, generando una sinergia muy importante para todas las partes. Sin él no hubiera conseguido evolucionar hasta donde he llegado hoy.

A mi familia, en especial a mis padres Miguel y Fernanda y a mi hermano Miguel, que desde pequeño me han empujado a estudiar y superarme en cada momento y a levantarme cuando me he caído.

A mis sobrinos Miguel y África, por ser parte de la felicidad de la casa cuando todos estamos juntos y por intentar ser un referente para ellos en todo lo que puedo.

Por último, a Carmen, mi pareja y mi compañera por su nobleza, apoyo y ánimo incondicional no se puede medir, es incomparable. Gracias por darme todos los días esos empujoncitos necesarios y por tu comprensión, es imposible quererte más.

Gracias a todos una vez más.

PEREZ PORRAS FERNANDO JUAN - 77353123Y

Firmado digitalmente por PEREZ PORRAS FERNANDO JUAN - 77353123Y
Fecha: 2021.03.26 17:18:48 +01'00'

RESUMEN

El uso civil de plataformas aéreas no tripuladas ha experimentado un notable aumento en la última década, siendo la agricultura una de las áreas que mayor interés ha despertado. La flexibilidad que ofrecen estas plataformas, permitiendo realizar vuelos sobre el cultivo en el preciso momento de interés generando estudios multi-temporales con técnicas de teledetección de muy alta resolución espacial. Estas aplicaciones están siendo posibles por la miniaturización de sensores que hace posible embarcarlos como carga de pago en estas plataformas. De este modo los sensores registran información de los cultivos en distintas regiones del espectro electromagnético, que es procesada para aplicaciones de agricultura de precisión. En función del tipo de sensor, su uso presenta un mayor o menor grado de madurez, beneficiando o limitando su uso. En el caso del uso de sensores termográficos, su uso aparece más limitado a consecuencia de la tecnología empleada si bien despierta un elevado interés tanto para su aplicación en la detección de enfermedades o evaluación de estrés hídrico en cultivos. Los sensores termográficos de uso civil se basan en una tecnología de microbolómetros no refrigerados, la cual presenta cambios continuos en la medida de temperatura. Esta inestabilidad genera una deriva en la adquisición de los valores de temperatura que debe ser corregida. Se presenta un método que permite calcular la deriva de cualquier sensor termográfico en función del tiempo.

ABSTRACT

The civilian use of unmanned aerial platforms has experienced a remarkable interest in the last decade, with agriculture being one of the areas that has aroused most interest. The flexibility offered by these platforms, allowing flights over the crop at the precise moment of interest, makes it possible to carry out multi-temporal studies applying remote sensing techniques with very high spatial resolution. These applications are being made possible by the miniaturisation of sensors, which makes it possible to ship them as payloads on these platforms. In this way, sensors record crop information in different regions of the electromagnetic spectrum, which, once processed, are used in precision agriculture applications. Depending on the type of sensor, its use has a greater or lesser degree of maturity, benefiting or limiting its use. In the case of thermographic sensors, their use is more limited due to the technology used, although they are of great interest for their application in the

detection of diseases or the evaluation of water stress in crops. Thermographic sensors for civilian use are based on uncooled microbolometer technology, which shows continuous changes in temperature measurement. This instability generates a drift in the acquisition of temperature values that must be corrected. A method is presented that allows the drift of any thermographic sensor to be calculated as a function of time.

Índice

Índice de Figuras

2 INTRODUCCIÓN

2.1 Breve repaso de la teledetección.

Fotografía literalmente significa dibujar con luz. La historia de la teledetección comienza con la fotografía, con el primer sensor que se desarrolló y perfeccionó, requiriendo de un método permanente de fijación de la imagen, cuyo descubrimiento inicial fue realizado por Louis Daguerre en 1839 (Pollack & Grushkin, 1977). Su uso se extendió rápidamente por el mundo, lo que provocó un rápido avance tecnológico en cuanto a cámaras, lentes y procesado. Como resultado de estos avances, el tiempo de exposición fue recortado de los 30 minutos iniciales necesarios por el método inicial de Daguerre con el daguerrotipo a 1/1000 s en 1875. Ejemplo de estos avances fueron que pocos años después, en 1888, George Eastman introdujo ya el primer rollo de película y la primera cámara fotográfica de Kodac (Pollack & Grushkin, 1977).

El proceso inicial de revelar imágenes era muy complejo, las placas fotográficas y las películas sólo eran sensibles a algunas regiones visibles del espectro electromagnético, concretamente del azul y el verde del espectro visible, por ello una luz roja de seguridad se utilizaba en un cuarto oscuro para revelar las imágenes. Posteriormente los tintes durante el revelado se empezaron a usar para extender el rango del revelado al rojo e infrarrojo. Este hecho fue descubierto por Vogel of Berlin en 1873 (Neblette, 1970). Diez años después se detectó el límite de 1,3 μm de ancho de banda en el uso de las placas fotográficas, un límite existente hoy día para el revelado de imagen (Hudson, 1969). Así, la teoría del color fotográfica se comenzó a desarrollar en 1868 pero fue impracticable hasta 1930, cuando el proceso Kodachrome fue introducido para las películas(Pollack & Grushkin, 1977). No obstante, no era un proceso fácil lo cual provocó que no se extendiera su uso. Por lo tanto, hasta que no se desarrolló el proceso Ektachrome no se generalizó el uso de imágenes en color, en 1950 (Pollack & Grushkin, 1977). En este contexto, las películas pancromáticas, las cuales sí son sensitivas a todo el espectro visible, no fueron comerciales hasta 1905 (Neblette, 1970). Las películas blanco y negro con infrarrojo no se comercializaron hasta después de la segunda guerra mundial. Dichos hechos bélicos, han sido probablemente los que han generado unos avances más importantes en el sector de la teledetección.

Por otro lado, y no menos importante, el uso de plataformas aéreas para el registro de imágenes a fotointerpretar comenzaron con la necesidad de labores de inteligencia con fines militares en momento de guerra. Por ello, las grandes guerras han contribuido notablemente a importantes avances tecnológicos. Las primeras fotografías fueron tomadas por globos fijados a tierra en 1850, más adelante, en 1862, dichos globos serían usados por el ejército de Estados Unidos para fotografiar las defensas alrededor de Richmond, Virginia, durante la guerra de secesión (Avery, 1962). De forma análoga pero cambiando la plataforma, Willbur Wright hizo la primera fotografía desde una aeronave tripulada en 1909 (Colwell, 1960). La fotografía aérea y la fotointerpretación fueron una práctica común que se generalizó durante la primera guerra mundial. Durante la guerra, se diseñaron cámaras instaladas en aeronaves las cuales operaban de forma independiente al vuelo, permitiendo a los pilotos centrarse en las maniobras de vuelo y mientras tanto las cámaras, de forma autónoma, capturaban datos de forma constante. Estas cámaras solían estar instaladas en la zona ventral apuntando hacia el terreno de forma cenital. Ejemplo de esto se puede encontrar en el uso realizado por las fuerzas aéreas francesas, llegando a procesar 10.000 imágenes diarias (Colwell, 1960). Por otro lado, en 1918, durante la primera guerra mundial, fotointérpretes estadounidenses detectaron e identificaron un 90% de las instalaciones alemanas gracias a esta tecnología (Colwell, 1960). Todos estos avances en el ámbito militar se trasladaron posteriormente a la sociedad civil, tanto en aplicaciones comerciales como científicas alrededor de 1930. Prueba de ello son las numerosas publicaciones científicas sobre fotointerpretación realizadas en 1940 en los ámbitos de la ecología, arqueología, geología, forestal, ingeniería o geografía (Colwell, 1960).

El segundo gran estímulo para la fotografía aérea y fotointerpretación se produjo durante la segunda guerra mundial. Gracias a la información que capturaban las cámaras aerotransportadas, se extendió su uso masivo por las fuerzas aéreas estadounidenses llegando a capturar más de 171 millones de negativos durante la segunda guerra mundial (Infield, 1970). En paralelo, el origen de la teledetección no fotográfica se desarrollaría también durante este evento bélico, siendo los principales desarrollos los relacionados con tecnología radar, sistemas termográficos y sónar.

Con todo esto, algunos investigadores a partir de ese momento reconocieron el potencial de estos sistemas aplicados a problemas del ámbito civil; celebrándose el primer Simposio Internacional sobre Teledetección del Medio Ambiente en la Universidad de Michigan en 1962, incluyendo ponencias sobre materiales relacionadas con la geofísica, termografía o imágenes radar (Moore, 1979). Dentro de este primer grupo

de investigadores que fueron pioneros en detectar las utilidades y aplicaciones civiles por este tipo de sensores destaca Robert Colwell, de la Universidad de California, Berkley, desarrollando soluciones para el ámbito agrícola y forestal. Este investigador llegó a realizar 400 publicaciones sobre teledetección ambiental y junto a David Simonett, el cual lideraría la edición de la revista Remote Sensing of Environment.

2.2 Primeros programas de teledetección de apoyo a la agricultura

En 1957, representantes de la industria química requirieron a *Agricultural Board of the National Research Council* soluciones para, de una forma más exacta, disponer de más información para detectar y evaluar la incidencia relacionada con plagas en cultivos agrícolas y zonas forestales que esos momentos asolaban a los Estados Unidos, generando cuantiosas pérdidas, fijadas por el Departamento de Agricultura y Forestal de los Estados Unidos (USDA) entorno a unos 7.000 millones de dólares anuales aproximadamente de la época. Esto desencadenó que la *Agricultural Board of the National Research Council* recomendara la formación de un comité de Teledetección agrícola para estudiar el uso potencial de sensores embarcados en plataformas aéreas entre los años 1957 y 1965, formado por científicos referentes en el sector de la botánica, ingeniería, estadística, física, silvicultura o economía (Sigafoos, 1970). Uno de las conclusiones de este comité fue poner en órbita plataformas espaciales para de observación de la Tierra, coincidiendo con el Año Geofísico Internacional (Acker et al., 2014) y que el presidente de los Estados Unidos Dwight Eisenhower fue quién lo anunció. Así, este comité consideró emplear todo tipo de sensores que dispusieran de longitudes de onda capaces de atravesar la atmosfera y capturar información relevante para la agricultura. Además, se establecieron las líneas estratégicas para el desarrollo de la teledetección, como el procesado bruto de datos, el reconocimiento de patrones, radiometría o el desarrollo del sector aeroespacial (Macdonald, 1984).

Inicialmente, los primeros estudios se enfocaron en la vegetación de grandes regiones para detectar brotes de estrés, controlar la propagación de las plagas y evaluar los daños, generando procesados automatizados en cada hito de la solución. Además, con datos proporcionados por sensores termográficos se detectarían áreas donde la vegetación aparecía gravemente estresada (Macdonald, 1984). Así, las aplicaciones agroforestales fueron creciendo desde 1960 a la par del desarrollo de nuevos sensores o mejora de los ya existentes en cuanto a resolución temporal, espacial o espectral.

Con estas plataformas espaciales se mantenía el mismo objetivo que con las plataformas aéreas tripuladas durante la guerra: embarcar una carga de pago que capturara datos georreferenciados sobre la Tierra. A diferencia de éstas últimas, la monitorización de la Tierra desde el espacio sería constante, lo que permitiría estudios multitemporales en grandes extensiones de terreno. La observación sistemática de la Tierra desde el espacio comenzó con el satélite TIROS-I, satélite meteorológico con una cámara de televisión embarcada que permitía a meteorólogos distinguir entre nubes, agua, hielo y nieve (Krueger & Fritz, 1961). Este satélite sería posteriormente rebautizado como NOAA en 1970, cuyo nombre y familia de satélite continua actualmente capturando datos desde el espacio.

No sería hasta el inicio del programa de observación de la Tierra Landsat donde las técnicas de Teledetección tuvieron un gran impacto en áreas como la agricultura, geología, minería o forestal. La plataforma LANDSAT I, equipada con un sensor Multispectral Scanner, formalmente llamado ERST, ofrecería datos a modo de escenas multiespectrales por primera vez y una vídeo cámara en el espectro visible e infrarrojo. Así, el programa Landsat sería el primero de una gran constelación de satélites que se han ido enviando constantemente al espacio para la captura de datos en diferentes rangos del espectro electromagnético, y de gran utilidad para el ámbito agroforestal. Fruto del desarrollo tecnológico, Landsat 3 ya disponía de bandas en el rango de espectro electromagnético correspondiente al rojo, verde, infrarrojo cercano e Infrarrojo de onda larga (Haack, 1982). Posteriormente en 1982, la puesta en servicio de Landsat 4 contaría con los sensores Multiespectral Scanner (MSS) y Thematic Mapper ™, de mucha utilidad para el sector agroforestal (Williams, Goward, & Arvidson, 2006). Entre las bondades de las plataformas espaciales respecto a las aeronaves tripuladas se encontraba poder contar con una cobertura global de forma repetitiva; con una visión sinóptica y resumida uniforme en el tiempo y abarcando grandes superficies, ofreciendo datos multiespectrales en formato digital con un coste económico más reducido. De este modo, inicialmente se identificaron por parte Chuck Paul en 1978, responsable de teledetección de la Agencia Internacional para el desarrollo (AID), ocho herramientas agroforestales a desarrollar con técnicas de teledetección (Haack, 1982): 1) cartografía de inventarios nacionales, 2) seguimiento de los bosques y deforestación, 3) planificación a futuro de los usos del suelo, 4) identificación de recursos acuícolas, 5) invasión de las zonas urbanas en tierras agrícolas, 6) planificación del transporte, 7) utilidad de la tierra y 8) cartografía de las capacidades de los suelos. En la Tabla 1 se muestra de forma resumida, en función de las plataformas y tipo

de carga de pago embarcada, la evolución temporal del tipo de aplicaciones desarrolladas en el sector agrícola.

Año	Aeronave tripulada	Media resolución	Alta resolución	Ultra resolución	Sensores activos	Sensor
1956	Cartografía en cualquier rango				Cartografía con RADAR, Cartografía con SLAR	**Imagen Aérea**
1972	Radar	Cartografía extensiva para producción y monitoreo			Cartografía con SAR	**1972 LANDSAT**
1975		Detección de cambios, usos del suelo				**LANDSAT 2**
1978		Detección regadíos, superficie, evaluación de plagas				**LANDSAT 3**
1982-84		Detección de sequías, monitoreo cambio climático				**LANDSAT 4-5**
1985		Mapping LAI				**1985 SPOT**
1998		Cartografía temática verificada				
1999	Biomasa					**1999 IKONOS**
2000						**2000 MODIS**

2001	Invasión urbana en tierras agrícolas	Mapeado especies LAI Agua subterránea Plagas			**2001 QuickBird**
2007		Aplicaciones para pequeños agricultores en el ámbito de la producción, tratamientos y fertilizantes		Mapping LiDAR	**2007 WorldView**
2009			Revisión diaria para estudios multi-temporales con 2 m^2/píx		**WordView2**
2012					**Gaofen**
2014				Biofísica	**WorldView 3**
2015			Detección de malas hierbas y agricultura de precisión	Estructura, biomasa.	**Sentinel**

Tabla 1 Evolución temporal de las aplicaciones agrícolas de las técnicas de Teledetección

2.3 Dificultades del uso de Teledetección en el sector agroforestal

Desde un principio, el principal objetivo de la Teledetección ha sido alertar de forma rápida y exacta ante la presencia de afecciones, plagas y/o enfermedades en el ámbito agroforestal. No obstante, la Teledetección aplicada como recurso para agricultores generó ciertas dudas en un primer momento, especialmente por la dificultad de disponer de datos en tiempo real. Además, la tecnología de computación en los años 60 no estaba demasiado avanzada para procesar grandes volúmenes de datos. Como resultado de este retraso en el acceso a los datos y o la información por parte de los agricultores junto con no poder contar con estos en una venta temporal de interés provocó que la Teledetección no fuera tan atractiva en un primer momento en este campo de aplicación. La consecuencia directa es que la Teledetección empezó a ponerse en duda como ayuda para los sistemas expertos de toma de decisiones en el ámbito agrícola, ya que los insumos se retrasaban mucho desde la captura de los datos. De hecho, las primeras referencias a los sensores de Landsat 5 siempre hacían hincapié en los mercados agrícolas o intereses por parte de grandes extensiones agrícolas para los gobiernos, pero no para los propietarios (Jackson, 1984). A modo de ejemplo, cultivos de ciclo corto no podrían ser gestionados correctamente apoyados en datos o información de Teledetección decenas de días o incluso meses después, ya que esos retrasos no permitían margen para la toma de decisiones. En este contexto, el trabajo colaborativo entre investigadores y usuario final permitirían definir las características técnicas deseables que debería ofrecer un programa de observación de la Tierra de utilidad para este sector de la agricultura, destacando: a) la disponibilidad de los datos, siendo deseable minutos o incluso horas, b) la resolución temporal, para que los datos fueran útiles, en el 50% de los casos ésta debería ser menor a 5 días, sobre todo en aplicaciones de riego, c) la resolución espacial, siendo aceptable valores de 400 m2/pixel y resolución óptimos sobre 25 m2/pixel(Jackson, 1984), pensando principalmente en cultivos extensivos. Atendiendo a estos condicionantes, no sería hasta 1986 con el lanzamiento de SPOT-1, con una resolución espacial en modo pancromático igual a 10 metros y multiespectrales de 20 metros, cuando se comenzaría a tener una aproximación real a lo planteado por Jackson, siendo el principal problema la resolución temporal igual a 26 días, provocando que en años posteriores se pusieran en servicio las plataformas SPOT2- y SPOT-3 en los años 1990 y 1993 respectivamente, aumentando la resolución temporal. Aun así y pese a todos los avances tecnológicos, seguiría habiendo reticencia en su uso, principalmente debido a la resolución espacial, demandándose una resolución espacial igual a 10

metros con una frecuencia de paso mínima igual a 3 días, además de tener en cuenta que el coste económico fuera asumible para una explotación (Steven, 1993).

Para cumplir con las características que necesitaban los agricultores, como el aumento de resolución o el aumento de la periodicidad, muchos investigadores usaron técnicas para combinar distintos de programas de observación que permitieran aumentar la resolución espacial o espectral de dichos programas a partir de datos pancromáticos (Yesou, Besnus, Rolet, & sensing, 1993) o mezclando la periodicidad de varios sensores, técnica que todavía se mantiene en la actualidad (Skakun, Vermote, Roger, & Franch, 2017).

La mayoría de los requisitos que Jackson estableció, se cumplen actualmente con el programa Copérnico diseñado por la Agencia Espacial Europea (ESA). Para agricultura, el uso de Sentinel-2 se ha extendido en la actualidad ya que dispone de unas características de periodicidad (5 días), resolución (desde 10 hasta 60 metros) y espectral (12 bandas desde 0.43 hasta 12.51 μm) similares a las que Jackson ya estableció en 1984.

2.4 Sistemas aéreos no tripulados

Sin duda alguna los UAS han supuesto una auténtica revolución para la teledetección. Inicialmente, como con otras tecnologías de la Geomática, las primeras aplicaciones aparecieron inicialmente en el ámbito militar. Los UAS son sistemas compuestos por una plataforma aérea, autopiloto, comunicaciones, estación de control remota además de GPS e inerciales (Ilustración 1).

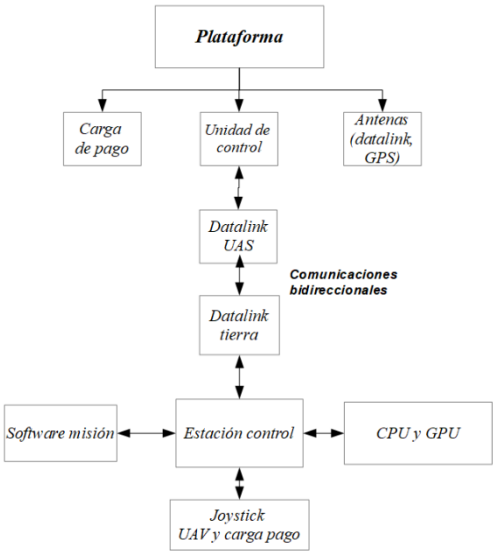

Ilustración 1: Arquitectura de un UAS

El primer programa militar que introdujo el desarrollo de un UAV fue el llamado AQM-91ª Compass arrow en Estados Unidos. El Compass Arrow (Ilustración 2) era una plataforma de 2400 kilogramos, con una carga de pago de más de 100 kilogramos y un techo de vuelo de 20 kilómetros que volaba 2 horas al límite de altura y con la máxima carga de pago (Papadales, Tibbetts, Schoenung, & Meier, 1993).

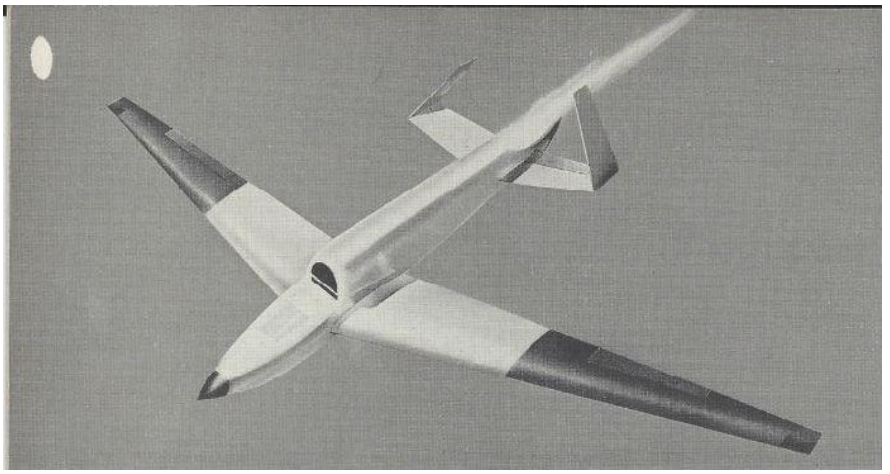

Ilustración 2: 3D del Compass Arrow UAS

Los UAV normalmente suelen ser clasificados por las características que definen su rendimiento, entre ellos cabe destacar el modo de despegue. Entre los distintos tipos de despegue se encuentran los de despegue vertical, horizontal o por el tipo de rotor ala rotatoria, multirotor o ala fija, entre otros Por otro lado, también podemos encontrar clasificaciones de UAV en función del tipo de alimentación (batería, combustión, hidrógeno), en función del tipo de misión (fotogrametría, observación, arma militar, transporte) , por el peso (>5kg, 5-25kg, 25-200kg, 200-2000kg ó >2000kg), o por la distancia y autonomía (<5 horas y <100km, 5-24 horas y 100-400km, > 24 horas y > 1500km)(Arjomandi, Agostino, Mammone, Nelson, & Zhou, 2006).

La teledetección agrícola no ha permanecido ajena al uso de UAS, permitiendo aumentar la resolución espacial hasta pocos cm/píxel, lo que permite abordar estudios a nivel de planta (Jurado, Ortega, Cubillas, & Feito, 2020) o malas hierbas (Peña, Torres-Sánchez, de Castro, Kelly, & López-Granados, 2013), permitiendo solventar dos de los principales problemas relativos a la resolución temporal y espacial. Sin duda, además de la plataforma UAV, dentro de un UAS el otro subsistema en orden de importancia es la carga de pago, presentando actualmente ciertos límites mecánicos y eléctricos comunes a cualquier plataforma no tripulada, siendo los principales peso, tamaño, alimentación y consumo, unidad de procesado y protección ambiental.

A nivel operacional, actualmente la legislación actual sobre aeronaves no tripuladas aprobada por la Agencia Estatal de Seguridad Aérea a través del Real Decreto 1036/2017 establece dos categorías de plataformas de

vuelo (AESA, 2017), aeronaves inferiores a 25 Kg y aeronaves mayores de 25 Kg. Para la operación con éstas últimas, se exige certificado de tipo o experimental, requisitos similares a los establecidos para una aeronave tripulada. Esto tipo de requisitos tan exigentes se deben al impacto en un accidente que pueden generar aeronaves superiores a 25 kg. Por ello, y sorteando estos requisitos operacionales tan exigentes, la mayoría de UAS usados en cartografía y teledetección se encuentran en el rango menor de 25 Kg, por facilidad documental, desarrollo, costes y justificación aeronáutica. Esto implica, que el peso del conjunto aeronave, comunicaciones, alimentación y carga de pago tienen un límite de peso muy bajo, lo que implica la miniaturización de los subsistemas y entre ellos la carga de pago.

2.5 Teledetección aplicada a la agricultura

La teledetección ofrece importantes ventajas en el campo de la investigación agronómica, destacando la clasificación de cultivo (Zheng, Myint, Thenkabail, Aggarwal, & Geoinformation, 2015) y su seguimiento y monitorización (Mateos, González-Dugo, Testi, & Villalobos, 2013). Por otro lado, permite la evaluación de rendimiento o producción de forma extensiva y cuantificada (Leslie, Servina, & Miller, 2017), ofreciendo ser una buena herramienta para ayuda a toma de decisiones (Jones & Barnes, 2000). Además, permite capturar mínimas variaciones de los cultivos debido a que éstos son muy vulnerables a variaciones del suelo (Sona et al., 2016), clima u otros cambios físico-químicos (Ballesteros et al., 2018). Por último, la aplicación de técnicas de teledetección permite aumentar y homogeneizar rendimientos de los cultivos (Sona et al., 2016) de forma que se aumenta la producción al tiempo que se reducen costes para grandes superficies (Khanal, Fulton, Shearer, & Agriculture, 2017; Potić, Bugarski, & Matić-Varenica, 2017).

2.5.1 Teledetección UAV

En cuanto a las principales funcionalidades que permite teledetección desde UAV se encuentran i) estimación de la superficie cultivo, clasificación del mismo, fenotipo o producción a nivel de planta (Yang et al., 2017), ii) control de la humedad del suelo, detección de estrés en cultivos, detección de enfermedades o plagas y la evaluación de la fertilidad del suelo (Bellvert, Zarco-Tejada, Girona, & Fereres, 2014) y por último, iii) control de malas hierbas, vigilancia de inundaciones, control de la erosión y monitorización de la cubierta vegetal (Peña et al., 2013).

Por otro lado, este tipo de teledetección con UAV volando a baja altura, máximo 120 metros sobre el terreno según la legislación actual, junto con el avance de los sensores actuales, ha permitido desarrollar una tecnología muy útil para la agricultura de precisión. La agricultura de precisión es una técnica de gestión de parcelas agrícolas basada en la variabilidad existente en las mismas y el manejo localizado de los inputs a partir de un listado de herramientas tecnológicas que permite monitorizar una parcela a nivel de píxel o parcela para mejorar la calidad y producción agrícola (Pierce & Nowak, 1999). La variabilidad espacial y temporal dentro de una misma parcela obliga a disponer de una resolución tal, que permita dar respuesta a esta variabilidad. Si no se dispone de esta resolución, se corre el riesgo de no dar una respuesta heterogénea de gestión de la parcela para generar una homogeneización en el crecimiento, producción, calidad o respuesta del cultivo.

2.6 Cargas de pago para plataformas no tripuladas. Teledetección aplicada a agricultura de precisión con UAV

2.6.1 Sensores RGB

Los sensores con respuesta en el espectro visible embarcadas en las plataformas aéreas no tripuladas suelen ofrecer la mayor resolución espacial, pudiendo ser implementados mediante dos tecnologías, Charge – coupled device (CCD) o Coplementary Metal Oxide Semiconductor (CMOS), pudiendo disponer unas u otras del método de captura rolling o global shutter. En los últimos tiempos los sensores CMOS han mejorado mucho las características respecto a los de tipo CCD en ruido y sensibilidad, siendo mejores en términos de bajo consumo, bajos niveles de alimentación y bajo coste.

En general, para cartografía o teledetección desde un UAV lo ideal es trabajar con sensores global shutter CMOS, que no presenta un coste demasiado elevado y ofrecen un resultado óptimo con un menor consumo (Bigas, Cabruja, Forest, & Salvi, 2006). Por otro lado, los sensores CMOS pueden utilizar focales con monturas fijas tipo C o micro 4/3, lo que permite ir adaptando la focal de forma remota en función de la resolución objetivo en cada momento. Esto puede ayudar en gran medida a mantener la resolución durante el vuelo, es decir, si el autopiloto del UAV no varía su posición respecto al terreno en tiempo real se puede mantener variando la focal en tiempo real de la cámara.

Dentro de la categoría de sensores pasivos, este tipo de sensores son los que disponen de una mejor calidad geométrica en comparación con los distintos sensores del rango del espectro electromagnético, por lo que es aconsejable a partir de ellos calcular cualquier producto que sea independiente del espectro, como modelos de elevaciones o superficies (Moravec et al., 2017).

Este tipo de sensores se usan para generar ortomosaico (Ilustración 3: Ortomosaico de ensayo de olivar), modelos digitales del elevaciones o de superficies (Remondino et al., 2011), delimitación de cultivos(Moravec et al., 2017), mapeado de recursos naturales (Carfagna & Gallego, 2005; Verbyla, 1995), fotointerpretación (Carfagna & Gallego, 2005), detección de caminos y carreteras (Mokhtarzade & Zoej, 2007), cubicación de movimiento de tierras o erosión del terreno(ULVİ & Geosciences, 2018), delimitación a nivel de planta o detección de malas hierbas (Torres-Sánchez, López-Granados, De Castro, & Peña-Barragán, 2013).

Ilustración 3: Ortomosaico de ensayo de olivar

2.6.2 Sensores multiespectrales

Este tipo suelen disponer de sensores CMOS con distintos filtros calibrados para registrar la reflectancia espectral en un rango del espectro electromagnético concreto, realizando su elección en función de la aplicación a desarrollar. De hecho, no es extraño encontrar sensores CMOS para las que se ha diseñado una rueda con distintos filtros que van girando y capturando datos en el rango del espectro en cada momento que le interese al usuario con un reducido coste económico (Morales et al., 2020).

La mayoría de estos sensores suelen disponer de filtros para aplicaciones agrícolas que cubren la región del espectro electromagnético entre 0,4 y 0,9 μm (Ilustración 4:). Además, es posible emplear sensores que recogen datos en otros rangos del espectro infrarrojo un poco más alto, denominados Short Wave Infrared (SWIR), los cuales registran datos desde 0,9 hasta 3 μm (Saari et al., 2011), de gran utilidad en agricultura para aplicaciones relacionadas con estrés hídrico (Ghulam et al., 2008) o contenido de nitrógeno (Herrmann, Karnieli, Bonfil, Cohen, & Alchanatis, 2010).

Ilustración 4: Imagen multiespectral capturada durante un incendio donde se aprecian diferentes contenidos de humedad

Por lo general, los sensores multiespectrales se utilizan para detectar en la vegetación variables como la vigorosidad de la planta, clorofila, índice de área foliar, daños por plagas o enfermedades, detección de estrés, determinación del tipo de suelo y pigmentos fotosintéticos, o cuantificación de la fertirrigación (Wójtowicz, Wójtowicz, Piekarczyk, & Science, 2016). Respecto a los sensores SWIR, las principales aplicaciones se centran en la predicción del estrés del cultivo y el contenido de nitrógeno en plantas, perjudicial para el ser humano (Camino et al., 2018).

2.6.3 Sensores hiperespectrales

Se clasifican normalmente en función del tipo de captura, que puede ser de barrido de línea o de área (Adão et al., 2017). Por un lado, las cámaras de barrido van realizando escaneos línea a línea o punto a punto, para luego generar en la fase de post-procesado un cubo hiperpespectral georreferenciado. Por otro lado, las cámaras de área realizan las capturas como su propio nombre indica, capturando todos los píxeles en un mismo momento, pudiendo disponer de un sensor rolling o global shutter.

Este tipo de sensores, particularmente las de barrido, necesitan de una unidad inercial muy precisa y correctamente calibrada que permita posteriormente, cuando se genera el cubo hiperespectral, la unión correcta de todas las líneas de barrido para formar el cubo hiperespectral (Adão et al., 2017). Así, es de gran importancia, sobre todo para agricultura de precisión, que estos sensores dispongan de unidades inerciales de gran precisión que permita la correcta generación de ortomosaicos hiperespectrales correctamente georreferenciados.

En general, en esta tipología de sensores, las de tipo barrido suelen disponer de un número de bandas espectrales mayor que las de tipo área. Para capturar un gran número de bandas espectrales se hace necesario las captura por barrido por una limitación estrictamente tecnológica, las comunicaciones del sensor hacia la unidad de procesamiento interna. Este tipo de comunicaciones comúnmente se realizan por Gigabit Ethernet (GigE), lo cual limita el ancho de banda a 1 Gbps. Esta limitación en las comunicaciones provoca que cuando se desean almacenar las tramas de la sensorización, no se puedan almacenar imágenes muy pesadas junto con muchas bandas espectrales, ya que los datos capturados pasarían de 1 Gbps de peso y no podrían llegar a la unidad de procesamiento. Actualmente, a las comunicaciones internas en las cámaras se les está incorporando fibra, sobre todo en visión artificial, lo cual permitirá en el futuro aumentar el ancho de banda del flujo de datos, lo que permitirá aumentar el número de bandas espectrales capturadas en las cámaras de área (Li, 2016).

En cuanto a las aplicaciones agrarias a partir de la captura de datos hiperespectrales se encuentran el cálculo de nitrógeno en planta (Näsi et al., 2018), contenido de carotenos en viñedo (Jeziorska, 2019; Zarco-Tejada et al., 2013), determinación de las características hidrológica de la superficie del cultivo (Jeziorska, 2019), predicción de riegos y estrés hídrico (Albornoz & Giraldo, 2017; Zarco-Tejada, González-Dugo, & Berni, 2012), detección o estudio de enfermedades como Verticillium en Olivo(Zarco-Tejada et al.,

2012) o determinación de clorofila y pigmentos fotosintéticos (Adão et al., 2017; Calderón, Navas-Cortés, & Zarco-Tejada, 2015).

2.6.4 Sensores radar de apertura sintética

Los radares de apertura sintética son sensores activos capaces de penetrar sobre la vegetación en función de la frecuencia del espectro en la que se dispongan los filtros, centrados en las frecuencias microondas. Este tipo de radares disponen de grandes antenas que emiten pulsos, calculando el retardo de los ecos, lo que les permite determinar la distancia una vez reflejado el pulso sobre la superficie. Al ser sensores activos, no necesitan fuentes de iluminación, por lo que pueden capturar datos tanto de día como de noche.

La principal característica de estos sensores es la alta resolución de la que se dispone en la dirección del movimiento del sensor mediante la síntesis de una antena de grandes dimensiones a partir de una pequeña, esta característica es la que impone su nombre a estos sensores.

En una imagen SAR lo que se aprecia son intensidades que dependen del tipo de reflectividad del objeto, en función de si la superficie es rugosa o plana. La reflectividad son los datos que se almacenan en las polarizaciones, ya que, como cualquier onda microondas, disponen de una polarización. En general, los mejores sensores son los que disponen de mayores polarizaciones disponibles. Lo ideal siempre es disponer de cuatro polarizaciones Horizontal-Horizontal, Horizontal-Vertical, Vertical-Vertical, Vertical-Horizontal.

La mayoría de sensores SAR, se centran en la banda X que va desde 8 a 12 Ghz, C de 4 a 8 Ghz o L, de 1 a 2 Ghz. En general, las frecuencias de mayor poder de penetración son las de menor longitud de onda, como la banda P centrada estas entre 450 y 900 Mhz (Schmullius & Evans, 1997), muy utilizada para funcionalidades forestales debido a que estas masas tienen una gran fracción de cabida cubierta (Ilustración 5).

Ilustración 6: Sensorización con radar de apertura sintética en banda X desde UAS

La mayoría de las aplicaciones agrícolas de estos sensores se centran en estudios sobre la humedad del suelo o tipo de suelo(Lyalin, Biryuk, Sheremet, Tsvetkov, & Prikhodko, 2018). Esto es debido a su poder de penetración a través de la vegetación y debido a la reflectividad medida que depende del tipo de suelo. Este tipo de características de los radares de apertura sintética permiten obtener datos hidrológico e hidromorfológicos de los suelos o determinar distintos tipos de suelos o su nivel de humedad(Lyalin et al., 2018).

2.6.5 LiDAR

Los sensores LiDAR (Light Detection And Ranging) son sistemas que están compuestos por una unidad láser, una unidad inercial, un sistema GNSS y una unidad de procesamiento. El sistema láser suele ser un sistema con dos espejos que envía pulsos para los que se mide su tiempo de retorno, lo que permite calcular distancia. Esta distancia unida a los datos GNSS e inerciales, permite generar una estructura de puntos en 3D (Ilustración 7:), llamada nube de puntos (Shan & Toth, 2018).

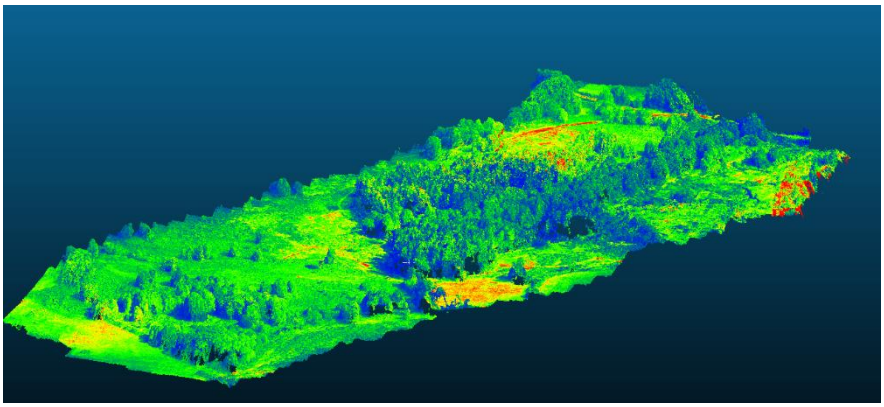

Ilustración 7: Nube de puntos 3D capturada por un sensor LiDAR

La penetración del sensor LiDAR depende de la frecuencia de emisión de los pulsos del láser, variando entre 100 y 1000 Khz, es decir, desde cien mil hasta un millón de medidas por segundo. La penetración también depende de los ecos del sensor por cada pulso. En el ámbito agrícola con sensores sencillos que permitan configuraciones hasta 100 Khz y 2 ó 3 (Lin & Habib, 2021) ecos por pulso es suficiente para la caracterización de cultivos mientras que, para aplicaciones forestales, es necesario configurar los sensores desde 500 Khz para fracciones de cabida cubierta altas con distintos estratos y hasta 5 ó 6 ecos por pulso (Jakubowski, Guo, & Kelly, 2013). La mayoría de los datos LiDAR se utilizan para el generación de modelos digitales del superficiies y elevaciones, permitiendo además calcular la estructura vertical de la vegetación (Zimble et al., 2003). Además, permiten realizar clasificaciones de usos del suelo (Mesas-Carrascosa, Castillejo-González, de la Orden, & Porras, 2012), detección para la digitalización de infraestructuras como caminos (Buján, Guerra-Hernández, González-Ferreiro, & Miranda, 2021), ríos (Bowen & Waltermire, 2002) o cuencas hidrológicas(Barber, Shortridge, & Science, 2005). Por otro lado, permiten calcular biomasa, estructura de la vegetación o cálculos precisos de erosión del terreno o seguimiento de cultivos mecanizados (Lin & Habib, 2021; Zhou et al., 2020). Por lo general, las mejores aplicaciones agrícolas se obtienen añadiendo a los datos LiDAR textura capturada con sensores multiespectrales, termográficos o hiperespectrales (Bradbury et al., 2005).

2.6.6 Sensores para medición de temperaturas

Existen dos categorías, radiométricas y no radiométricas, operando en distintos rangos del espectro, Medium Wave Infrared (MWIR), de 3,5 a 5 μm y Long Wave Infrarred, de 7,5 a 13,5 μm. Las temperaturas que miden

estos sensores se obtienen a través de la radiación de onda que emiten los objetos en el espectro infrarrojo. Esta radiación es emitida por los cuerpos debido a que se encuentran a una temperatura superior al cero absoluto, 0 grados kelvin (Speakman & Ward, 1998). Estos sensores, bien de MWIR o bien LWIR, a diferencia de los de tipo multiespectral poseen, para realizar las mediciones de temperatura, un bolómetro, el cual tiene la posibilidad de estar refrigerado por criogenización. Las cámaras en el rango MWIR son las que disponen de este tipo de bolómetro refrigerado, por lo que presentan un mayor peso que las de tipo LWIR, que suelen disponer de bolómetro no refrigerado.

El funcionamiento de un bolómetro se basa en tres fenómenos físicos i) la radiación del entorno, ii) la transferencia de calor dentro de las partes sólidas de esta y iii) la conservación de las corrientes eléctricas (Thomas, Crompton, & Koppenhoefer, 2015). El funcionamiento del bolómetro principalmente se modela mediante el acoplamiento de la transferencia de calor y la corriente eléctrica. Los bolómetros que funcionan con temperaturas criogénicas y por tanto constantes, pueden ser más sensibles y con mediciones más fiables que los que no lo son (J. Thomas & AltaSim Technologies, 2015).

El uso potencial de la teledetección termográfica en agricultura incluye la supervisión y programación del riego, detección de enfermedades en plantas que causen estrés, estimación del rendimiento de la fruta, evaluación de la madurez de la fruta o detección de magulladuras y golpes en frutas y verduras (Ishimwe, Abutaleb, & Ahmed, 2014).

Los sensores MWIR y LWIR se diferencian a su vez entre sensores térmicos y termográficos. Los primeros son sensores que sólo disponen de bolómetro y que traducen la diferencia de temperaturas irradiada por los objetos en el infrarrojo a una imagen con una paleta de colores. Esta paleta de colores se asigna en función de la radiación o temperatura emitida por cada objeto.

A diferencia de los sensores térmicos, los de tipo termográfico disponen de un módulo calibrado radiométricamente, similar a una unidad de computación, que convierte los datos capturados por el bolómetro a valores radiométricos. Posteriormente, para convertir los datos radiométricos a reflectancia, es necesario realizar una conversión en función de la calibración del bolómetro con un cuerpo negro (Grimberg, 2012). Por tanto, a partir de una cámara termográfica se puede obtener, por un lado, los mismos resultados que una térmica si se integra la salida analógica y, por otro lado, a partir de la salida digital se pueden conseguir datos radiométricos que permiten al usuario disponer de la temperatura

por píxel (Ilustración 8). Estos píxeles una vez georreferenciados tras un vuelo de fotogrametría, permitirían una comparación multitemporal a diferencia de una cámara térmica.

Ilustración 8: Termografía sobre viñedos

Los sensores con bolómetro no refrigerado son más económicos y pequeños (Jensen, McKee, & Chen, 2014) que los refrigerados debido sobre todo a la implantación de una tecnología más sencilla, lo que ha desembocado en un uso más extendido de los mismos en aplicaciones de agricultura de precisión con UAV. En general este tipo de sensores con bolómetro no refrigerado son bastante precisos, con variaciones entre 30 y 50 mK, pero bastante inexactos, errando las medidas varios grados Celsius (Minkina & Dudzik, 2009). Este tipo de bolómetros al estar en contacto con el viento y el aire a diferentes temperaturas, van cambiando el valor de sus mediciones constantemente, ya que la electrónica está programada por sí sola a mantener una temperatura constante. Este principio se conoce como Non-Uniformity Correction (NUC) (Ibarra-Castanedo & Maldague, 2013) eliminando la necesidad de calibración constante al actualizar los coeficientes de corrección en función de los niveles de radiación de la escena (Olbrycht, Więcek, & De Mey, 2012), de este modo, se puede aplicar una compensación continua a las mediciones. Este principio provoca oscilaciones en la medición de temperatura que junto con la deriva térmica

provocada por el viento en contacto con el bolómetro que recibe el sensor mientras está embarcado en el UAV, genera mediciones inexactas. En conclusión, estos sensores miden muy bien valores de temperatura en relativo, pero no valores de temperatura absolutos, necesitando correcciones para compensar las derivas (Kelly et al., 2019). Así, para poder extender el uso de estas cámaras en agricultura de precisión mediante UAV, se hace indispensable realizar correcciones atmosféricas que permitan que las medidas realizadas por el sensor sean precisas y a la vez exactas. Este tipo de correcciones permitirán calcular índices de vegetación a partir de valores de temperatura, generalmente índices de estrés hídrico.

Esta aplicación directa de la termografía sobre el estrés de los cultivos y por tanto en el manejo eficiente del riego se debe a que, un indicador del estrés hídrico en los cultivos se basa en el cierre de los conductos estomáticos de la hoja. El cierre estomático inducido por el estrés hídrico reduce la tasa de transpiración, reduciendo así el enfriamiento por evaporación y aumenta la temperatura de las hojas, hecho que puede ser detectado por cámaras termográficas embarcadas en un UAV, lo que permite cuantificar el nivel de estrés y sus mitigaciones a través del riego (Berni, Zarco-Tejada, Sepulcre-Cantó, Fereres, & Villalobos, 2009).

Después de todas las funcionalidades citadas anteriormente, se aprecia que las tecnologías UAV están revolucionando la agricultura, apareciendo constantemente nuevos desarrollos y aplicaciones que permiten la toma de decisiones en días en lugar de semanas o meses, prometiendo una importante reducción de costes y un aumento de rendimiento. Estas decisiones permiten aplicar de forma eficaz los insumos agrícolas, apoyando los pilares de la agricultura de precisión. Estos pilares se centran en prácticas agrícolas adecuadas, lugar adecuado, momento oportuno y cantidades adecuadas y controladas.

Sin embargo, la proliferación de los UAV ha sido muy alta pero no así la explotación real de los vehículos no tripulados en agricultura inteligente, debido sobre todo a los retos a los que se enfrenta la selección y despliegue de las tecnologías, como por ejemplo los métodos de adquisición de datos o procesamiento de imágenes, que no siguen un flujo estandarizado en un área relativamente nueva. Por ello, en el ámbito de los UAV, sensores, termografía, etc. se hace necesario el establecimiento de unos flujos de trabajo que permitan en cualquier desarrollo ofrecer unos resultados óptimos y una aplicabilidad directa en el ámbito agrícola.

2.7 Bibliografía

1. Acker, J., Williams, R., Chiu, L., Ardanuy, P., Miller, S., Schueler, C., . . . Manore, M. (2014). Remote sensing from satellites.
2. Adão, T., Hruška, J., Pádua, L., Bessa, J., Peres, E., Morais, R., & Sousa, J. J. J. R. S. (2017). Hyperspectral imaging: A review on UAV-based sensors, data processing and applications for agriculture and forestry. *9*(11), 1110.
3. AESA. (2017). Real Decreto 1036/2017, de 15 de Diciembre, por el que se regula la utilización civil de las aeronaves pilotadas por control remoto.
4. Albornoz, C., & Giraldo, L. F. (2017). *Trajectory design for efficient crop irrigation with a UAV*. Paper presented at the 2017 IEEE 3rd Colombian Conference on Automatic Control (CCAC).
5. Arjomandi, M., Agostino, S., Mammone, M., Nelson, M., & Zhou, T. J. R. f. M. E. c., University of Adelaide, Adelaide, Australia. (2006). Classification of unmanned aerial vehicles.
6. Avery, T. E. (1962). *Interpretation of aerial photographs*. Retrieved from
7. Ballesteros, R., Ortega, J. F., Hernandez, D., Del Campo, A., Moreno, M. A. J. I. j. o. a. e. o., & geoinformation. (2018). Combined use of agro-climatic and very high-resolution remote sensing information for crop monitoring. *72*, 66-75.
8. Barber, C. P., Shortridge, A. J. C., & Science, G. I. (2005). Lidar elevation data for surface hydrologic modeling: Resolution and representation issues. *32*(4), 401-410.
9. Bellvert, J., Zarco-Tejada, P. J., Girona, J., & Fereres, E. J. P. a. (2014). Mapping crop water stress index in a 'Pinot-noir'vineyard: comparing ground measurements with thermal remote sensing imagery from an unmanned aerial vehicle. *15*(4), 361-376.
10. Berni, J., Zarco-Tejada, P., Sepulcre-Cantó, G., Fereres, E., & Villalobos, F. J. R. S. o. E. (2009). Mapping canopy conductance and CWSI in olive orchards using high resolution thermal remote sensing imagery. *113*(11), 2380-2388.
11. Bigas, M., Cabruja, E., Forest, J., & Salvi, J. J. M. j. (2006). Review of CMOS image sensors. *37*(5), 433-451.
12. Bowen, Z. H., & Waltermire, R. G. J. J. J. o. t. A. W. R. A. (2002). Evaluation of light detection and ranging (lidar) for measuring river corridor topography 1. *38*(1), 33-41.
13. Bradbury, R. B., Hill, R. A., Mason, D. C., Hinsley, S. A., Wilson, J. D., Balzter, H., . . . Bellamy, P. E. J. I. (2005). Modelling relationships between birds and vegetation structure using airborne LiDAR data: a review with case studies from agricultural and woodland environments. *147*(3), 443-452.
14. Buján, S., Guerra-Hernández, J., González-Ferreiro, E., & Miranda, D. J. R. S. (2021). Forest Road Detection Using LiDAR Data and Hybrid Classification. *13*(3), 393.
15. Calderón, R., Navas-Cortés, J. A., & Zarco-Tejada, P. J. J. R. S. (2015). Early detection and quantification of Verticillium wilt in olive using hyperspectral and thermal imagery over large areas. *7*(5), 5584-5610.

16. Camino, C., González-Dugo, V., Hernández, P., Sillero, J., Zarco-Tejada, P. J. J. I. j. o. a. e. o., & geoinformation. (2018). Improved nitrogen retrievals with airborne-derived fluorescence and plant traits quantified from VNIR-SWIR hyperspectral imagery in the context of precision agriculture. *70*, 105-117.
17. Carfagna, E., & Gallego, F. J. J. I. s. r. (2005). Using remote sensing for agricultural statistics. *73*(3), 389-404.
18. Colwell, R. J. A. S. o. P., Falls Church, Virginia. (1960). 1960, Manual of Photographic Interpretation.
19. Ghulam, A., Li, Z.-L., Qin, Q., Yimit, H., Wang, J. J. A., & Meteorology, F. (2008). Estimating crop water stress with ETM+ NIR and SWIR data. *148*(11), 1679-1695.
20. Grimberg, E. (2012). Radiometry using an uncooled microbolometer detector. In: Google Patents.
21. Haack, B. N. J. W. D. (1982). Landsat: A tool for development. *10*(10), 899-909.
22. Herrmann, I., Karnieli, A., Bonfil, D., Cohen, Y., & Alchanatis, V. J. I. J. o. R. S. (2010). SWIR-based spectral indices for assessing nitrogen content in potato fields. *31*(19), 5127-5143.
23. Hudson, R. D. (1969). *Infrared system engineering* (Vol. 1): Wiley-Interscience New York.
24. Ibarra-Castanedo, C., & Maldague, X. P. (2013). Infrared thermography. In *Handbook of technical diagnostics* (pp. 175-220): Springer.
25. Infield, G. B. (1970). *Unarmed and Unafraid, p. 6*. New York: Macmillan.
26. Ishimwe, R., Abutaleb, K., & Ahmed, F. J. A. i. r. S. (2014). Applications of thermal imaging in agriculture—A review. *3*(03), 128.
27. J. Thomas, J. S. C. a. K. C. K., & AltaSim Technologies, C., OH. (2015). Multiphysics Analysis of Infra Red Bolometer. *Proceedings of the 2015 COMSOL Conference*.
28. Jackson, R. D. (1984). *Remote sensing of vegetation characteristics for farm management.* Paper presented at the Remote Sensing: Critical Review of Technology.
29. Jakubowski, M. K., Guo, Q., & Kelly, M. J. R. S. o. E. (2013). Tradeoffs between lidar pulse density and forest measurement accuracy. *130*, 245-253.
30. Jensen, A. M., McKee, M., & Chen, Y. (2014). *Procedures for processing thermal images using low-cost microbolometer cameras for small unmanned aerial systems.* Paper presented at the 2014 IEEE Geoscience and Remote Sensing Symposium.
31. Jeziorska, J. J. R. S. (2019). UAS for wetland mapping and hydrological modeling. *11*(17), 1997.
32. Jones, D., & Barnes, E. J. A. S. (2000). Fuzzy composite programming to combine remote sensing and crop models for decision support in precision crop management. *65*(3), 137-158.
33. Jurado, J. M., Ortega, L., Cubillas, J. J., & Feito, F. J. R. S. (2020). Multispectral mapping on 3D models and multi-temporal monitoring for individual characterization of olive trees. *12*(7), 1106.
34. Kelly, J., Kljun, N., Olsson, P.-O., Mihai, L., Liljeblad, B., Weslien, P., . . . Eklundh, L. J. R. S. (2019). Challenges and best practices for deriving temperature data from an uncalibrated UAV thermal infrared camera. *11*(5), 567.

35. Khanal, S., Fulton, J., Shearer, S. J. C., & Agriculture, E. i. (2017). An overview of current and potential applications of thermal remote sensing in precision agriculture. *139*, 22-32.
36. Krueger, A. F., & Fritz, S. J. T. (1961). Cellular cloud patterns revealed by TIROS I. *13*(1), 1-7.
37. Leslie, C. R., Servina, L. O., & Miller, H. M. (2017). *Landsat and Agriculture: Case Studies on the Uses and Benefits of Landsat Imagery in Agricultural Monitoring and Production*: US Department of the Interior, US Geological Survey.
38. Li, J. J. O. (2016). A highly reliable and super-speed optical fiber transmission for hyper-spectral SCMOS camera. *127*(3), 1532-1545.
39. Lin, Y.-C., & Habib, A. J. R. S. o. E. (2021). Quality control and crop characterization framework for multi-temporal UAV LiDAR data over mechanized agricultural fields. *256*, 112299.
40. Lyalin, K. S., Biryuk, A. A., Sheremet, A. Y., Tsvetkov, V. K., & Prikhodko, D. V. (2018). *UAV synthetic aperture radar system for control of vegetation and soil moisture.* Paper presented at the 2018 IEEE Conference of Russian Young Researchers in Electrical and Electronic Engineering (EIConRus).
41. Macdonald, R. B. (1984). A summary of the history of the development of automated remote sensing for agricultural applications. *Transactions on Geoscience Remote Sensing*(6), 473-482.
42. Mateos, L., González-Dugo, M., Testi, L., & Villalobos, F. J. A. W. M. (2013). Monitoring evapotranspiration of irrigated crops using crop coefficients derived from time series of satellite images. I. Method validation. *125*, 81-91.
43. Mesas-Carrascosa, F. J., Castillejo-González, I. L., de la Orden, M. S., & Porras, A. G.-F. (2012). Combining LiDAR intensity with aerial camera data to discriminate agricultural land uses. *Computers*
44. *electronics in agriculture, 84*, 36-46.
45. Minkina, W., & Dudzik, S. (2009). *Infrared thermography: errors and uncertainties*: John Wiley & Sons.
46. Mokhtarzade, M., & Zoej, M. V. (2007). Road detection from high-resolution satellite images using artificial neural networks. *International journal of applied earth observation geoinformation, 9*(1), 32-40.
47. Moore, G. K. J. H. S. B. (1979). What is a picture worth? A history of remote sensing/Quelle est la valeur d'une image? Un tour d'horizon de télédétection. *24*(4), 477-485.
48. Morales, A., Guerra, R., Horstrand, P., Diaz, M., Jimenez, A., Melian, J., . . . Lopez, J. F. J. S. (2020). A Multispectral Camera Development: From the Prototype Assembly until Its Use in a UAV System. *20*(21), 6129.
49. Moravec, D., Komárek, J., Kumhálová, J., Kroulík, M., Prošek, J., & Klápště, P. J. A. R. (2017). Digital elevation models as predictors of yield: comparison of an UAV and other elevation data sources. *15*(1), 249-255.
50. Näsi, R., Viljanen, N., Kaivosoja, J., Alhonoja, K., Hakala, T., Markelin, L., & Honkavaara, E. J. R. S. (2018). Estimating biomass and nitrogen amount of barley

and grass using UAV and aircraft based spectral and photogrammetric 3D features. *10*(7), 1082.
51. Neblette, C. B. (1970). *Fundamentals of Photography*: Van Nostrand Reinhold.
52. Olbrycht, R., Więcek, B., & De Mey, G. J. A. O. (2012). Thermal drift compensation method for microbolometer thermal cameras. *51*(11), 1788-1794.
53. Papadales, B. S., Tibbetts, T. A., Schoenung, S. M., & Meier, W. R. (1993). *Remote sensing with high-altitude unmanned aerial vehicles.* Paper presented at the Airborne Reconnaissance XVII.
54. Peña, J. M., Torres-Sánchez, J., de Castro, A. I., Kelly, M., & López-Granados, F. J. P. o. (2013). Weed mapping in early-season maize fields using object-based analysis of unmanned aerial vehicle (UAV) images. *8*(10), e77151.
55. Pierce, F. J., & Nowak, P. J. A. i. a. (1999). Aspects of precision agriculture. *67*, 1-85.
56. Pollack, P., & Grushkin, P. (1977). *The picture history of photography: from the earliest beginnings to the present day*: Abrams New York.
57. Potić, I., Bugarski, M., & Matić-Varenica, J. (2017). *Soil moisture determination using remote sensing data for the property protection and increase of agriculture production.* Paper presented at the Worldbank conference on land and poverty", The World Bank, Washington DC.
58. Remondino, F., Barazzetti, L., Nex, F., Scaioni, M., Sarazzi, D. J. I. a. o. t. p., remote sensing, & sciences, s. i. (2011). UAV photogrammetry for mapping and 3d modeling–current status and future perspectives. *38*(1), C22.
59. Saari, H., Pellikka, I., Pesonen, L., Tuominen, S., Heikkilä, J., Holmlund, C., . . . Antila, T. (2011). *Unmanned Aerial Vehicle (UAV) operated spectral camera system for forest and agriculture applications.* Paper presented at the Remote Sensing for Agriculture, Ecosystems, and Hydrology XIII.
60. Schmullius, C., & Evans, D. J. I. J. o. R. S. (1997). Review article Synthetic aperture radar (SAR) frequency and polarization requirements for applications in ecology, geology, hydrology, and oceanography: A tabular status quo after SIR-C/X-SAR. *18*(13), 2713-2722.
61. Shan, J., & Toth, C. K. (2018). *Topographic laser ranging and scanning: principles and processing*: CRC press.
62. Sigafoos, R. S. (1970). Remote Sensing. With Special Reference to Agriculture and Forestry. National Research Council Committee on Remote Sensing for Agricultural Purposes. National Academy of Sciences, Washington, DC, 1970. xvi, 424 pp.+ plates. $12.95. NAS Publication No. 1723. In: American Association for the Advancement of Science.
63. Skakun, S., Vermote, E., Roger, J.-C., & Franch, B. J. A. g. (2017). Combined use of Landsat-8 and Sentinel-2A images for winter crop mapping and winter wheat yield assessment at regional scale. *3*(2), 163.
64. Sona, G., Passoni, D., Pinto, L., Pagliari, D., Masseroni, D., Ortuani, B., & Facchi, A. (2016). *UAV multispectral survey to map soil and crop for precision farming applications.* Paper presented at the Remote Sensing and Spatial Information Sciences Congress:

International Archives of the Photogrammetry Remote Sensing and Spatial Information Sciences Congress: 19 July.
65. Speakman, J. R., & Ward, S. J. Z.-J.-. (1998). Infrared thermography: principles and applications. *101*, 224-232.
66. Steven, M. (1993). Satellite remote sensing for agricultural management: Opportunities and logistic constraints. *Journal of photogrammetry Remote Sensing, 48*(4), 29-34.
67. Thomas, J., Crompton, J., & Koppenhoefer, K. (2015). *Multiphysics Analysis of Infra Red Bolometer.* Paper presented at the Proceedings of the 2015 COMSOL Conference in Boston, Boston, MA, USA.
68. Torres-Sánchez, J., López-Granados, F., De Castro, A. I., & Peña-Barragán, J. M. J. P. o. (2013). Configuration and specifications of an unmanned aerial vehicle (UAV) for early site specific weed management. *8*(3), e58210.
69. ULVİ, A. J. I. J. o. E., & Geosciences. (2018). Analysis of the utility of the unmanned aerial vehicle (Uav) in volume calculation by using photogrammetric techniques. *3*(2), 43-49.
70. Verbyla, D. L. (1995). *Satellite remote sensing of natural resources* (Vol. 4): CRC Press.
71. Williams, D. L., Goward, S., & Arvidson, T. (2006). Landsat. *Photogrammetric Engineering Remote Sensing, 72*(10), 1171-1178.
72. Wójtowicz, M., Wójtowicz, A., Piekarczyk, J. J. C. i. B., & Science, C. (2016). Application of remote sensing methods in agriculture. *11*(1), 31-50.
73. Yang, G., Liu, J., Zhao, C., Li, Z., Huang, Y., Yu, H., . . . Zhang, X. J. F. i. p. s. (2017). Unmanned aerial vehicle remote sensing for field-based crop phenotyping: current status and perspectives. *8*, 1111.
74. Yesou, H., Besnus, Y., Rolet, J. J. I. j. o. p., & sensing, r. (1993). Extraction of spectral information from Landsat TM data and merger with SPOT panchromatic imagery—a contribution to the study of geological structures. *48*(5), 23-36.
75. Zarco-Tejada, P. J., González-Dugo, V., & Berni, J. A. J. R. s. o. e. (2012). Fluorescence, temperature and narrow-band indices acquired from a UAV platform for water stress detection using a micro-hyperspectral imager and a thermal camera. *117*, 322-337.
76. Zarco-Tejada, P. J., Guillén-Climent, M. L., Hernández-Clemente, R., Catalina, A., González, M., Martín, P. J. A., & meteorology, f. (2013). Estimating leaf carotenoid content in vineyards using high resolution hyperspectral imagery acquired from an unmanned aerial vehicle (UAV). *171*, 281-294.
77. Zheng, B., Myint, S. W., Thenkabail, P. S., Aggarwal, R. M. J. I. J. o. A. E. O., & Geoinformation. (2015). A support vector machine to identify irrigated crop types using time-series Landsat NDVI data. *34*, 103-112.
78. Zhou, L., Gu, X., Cheng, S., Yang, G., Shu, M., & Sun, Q. J. A. (2020). Analysis of plant height changes of lodged maize using UAV-LiDAR data. *10*(5), 146.
79. Zimble, D. A., Evans, D. L., Carlson, G. C., Parker, R. C., Grado, S. C., & Gerard, P. D. J. R. s. o. E. (2003). Characterizing vertical forest structure using small-footprint airborne LiDAR. *87*(2-3), 171-182.

3 OBJETIVOS DE LA TESIS DOCTORAL

El principal objetivo de esta Tesis Doctoral es explorar y analizar el uso de sensores embarcados en plataformas espaciales y aéreas no tripuladas aplicando técnicas de Teledetección en distintos campos de actuación, desde la modelización del comportamiento del sensor durante el registro de datos hasta la generación de información de utilidad para la toma de decisiones, pasando por la formación y capacitación de profesionales en el manejo de estas tecnologías. Concretamente esta Tesis queda estructurada

Capítulo 1. Drift correction of lightweight microbolometer thermal sensors on-board unmanned aerial vehicles

En este capítulo se ha desarrollado una metodología que permita, a partir de la extracción de puntos de control en imágenes termográficas registradas por un sensor embarcado en una plataforma aérea no tripulada en la zonas de solape longitudinal y transversal durante la fase de aerotriangulación en el flujo de trabajo fotogramétrico, evaluar la deriva térmica del bolómetro producida en el sensor en función del tiempo. Una vez calculada esta deriva, se han desarrollado unos modelos que dan respuesta a esta deriva de la temperatura en función del tiempo, generando una nuevas imágenes termográficas corregidas de este efecto.

Capítulo 2. Project-based learning applied to unmanned aerial systems and remote sensing

El desarrollo de la tecnología de los vehículos aéreos no tripulados y la miniaturización de los sensores han cambiado la forma de utilizar la teledetección, popularizando esta disciplina en la agricultura de precisión. Además de la transferencia de estas tecnologías al sector productivo, no menos importante es su incorporación en la capacitación de ingenieros. En este capítulo se presenta como se ha introducido el uso de estas tecnologías en la formación de los alumnos de Master en Ingeniería Agronómica a través de la formación basada en proyectos.

Capítulo 3. Effect of lockdown measures on atmospheric nitrogen dioxide during SARS-CoV-2 in Spain

Debido a la pandemia producida por el virus SARS-CoV-2, la concentración de gases de efecto invernadero en la atmósfera ha disminuido notablemente, sobre todo durante el periodo de confinamiento de la población. En este capítulo, a través del uso de sensores embarcados

en la plataforma Sentinel-5P del programa de observación de la Tierra Copernicus de la Unión Europea se ha analizado esta reducción y su relación con la densidad de población en España.

4 CAPÍTULO 1

remote sensing

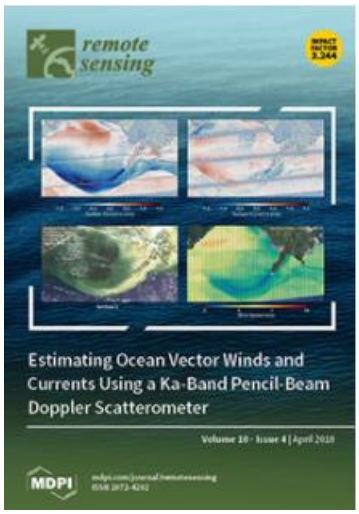

Open Access Article

Drift Correction of Lightweight Microbolometer Thermal Sensors On-Board Unmanned Aerial Vehicles

by Francisco-Javier Mesas-Carrascosa [1,*], Fernando Pérez-Porras [1], Jose Emilio Meroño de Larriva [1], Carlos Mena Frau [2], Francisco Agüera-Vega [3], Fernando Carvajal-Ramírez [3], Patricio Martínez-Carricondo [3] and Alfonso Garcia-Ferrer [1]

[1] Department of Graphic Engineering and Geomatics, University of Cordoba, Campus de Rabanales, 14071 Córdoba, Spain
[2] Departamento de Gestión Forestal Ambiental, University of Talca, 3460000 Talca, Chile
[3] Department of Engineering, University of Almería, La Cañada, 04120 Almería, Spain
* Author to whom correspondence should be addressed.

Remote Sens. **2018**, *10*(4), 615; https://doi.org/10.3390/rs10040615

Received: 23 March 2018 / Revised: 23 March 2018 / Accepted: 12 April 2018 / Published: 17 April 2018

(This article belongs to the Section Remote Sensing in Agriculture and Vegetation)

Publicado en **Remote Sensing**. 2018, 10(4), 615;

https://doi.org/10.3390/rs11202413

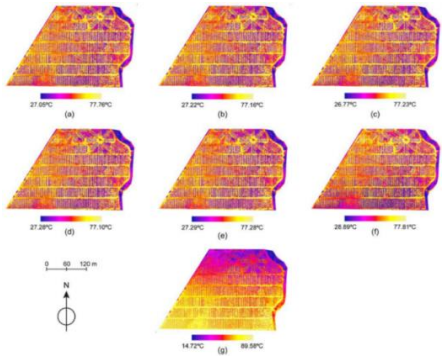

Article

Drift Correction of Lightweight Microbolometer Thermal Sensors On-Board Unmanned Aerial Vehicles

Francisco-Javier Mesas-Carrascosa [1,*], Fernando Pérez Porras [1], Jose Emilio Meroño de Larriva [1], Carlos Mena Frau [2], Francisco Agüera-Vega [3], Fernando Carvajal-Ramírez [3], Patricio Martínez-Carricondo [3] and Alfonso García-Ferrer [1]

[1] Department of Graphic Engineering and Geomatics, University of Cordoba, Campus de Rabanales, 14071 Córdoba, Spain; o12ppof@uco.es (F.P.P.); jemerono@uco.es (J.E.M.d.L.); agferrer@uco.es (A.G.-F.)
[2] Departamento de Gestión Forestal Ambiental, University of Talca, 3460000, Talca, Chile; cmena@utalca.cl
[3] Department of Engineering, University of Almeria, La Cañada, 04120 Almería, Spain; faguera@ual.es (F.A.-V.); carvajal@ual.es (F.C.-R.); pmc824@ual.es (P.M.-C.)
* Correspondence: fjmesas@uco.es; Tel.: +34-957-218-537

Received: 23 March 2018; Accepted: 12 April 2018; Published: date

1. **Abstract:** The development of lightweight sensors compatible with mini unmanned aerial vehicles (UAVs) has expanded the agronomical applications of remote sensing. Of particular interest in this paper are thermal sensors based on lightweight microbolometer technology. These are mainly used to assess crop water stress with thermal images where an accuracy greater than 1 °C is necessary. However, these sensors lack precise temperature control, resulting in thermal drift during image acquisition that requires correction. Currently, there are several strategies to manage thermal drift effect. However, these strategies reduce useful flight time over crops due to the additional in-flight calibration operations. This study presents a drift correction methodology for microbolometer sensors based on redundant information from multiple overlapping images. An empirical study was performed in an orchard of high-density hedgerow olive trees with flights at different times of the day. Six mathematical drift correction models were developed and assessed to explain and correct drift effect on thermal images. Using the proposed methodology, the resulting thermally corrected orthomosaics

yielded a rate of error lower than 1° C compared to those where no drift correction was applied.

Keywords: UAV; uncooled thermal sensor; precision agriculture; thermal orthomosaic

1. Introduction

World agriculture faces three major challenges that represent an apparent contradiction: to feed a growing population, to contribute to the reduction of rural poverty, and to manage the natural resource base [1,2]. Precision agriculture is believed to be an efficient method of crop production because it is accurate, inputs are optimized leading to reduced costs and environmental impact, and because it provides an audit trail that consumers and legislation require [3]. Precision agriculture emphasizes spatial-temporal data analysis and management jointly rather than singularly [4], as well as requiring a detailed description of canopy status and its variation in the field during the growth cycle [1].

Remote sensing methods have been demonstrated to be very useful in monitoring large areas while remaining cost effective [5]. Traditional remote sensing techniques have used manned aerial or satellite platforms to measure canopy reflectance in the electromagnetic spectrum range from 400 to 2500 nm [6]. These platforms have a temporal and spatial resolution that limits their utility in agriculture assessments due to the dynamic changes in crops in relation to the environment [7,8]. In recent years, unmanned aerial systems (UASs) have been used in a broad range of applications, including precision agriculture projects, principally because unmanned aerial vehicles (UAVs) have become more reliable, their performance (flight time, range) has improved, and the sensors have miniaturized [9]. Therefore, UAS technology allows for the possibility of acquiring information with high spatial and temporal resolution. In precision agriculture where analyses are performed of yield variation over a field and across years, half of the variation comes from year to year variation [10]. A well-timed sequence of UAV flights can contribute to the analyses of spatial and temporal variations.

A variety of sensors can be used as payload on board UAVs, ranging from Light Detection and Ranging system (LiDAR) [11,12], Red-Green-Blue (RGB) [13,14], multispectral [15,16], and hyperspectral [17,18] to thermal [19,20]. Infrared thermography allows users to monitor plant water status

for detecting stress or for applying deficit irrigation techniques [21], to monitor for infections [22], water stress detection [20,23] or for phenotyping plants [24,25].

To date, two different thermal systems are available: cooled and uncooled. The first, being very sensitive and highly accurate, are used on board satellite and aerial platforms. However, they are large, heavy, and power consuming. Uncooled thermal sensors are used as UAV payloads because they are smaller, lighter, and consume less power than cooled thermal sensors [26]. However, they are not as sensitive nor as accurate. Microbolometers are uncooled infrared radiation thermal sensors distributed in an array. Low values of noise-equivalent temperature difference (NETD) in uncooled thermal sensors, reaching 20 mK, have allowed their use in applications where only cooled thermal sensors were once suitable. However, temperature drift continues to be a disadvantage causing unwanted detector gain and offset non-uniformity in registered temperature data.

To combat this, a non-uniformity correction (NUC) is applied to remove noise using digital signal processing techniques on the detector output signal. It requires knowledge of coefficient corrections for every detector in the array [27]. For each detector in the array, a determined gain and offset is stored in the sensor. However, the change of the offset coefficient has to be updated due to the thermal drift effect. This temperature drift is principally caused by the detector's casing, which overheats and dissipates power and heat onto the detectors and electronic circuits. Hence, it is necessary to perform thermal drift correction and periodically update the correction values for each detector [28]. Without this correction, the temperature error would increase by approximately 0.7 °C per minute [29].

The most commonly used approach to compensate for thermal drift is shutter based [28,30]. Others have used a contact sensor between the detector matrix and the lens [31] or other locations inside the sensor [32], as well as "blind" pixels whose signal does not depend on the radiation of the observed scene [33]. Other types of NUCs are scene-based methods, which are divided into two categories: statistical [34] and registration-based methods [35].

Prior to flight, uncooled thermal sensors need to be stabilized after being switched on [36]. During this period, the absolute temperature progressively shifts until it is stabilized. As such, it is necessary to consider how environmental variables affect the registered temperature values, especially during a long acquisition period [37], and take into account wind

effect, varying cloud cover, position, and orientation of the sensor during the UAV flight. To remove thermal drift effects and simultaneously apply radiometric correction, some authors program UAV flights to cover ground targets with known temperatures. At the cost of useful UAV flight time, radiometric calibration coefficients are calculated so that the UAV can repeatedly fly over the nearest ground target and thus eliminate thermal drift [38,39].

The goal of this study was to determine a methodology using high spatial resolution thermal imagery acquired from a UAV while removing temperature drift independently of NUC applied by the sensor without any extra UAV flight operations. The specific objectives of this work were aimed at (i) modeling temperature drift effect; and the assessment of (ii) different drift models at (iii) different hours of the day.

2. Materials and Methods

The presented study was carried out in Córdoba, Spain (north latitude 37°56′05″, west longitude 4°42′59″, WGS 84) in June 2016, using a 10 ha orchard of high-density hedgerow olive trees (Olea europaea L. cv Arbequina). Figure 1 shows the development of olive trees during the growing season. Being a typical Mediterranean region, the climate is characterized by warm, dry summers and cool, wet winters with an average annual rainfall equal to 180 mm.

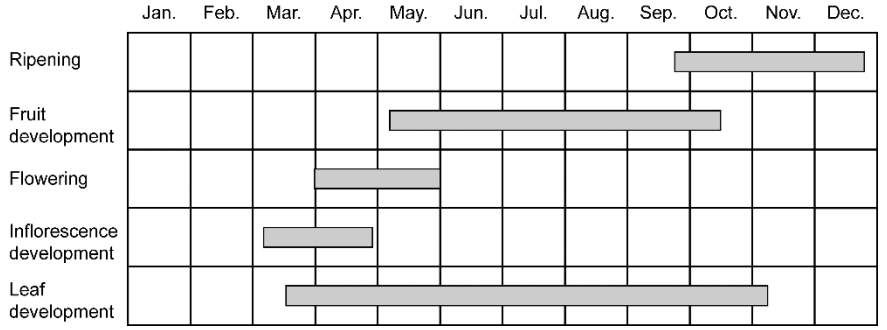

Figure 1. Development of olive trees during the growing season.

2.1. UAV Campaigns

The unmanned aerial vehicle (UAV) used was an MD4-1000 multi-rotor drone (Microdrones GmbH, Siegen, Germany). This UAV is a quadcopter with an entire carbon design. The system has a maximum payload equal to 1.2 kg. It uses 4 × 250 W gearless brushless motors and reaches a cruising speed of 15.0 m/s. The UAV was equipped with a Gobi 640-GiGe thermal sensor (Xenics nv, Leueven, Belgium), which is an uncooled long-wave infrared (LWIR) thermal sensor delivering raw digital images at 16 bits of sensor calibrated radiance with a dynamic range from −20 °C to 120 °C and a spectral resolution of 0.05 °C. It has a focal length equal to 18 mm and operates in a spectral band range from 8 μm to 14 μm. Registered images have a dimension equal to 640 × 480 pixels and a pixel pitch of 17 μm. Moreover, it has an onboard image processing system to perform a non-uniformity correction, an auto offset, and an auto gain. However, the continuous changing conditions in which the sensor operates cause temperature values to degrade throughout the UAV flight although the image processing system is operating. In this manuscript, the NUC has been deactivated, obtaining a set of images without any compensation. A stabilization procedure on the thermal sensor was conducted before each UAV flight as described in Berni et al. [36]. The thermal sensor was pre-heated for twenty minutes on field before each UAV flight to stabilize its

internal temperature. The sensor was connected to a stick PC Asus QM1 (Asustek Computer Inc., Taiwan, China) to store the images via an Ethernet port. Sensor weight totaled 710 g with flight duration equal to 20 min.

UAV flights were performed on 1 June 2016 at 120 m above ground level with a ground sample distance (GSD) equal to 11.3 cm (Figure 2). Side and forward lap settings were 80% and 70%, respectively, with 632 images registered. Five aluminum disks were placed on the plot as ground control points (GCPs), one in each corner and the other in the center of the study area. Because of the low emissivity of aluminum GCPs, they were visible in thermal images. Each GCP was measured with the stop-and-go technique through relative positioning by means of the NTRIP protocol (The Radio Technical Commission for Maritime Services, RTCM, for Networked Transfer via Internet Protocol) using two GNSS (global navigation satellite system) receivers. One of the receivers was a reference station for the GNSS Red Andaluza de Posicionamiento (RAP) network from the Institute for Statistics and Cartography of Andalusia, Spain, and the other, a Leica GS15 GNSS (Leica Geosystems AG, Heerbrugg, Switzerland), functioned as the rover receiver.

The UAV flew over the crop at 8:30, 12:30, 16:00, and 18:30 local time in clear skies. A Davis Vantage Pro2 weather station (Davis Instrument Corp., Hayward, CA, USA) was used to monitor climate conditions during the UAV flights. This weather station was equipped with a three-cup anemometer, an air temperature and humidity sensor, and a barometer. Table 1 shows air temperature, percentage of relative humidity, mean wind speed, and atmospheric pressure during each UAV flight on this date. These UAV flights were used to acquire thermal images of soil and crop under different atmospheric and temperature conditions.

Table 1. Atmospheric conditions for individual unmanned aerial vehicle (UAV) flights on 1 June 2016.

	UAV Flight (Local Time)			
	8:30	12:30	16:00	18:30
Air temperature (°C)	21	30	36	37
Relative humidity (%)	48	26	18	17
Mean wind speed (m/s)	2	3	6	6
Atmospheric pressure (hPa)	1022.6	1021.2	1018.4	1017.4

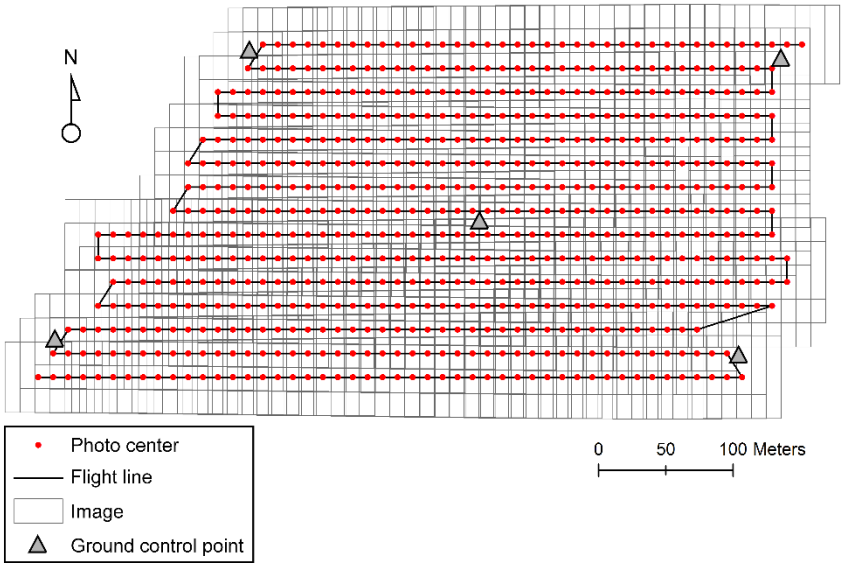

Figure 2. Flight planning and distribution of ground control points.

2.2. Thermal Image Processing

Thermal images were processed in three stages: thermal drift correction, geometric correction, and radiometric correction. Figure 3 describes the drift correction applied to the thermal images. As previously discussed, thermal drift is when the same location in the terrain presents different temperature values in different images. Thermal drift correction is based on points having a constant temperature during the UAV flight. In the first stage, a set of distinctive features are extracted from the UAV images using algorithms based on "structure from motion" (SfM) techniques described by Lowe [40]. SfM techniques extract individual features in each thermal image that are matched to their corresponding feature in the other images from the same UAV flight. As Figure 3 shows, a point appears in several images that belongs to different laps, each having a different temperature value due to drift effect. Every thermal image has a temporal reference, allowing the drift effect to be evaluated as it occurred in flight. In the proposed methodology, sensor drift is modeled as a function of time where each point of each image has a timestamp obtained by a GNSS sensor from the UAV autopilot. This methodology is applied to the set of characteristics extracted by the SfM algorithms. As a result, a mathematical model that describes thermal drift as it occurs for the duration of the UAV flight is achieved. Subsequently, this model is applied to all thermal images to obtain a new thermal image where temperature values are uniform on all corresponding points along the UAV flight. Six

different drift correction models (DCMs) were developed to describe thermal drift for the duration of the UAV flight: exponential, exponential, lineal and polynomial order two, three, and four. Each DCM was applied to the UAV thermal images to generate a new collection of images, which were orthorectified and then processed into thermal orthomosaics.

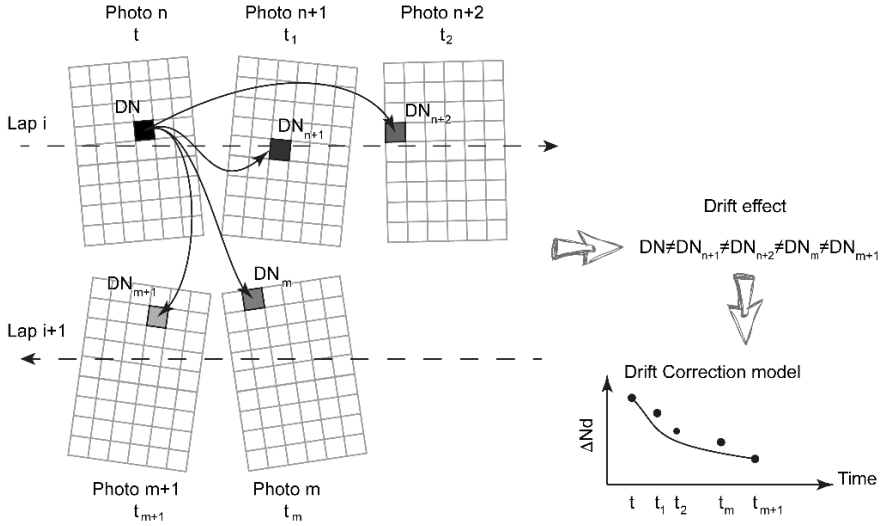

Figure 3. Graphical description of thermal drift correction model (DN: digital number, t: time).

To obtain a single thermal orthomosaic of the area of interest, images have to be aerotriangulated, rectified, and finally mosaicked. Based on previous research results, Pix4dmapper by Pix4D SA was selected (Lausanne, Switzerland) and described by Mesas-Carrascosa [15] to do this processing. Afterward, digital numbers (DNs) of the thermal orthomosaics were converted to temperature values using the information obtained by the radiometric calibration of the sensor provided by the manufacturer. Finally, remotely sensed temperatures are influenced by the environmental conditions present at the time of UAV flight. Atmospheric correction of surface temperature is essential to extract absolute temperature measurements from thermal images, requiring the application of a radiative transfer model [41], a vicarious calibration [42], or an empirical method [43]. In this research, using an empirical method, two extreme temperature panels of 0.5 × 0.5m were placed in the plot to record the hottest (black polymer panel) and the coldest (white polymer panel) temperatures on scene. Reference panels were close to five times larger than the GSD and, therefore, several homogeneous pixels appear in the thermal images. A temperature measurement of each reference panel was collected

for each UAV flight with a Flir E60 heat gun (Flir Systems, Oregon, USA). These measurements were later used to correct the atmospheric effect on the thermal mosaics, applying an empirical line method, which defines a linear relationship between absolute temperature and sensor temperature [44].

2.3. Validation

The analysis of the proposed methodology was applied to all UAV flights both with and without thermal drift correction. A total of 37 georeferenced checkpoints (CPs) were placed along a transect perpendicular to the laps and crossing the middle zone of the plot and were read for temperature using a Flir E60 heat gun. These values were compared to the extracted values from the thermal orthomosaics obtained from the flights. The mean error and root mean square error (RMSE) were calculated for each model and flight. Moreover, Akaike's information criterion (AIC) [45] was used to identify the relative importance among all possible sets of DCMs per UAV flight where the best performing in each flight was identified by the lowest AIC score.

In addition, the correlation between flight time and thermal drift was defined. To do this, the thermal images in which a CP appeared were analyzed. Of all the possible thermal images where a CP appeared, the images with the most centrally situated CP were used in the mosaic process to obtain a thermal orthomosaic, as this is the standard method. As each image has an associated timestamp, each CP was temporally registered as it appeared in flight, which was then evaluated for the influence of flight time on thermal drift for each thermal orthomosaic obtained by a DCM.

3. Results

Figure 4 shows the variation of digital number per second ($\Delta DN/t$) along the duration of the UAV flights on features extracted from images and the different DCMs per flight developed for the proposal methodology. Comparing the four UAV flights, digital number per second in raw images varied both in absolute and relative terms. Therefore, the thermal sensor did not show a defined pattern in registering temperatures. Each DCM calculated per flight and its correlation coefficient (R^2) are summarized in Table 2. At 8:30 a.m. (Figure 4a), $\Delta DN/t$ had no defined behavior, showing a disperse distribution. Regardless of the mathematical model used, the correlation coefficient showed a value between 0.370 with the linear model and 0.382 for the exponential model of order 2. Therefore, there were no clear differences a priori between DCMs applied to thermal orthomosaics.

At 12.30 p.m. (Figure 4b), $\Delta DN/t$ started to show a trend in its relation to flight duration as R^2 of some DCMs revealed. In this case, at the beginning of the UAV flight the $\Delta DN/t$ showed lower values over time (between 0 and 100 s) but then the variation increased, reaching the highest variation between 200 and 400 s. Thereafter, the variation decreased to values equal to the beginning of the UAV flight until 700 s where it again increased, although it did not reach the initial maximum values. In this flight, the bicubic model showed the highest R^2, equal to 0.482, while the exponential model had the lowest, 0.190. At 16.00 p.m. (Figure 4c), $\Delta DN/t$ showed a defined evolution as the UAV flight progressed, which was reflected in higher R^2 values for all the DCMs. In this mission, $\Delta DN/sec$ showed maximum values at the beginning of the UAV flight and then decreased over time. The exponential order 2 and lineal models had the lowest R^2 value (0.688) while the bicubic model had, again, the highest R^2 value (0.836). The other DCMs had an R^2 value higher than 0.7. Finally, the mission at 18:30 p.m. (Figure 4d) showed more oscillations during flight time; however, the range of $\Delta DN/sec$ values was narrow. With this mission, maximum variations occurred at the beginning of the UAV flight, decreasing as the flight progressed. R^2 values were between 0.67 and 0.69 with no clear differences between the DCMs. Therefore, in analyzing the behavior of $\Delta DN/t$ along the UAV flight duration for these missions, it is possible to assert that the thermal sensor was not stable and that its operation varied in each UAV flight.

Regarding R^2, the DCMs obtained from the UAV flights at 16:00 p.m. and 18:30 p.m. had higher values than those from 8:30 a.m. and 12:30 p.m. because $\Delta DN/sec$ showed a shorter range of values by time. This is due to the fact that $\Delta DN/t$ per second was different for each UAV flight, occurring with a lower frequency at later UAV flights.

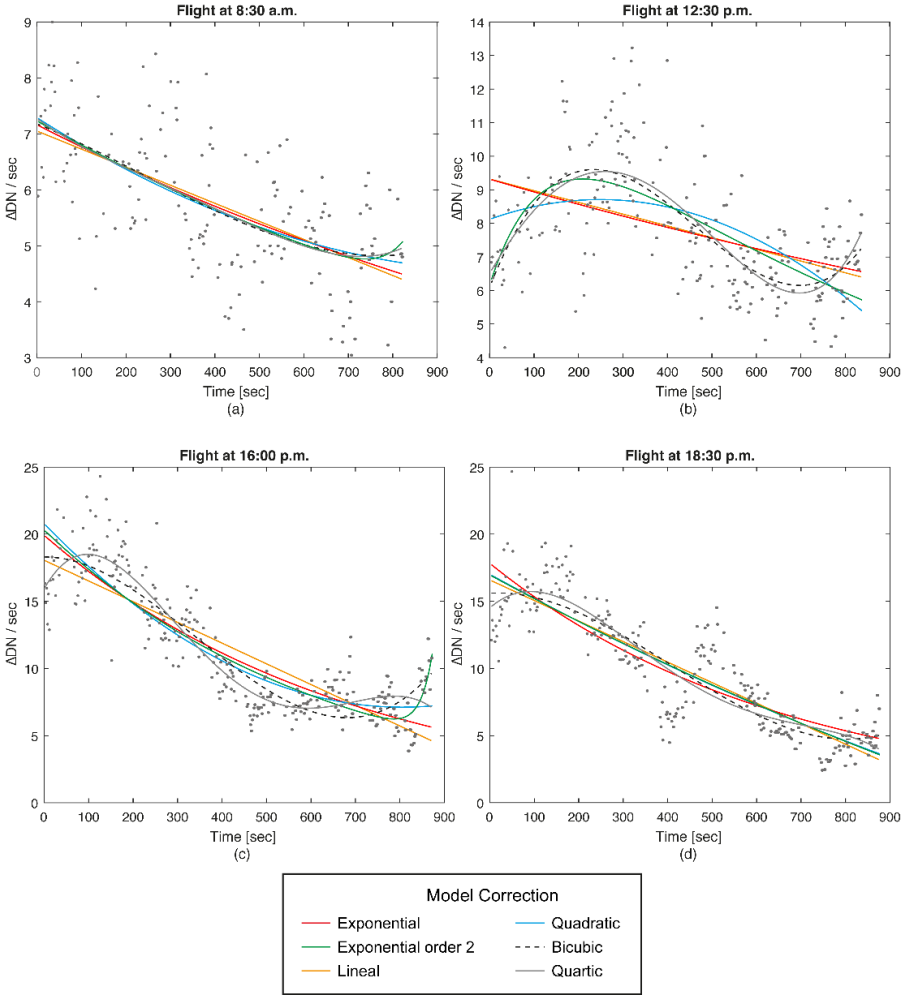

Figure 4. Relationship obtained between the variation of digital number per second (ΔDN/sec) and flight duration for exponential, exponential order 2, lineal, quadratic, bicubic, and quartic drift correction models at (**a**) 8:30 a.m., (**b**) 12:30 p.m., (**c**) 16:00 p.m., and (**d**) 18:00 p.m.

Table 2. Drift correction models for each mission and coefficient of correlation ($\mathbf{R^2}$).

DCM Type	Time of Flight	Equation	R^2
Exponential order 1	8:30	$c = 7.160 \cdot e^{-5.677 \cdot 10^{-4} \cdot t}$	0.375 *
	12:00	$c = 9.317 \cdot e^{-4.1911 \cdot 10^{-4} \cdot t}$	0.190 n.s.
	16:00	$c = 19.923 \cdot e^{-0.001 \cdot t}$	0.733 **
	18:30	$c = 18.368 \cdot e^{-0.001 \cdot t}$	0.688 **
Exponential order 2	8:30	$c = 3.833 \cdot 10^{-7} \cdot e^{0.017 \cdot t} + 7.227 \cdot e^{-6.131 \cdot 10^{-4} \cdot t}$	0.382 *
	12:00	$c = 13.121 \cdot e^{-9.923 * 10^{-4} \cdot t} - 6.958 \cdot e^{-0.007 \cdot t}$	0.398 *
	16:00	$c = 20.316 \cdot e^{-0.001 \cdot t} + 8.155 \cdot 10^{-14} \cdot e^{-0.36 \cdot t}$	0.688 **
	18:30	$c = 6.985 \cdot 10^{4} \cdot e^{-2.791 \cdot t} - 6.9833 \cdot 10^{-4} \cdot e^{-2.7889 \cdot 10^{-4} \cdot t}$	0.675 **
Lineal	8:30	$c = -0.003 \cdot t + 7.048$	0.370 *
	12:00	$c = -0.003 \cdot t + 9.321$	0.210 n.s.
	16:00	$c = -0.015 \cdot t + 18.062$	0.688 **
	18:30	$c = -0.015 \cdot t + 16.991$	0.673 **
Quadratic	8:30	$c = 2.339 \cdot 10^{-6} \cdot t^2 - 0.005 \cdot t + 7.28$	0.379 *
	12:00	$c = -9.601 \cdot 10^{-6} \cdot t^2 + 0.004 \cdot t + 8.120$	0.286 n.s.
	16:00	$c = -2.117 \cdot 10^{-5} \cdot t^2 + 0.034 \cdot t + 20.780$	0.755 **
	18:30	$c = -4.587 \cdot 10^{-6} \cdot t^2 + 0.019 \cdot t + 17.576$	0.676 **
Bicubic	8:30	$c = 4.786 \cdot 10^{-9} \cdot t^3 - 3.401 \cdot t^2 - 0.003 \cdot t + 7.117$	0.380 *
	12:00	$c = 6.913 \cdot 10^{-8} \cdot t^3 - 9.654 \cdot 10^{-5} \cdot t^2 + 0.033 \cdot t + 6.098$	0.482 *
	16:00	$c = 7.632 \cdot 10^{-8} \cdot t^3 - 7.838 \cdot 10^{-5} \cdot t^2 + 4.128 \cdot 10^{-4} \cdot t + 18.299$	0.836 **
	18:30	$c = 4.006 \cdot 10^{-8} \cdot t^3 - 4.858 \cdot 10^{-5} \cdot t^2 - 0.001 \cdot t + 16.233$	0.694 **
Quartic	8:30	$c = 1.630 \cdot 10^{-11} \cdot t^4 - 2.185 \cdot t^3 + 1.056 \cdot 10^{-6} \cdot t^2 - 0.005 \cdot t + 7.270$	0.381 *
	12:00	$c = 7.068 \cdot 10^{-11} \cdot t^4 - 4.838 \cdot 10^{-8} \cdot t^3 - 3.426 \cdot 10^{-5} \cdot t^2 + 0.002 \cdot t + 6.51$	0.474 *
	16:00	$c = -3.173 \cdot 10^{-6} \cdot t^4 + 6.261 \cdot 10^{-7} \cdot t^3 - 3.828 \cdot 10^{-4} \cdot t^2 + 0.058 \cdot t + 15.927$	0.799 **
	18:30	$c = -1.351 \cdot 10^{-10} \cdot t^4 + 2.791 \cdot 10^{-7} \cdot t^3 - 1.837 \cdot 10^{-4} \cdot t^2 + 0.025 \cdot t + 15.138$	0.688 **

The asterisks indicate the level of significance (* $p < 0.05$, ** $p < 0.001$, n.s. not significant).

Figure 5 shows the thermal orthomosaic histograms for each flight mission with the applied DCMs, as well as without a DCM; Table 3 summarizes the statistics for each. First, the histograms manifest a clear difference between the thermal orthomosaics where a DCM was applied compared to those where no DCM was applied. Moreover, the temperature distribution was quite similar in all the thermal orthomosaics where a DCM was applied. Because the study area had two differentiated classes, vegetation and bare soil, a bimodal distribution was expected to describe temperature distribution of the scene. However, at the 8:30 a.m. UAV mission (Figure 5a), all thermal orthomosaics had a normal distribution as Sarle's bimodality coefficient (SBC) showed. The temperature range on those thermal orthomosaics where a DCM was applied ranged from 15 to 35 °C, 20 °C occurring with the most frequency. Conversely, the thermal orthomosaic without any drift correction showed a broader temperature range from 15 to 43 °C and a right-skewed distribution. Instead of a bimodal distribution, a normal distribution of temperatures occurred in the early morning on the thermal orthomosaics with drift correction because the bare soil and vegetation had not yet absorbed heat from the sunlight and consequently the temperatures of both were similar. Therefore, at this hour, both classes showed no clear difference in thermal behavior. Conversely, at 12:30 p.m. (Figure 5b), the UAV flight histograms showed two different shapes irrespective of whether a DCM was applied or not. However, when no drift correction was applied, the temperature distribution was, again, similar to a normal distribution with SBC being less than 5/9. As a result, the non-corrected histogram did not properly mark bare soil and vegetation with different temperatures. On the other hand, all drift-corrected thermal orthomosaics showed an SBC higher than 5/9, having a bimodal distribution with two differentiated peaks. In this mission, bare soil and vegetation had different behaviors as they correlated to sunlight. Although both classes increased their temperature, vegetation (left peak) showed a mean temperature equal to 30 °C, which was lower than bare soil (right peak), which reached a mean value equal to 50 °C. At 16:30 p.m. (Figure 5c), both vegetation and bare soil increased in temperature, which was properly shown when a DCM was applied. If corrections were not applied, the temperatures were also higher but the classes were not accurately represented in the histogram. A comparison of the histograms shows that vegetation temperature increased as the day progressed, reaching the highest temperature at 18:30 p.m. while soil temperature increased until 16:30 p.m. and then began to decrease. At 18:30

p.m. (Figure 5d), the left peak of the histogram has a higher frequency than the right peak as the vegetation maintained a stable temperature while the bare soil temperature decreased, which also caused the distance between the peaks to be reduced. These results are because the soil was cooling due to the declining sun and greater shadow cover.

All of the DCMs used successfully described this occurrence from 12:30 p.m. to 18:30 p.m. Moreover, the histograms of each DCM for every flight had a similar distribution with the quartic model presenting the greatest differences in portions of the flights. The histograms show that from 12:30 p.m., the temperature difference between the vegetation and bare soil was quite distinctive and remained so until 16:30 p.m. when the difference began to decrease. Therefore, as in Bellvert et al. (2014) [43], it is recommended that thermal UAV flights with agronomic objectives are performed between 12:00 and 16:30 p.m. However, without the method proposed in this paper, non-corrected thermal orthomosaics will not sufficiently differentiate soil and vegetation.

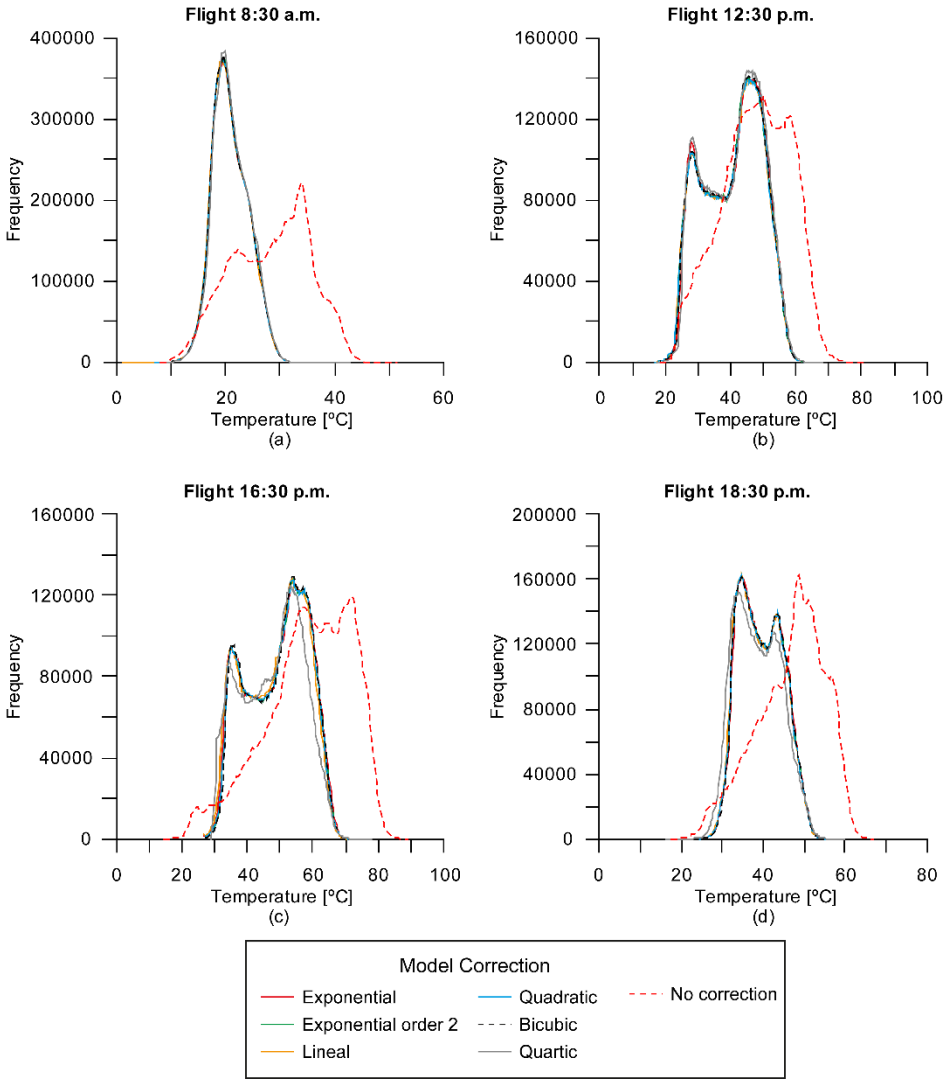

Figure 5. Thermal orthomosaic histograms at (**a**) 8:30 a.m., (**b**) 12:30 p.m., (**c**) 16:30 p.m., and (**d**) 18:30 p.m. for each drift correction model and without correction.

Table 3. Statistics of thermal orthomosaics.

Time of Flight		Exponential	Exponential Order 2	Lineal	Quadratic	Cubic	Quartic	No DCM
8:30 a.m.	Range	35.33	35.66	35.66	35.68	34.64	34.33	43.16
	Mean	20.92	20.96	20.88	20.95	20.96	21.10	28.35
	SD	3.29	3.28	3.30	3.29	3.28	3.26	7.14
	SBC	0.38	0.38	0.38	0.38	0.38	0.38	0.47
12:30 p.m.	Range	50.08	50.03	50.15	50.31	49.80	50.72	62.38
	Mean	40.74	40.50	40.53	40.48	40.61	40.98	47.68
	SD	8.87	8.89	8.92	8.91	8.87	8.80	10.43
	SBC	0.66	0.66	0.66	0.66	0.66	0.67	0.45
16:00 p.m.	Range	50.89	49.82	50.52	50.08	50.18	48.71	74.52
	Mean	49.19	49.20	48.66	49.22	49.37	47.84	58.66
	SD	9.41	9.24	9.35	9.25	9.19	9.73	13.06
	SBC	0.68	0.68	0.68	0.68	0.68	0.65	0.48
18:30 p.m.	Range	43.78	39.65	42.83	41.17	42.46	43.74	49.57
	Mean	39.57	39.47	39.37	39.46	39.55	38.61	46.69
	SD	5.24	5.26	5.28	5.24	5.23	5.55	8.32
	SBC	0.67	0.67	0.66	0.67	0.67	0.66	0.48

SBC: Sarle's bimodality coefficient. SD: standard deviation.

Validation

Once the histograms of the drift corrected thermal orthomosaics accurately described the presence of vegetation and bare soil in the study

area, the next step was to analyze which DCM had the greatest thermal accuracy. Figure 6 illustrates the 16:30 p.m. thermal orthomosaics with the applied DCMs, which are detailed in Table 2, as well as without drift correction. When drift correction was not applied (Figure 6g), the resulting thermal orthomosaics ordered the temperature values. From a visual analysis, neither bare soil nor vegetation showed stable temperature. Moreover, temperature changed along the north and south laps, registering higher temperature values as the UAV flight progressed. This effect is pronounced in this paper because NUC was switched off to obtain an extreme example; in other cases, the drift effect would be less pronounced. This also explains the pronounced skewness in the non-corrected histograms presented in Figure 5. Based on the authors' results, the temperature variation for this sensor under normal conditions was less than 0.5 °C per minute, similar to the variations reported by Olbrycht and Więcek (2015) [29].

Regarding the thermal orthomosaics where a DCM was applied (Figure 6a–f), no visual temperature differences from north to south were detected. Instead, the temperature variations were linked to the state of vegetation and bare soil as explained by the histogram analysis above. In addition, comparing all of the thermal orthomosaics generated with a DCM resulted in similar orthomosaics with the exception of the quartic model (Figure 6f). This model generated colder temperatures in the south of the plot compared to the north of the plot, which was not present in the other DCMs. These differences were not detected in the field campaign, suggesting that the quartic model did not adequately describe thermal drift in the UAV flights. This result occurred for all of the UAV flights assessed.

Table 4 summarizes the results of thermal quality control on the thermal orthomosaics from each UAV flight with and without the applied DCMs by mean error and standard deviation (SD) and Akaike's information criterion (AIC). In addition, a correlation coefficient (r^2) between error and flight progress was calculated. In all the orthomosaics, as expected, where a DCM was not applied, the temperature errors were higher than where a DCM was applied. Therefore, it is necessary to pre-process thermal images taking into account the behavior of the microbolometer registering temperature values. The 8:30 a.m. mission showed a higher rate of error than the other UAV missions independent of which DCM was applied. At this time, the error ranged from 0.88 ± 0.8 °C using the bicubic model correction to 1.01 ± 0.81 °C using the exponential correction model. These higher errors are explained by the different environmental conditions while performing the UAV flight and measuring ground truth. In the early morning, the sun is ascending and an object's or

coverage's superficial temperature changes in a short time interval. Although ground truth measurements were performed immediately after the UAV flight finished (twenty minutes), the duration of the UAV flight was long enough for temperature values of the olive trees and bare soil to change both for images and for on-ground measurements, influencing this mission's results. At 12:30 p.m., the mean error decreased to values around 0.2 °C ± 0.5 °C for all DCMs applied with the cubic model generating the smallest error (0.10 °C ± 0.45 °C) while the exponential model order 2 had the highest error (0.29 °C ± 0.56 °C). Conversely, at 16:30 p.m., the errors differed depending on the DCM used. For this mission, the quartic model showed the highest error (1.57° ± 1.22 °C) while the cubic model had the lowest (0.06 ± 0.45 °C). Finally, at 18:30 p.m., the cubic model again showed the greatest accuracy with an error equal to 0.26 ± 0.58 °C and the quartic model being the worst with an error equal to 1.55 ± 0.85 °C. Even so, the highest mean error and SD were found in those thermal orthomosaics where no DCM was applied, independent of the mission. Moreover, the calculated AIC scores identified the cubic model as the most consistent DCM, showing the minimum score in each UAV flight.

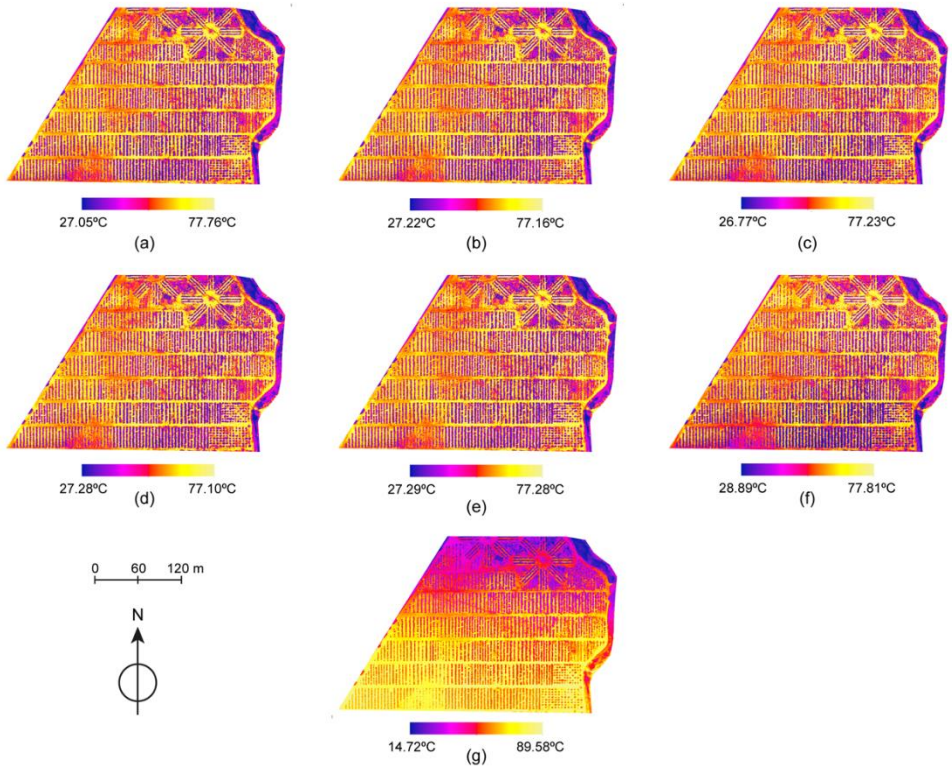

Figure 6. Comparison of thermal orthomosaics at 16:30 p.m. with drift model corrections: (**a**) exponential, (**b**) exponential order 2, (**c**) lineal, (**d**) quadratic, (**e**) bicubic, (**f**) quartic, and (**g**) no correction.

Table 4. Mean error, standard deviation (SD), Akaike's information criterion (AIC), and coefficients of correlation (r^2) for each model correction and mission.

		Exponential	Exponential 2	Lineal	Quadratic	Cubic	Quartic	No DCM
8:30	Mean	1.013	0.898	0.913	0.901	0.88	0.895	−2.929
	SD	0.818	0.804	0.815	0.800	0.80	0.758	2.792
	AIC	3.777	0.832	3.593	2.574	0.77	18.472	--
	r^2	0.027	0.004	0.001	0.005	0.04	0.645 **	0.918 **
12:30	Mean	0.288	0.291	0.225	0.222	0.10	0.212	−3.555
	SD	0.590	0.560	0.556	0.569	0.45	0.584	3.012
	AIC	39.833	27.437	36.364	31.673	26.6	56.955	--
	r^2	0.007	0.025	0.052	0.08	0.06	0.322 **	0.959 **
16:30	Mean	0.112	-0.152	0.518	−0.123	−0.06	1.573	−12.158
	SD	0.588	0.493	0.795	0.508	0.45	1.224	7.363
	AIC	18.219	7.452	11.329	7.765	2.31	31.893	--
	r^2	0.391 **	0.156 *	0.667 **	0.168 *	0.00	0.359 **	0.915 **
18:30	Mean	0.379	0.409	0.524	0.404	0.26	1.557	−9.544
	SD	0.648	0.622	0.627	0.626	0.58	0.857	5.433
	AIC	12.992	6.888	13.871	9.006	2.56	29.432	--
	r^2	0.001	0.009	0.032	0.005	0.02	0.568 **	0.880 **

Pearson's analysis. ** Correlation is significant at the 0.01 level (2-tailed);
* Correlation is significant at the 0.05 level (2-tailed).

To demonstrate, Figure 7 shows the relationship between temperature obtained from the UAV flight and the on-ground measurements at 16:30 p.m. The continuous line represents a perfect correlation of temperatures between both sets of temperatures and a discontinuous line represents the adjusted lineal model from both sets. When no DCM was applied (Figure 7g), the temperature values in the thermal orthomosaic did not show any relationship with those on the ground having a broad range of variation. On the other hand, in general, when a DCM was applied, temperature values on the thermal orthomosaics and their corresponding on-ground measurement were similar. However, there were differences between the DCMs. The quartic model (Figure 7f) yielded the highest deviation from a perfect correlation although not as broad as in the case of not using a DCM. The same occurred when the exponential model (Figure 7a) or lineal model (Figure 7c) was applied, although not as evident as in the previous case. The remaining DCMs considered did not show significant differences in their temperature values.

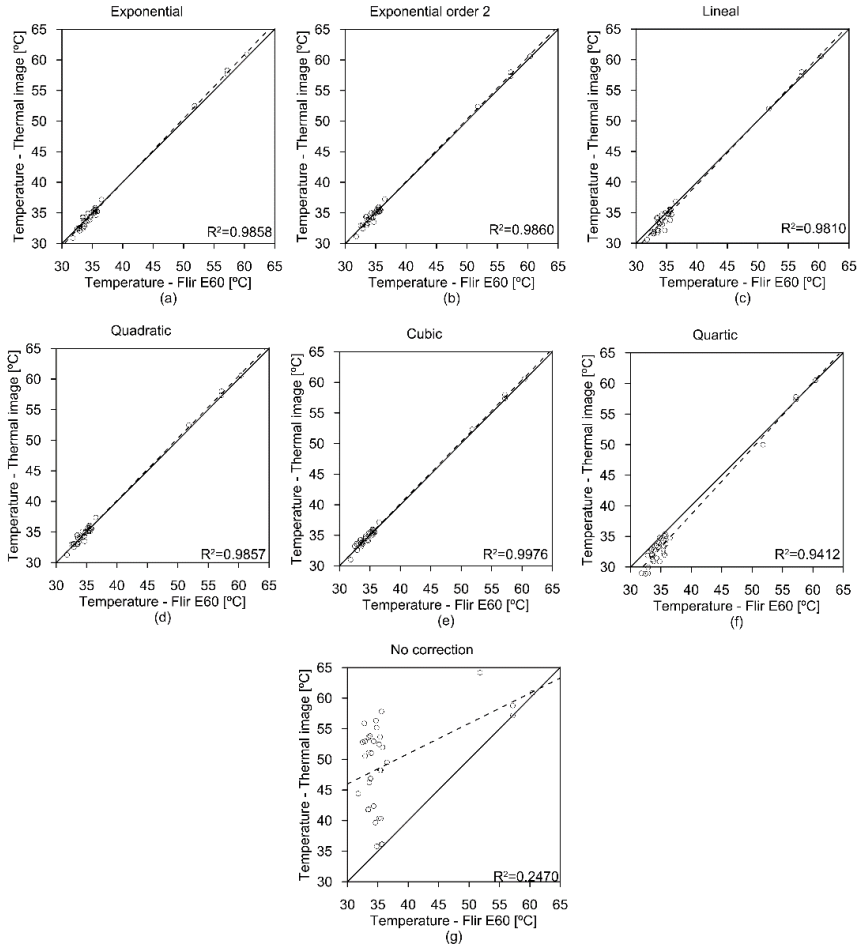

Figure 7. Correlation for each drift correction model (DCM) between temperature values from the thermal orthomosaic and on-ground measurement at 16:30 p.m. unmanned aerial vehicle (UAV) flight. DCM: (a) exponential, (b) exponential order 2, (c) lineal, (d) quadratic, (e) cubic, (f) quartic and (g) no correction.

Moreover, to have an acceptable range of temperature error, it is necessary that this error occurs independently of the flight duration, meaning that the drift effect of the microbolometer has been adjusted accordingly. Table 4 shows this relationship through a correlation coefficient and its Pearson analysis and Figure 8 shows the relation between error and flight duration for each thermal orthomosaic obtained from the 16:30 p.m. mission where a DCM was applied. As expected, the thermal orthomosaics where a DCM was not applied showed high R^2 between error and flight duration in all UAV flights, meaning that the error is dependent

on flight duration. As to the thermal orthomosaics where a DCM was applied, the quartic model was the one whose errors showed a significant correlation with flight duration in all UAV flights. The other DCMs had no significant correlation at 8:30 a.m., 12:30 p.m., and 18:30 p.m. At 16:30 p.m., the cubic model was the only DCM whose results were independent of flight duration. Therefore, when considering the relationship between temperature error and flight duration, the cubic model adequately described drift effect on temperature measurements on all performed UAV flights. In this study and our experience, using the Gobi 640 thermal sensor on subsequent UAV flights has shown that the cubic drift model is the most adequate. However, for other thermal sensors, it is recommendable to analyze which model would better describe drift effect using the proposed methodology.

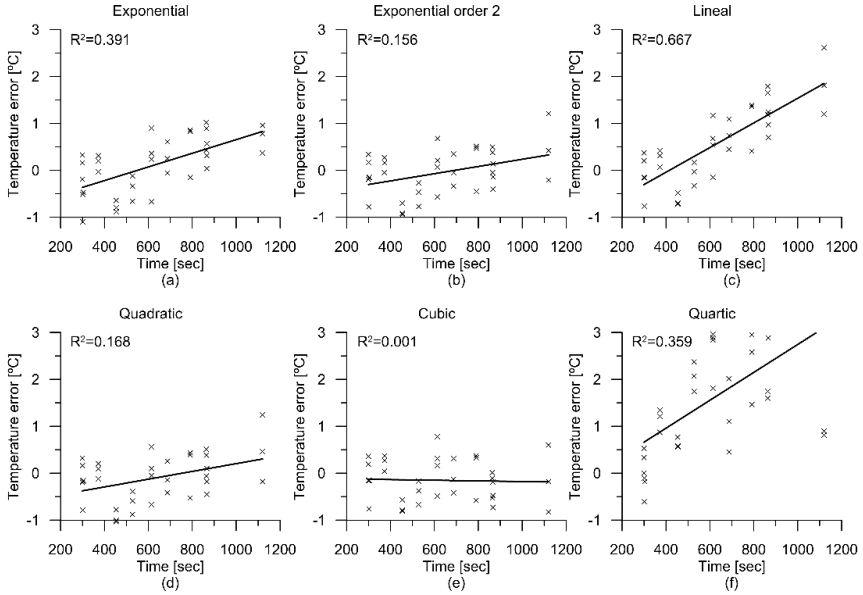

Figure 8. Relationship for each DCM between temperature error and flight duration for the 16:30 p.m. mission. DCM: (a) exponential, (b) exponential order 2, (c) lineal, (d) quadratic, (e) cubic, (f) quartic.

The temperature error obtained in this research when a DCM was applied is equal to those described in the literature [8,38] and therefore presents itself as another option for agronomical projects. Moreover, the proposed methodology presents an advantage as it optimizes flight time. In other studies, it is necessary to stabilize the sensor in flight [36] or it is necessary to recurrently fly over temperature targets for reference to calibrate thermal images [38]. These two strategies spend the limited

battery charge and, therefore, reduce the area covered by the UAV flight due to the decrease in useful flight time. With the proposed methodology, flight time is maximized without loss of accuracy in temperature values. Moreover, it allows the use of a thermal sensor on board the UAV regardless of the drift effect.

The UAV flights were performed under stable weather conditions and were of short duration (20 min) and as such, there were no changes in the surface temperature. However, UAV flights with longer duration (longer than 30 min) and/or under unstable weather conditions must be evaluated in future work due to changes in atmospheric or sunlight conditions. In these cases, in addition to the drift correction, it would be necessary to have an instantaneous atmospheric correction adapted to the UAV flight conditions. One possible methodology is to equip the UAV platform with additional sensors that record values of temperature, relative humidity, atmospheric pressure, incident radiation, and wind speed. These parameters would allow the possibility of determining the atmospheric conditions linked to each individual thermal image and, therefore, at each moment of flight time. These parameters along with the drift effect model would allow more precise and accurate temperature values.

4. Conclusions

Remote sensing using lightweight uncooled thermal sensors on board UAVs is a useful tool for measuring crop temperatures. However, drift effect on registered temperatures can invalidate its agronomical applications where an accuracy greater than 1 °C is necessary. The present research has developed methodology to remove drift effect on temperature using a lightweight microbolometer thermal sensor on board a UAV. In this study, removing drift effect on thermal images is based on redundant information around objects that appear in different overlapping images from a UAV flight that covers the area of interest. Different mathematical models were explored to describe drift effect with the cubic drift model yielding the best results on separate missions performed for this research.

These models were tested in four UAV missions at different hours at the same location. If no drift correction was applied, the thermal orthomosaics did not adequately describe crop temperatures, invalidating their use within an agronomical context. Contrarily, if a drift correction model was applied using the proposed methodology, the results improved with a range of error that would be adequate for agronomical projects. Moreover, the accuracy is in the same range as other authors' results but with the added benefit of not requiring any special in air UAV flight

operation and thusly increasing useful flight time. This is an important point to those UASs with short flight durations due to limited battery power. In addition, this methodology was applied to a single UAV flight and, therefore, the proposed drift correction model is adaptable to specific flight conditions.

In this study, the cubic drift model offered the best results. However, the authors recommend exploring the behavior of a particular uncooled thermal sensor to determine which model would best describe the drift effect using the proposed methodology.

Acknowledgments: This research was funded by Khepri project supported by CDTI: Centro para el Desarrollo Tecnológico Industrial, FEDER Funds: Fondo Europeo de Desarrollo Regional and CTA: Corporación Tecnológica de Andalucía.

Author Contributions: Francisco Javier Mesas-Carrascosa and Fernando Pérez Porras. conceived and designed the experiments; Francisco Javier Mesas-Carrascosa, Fernando Pérez Porras, Jose Emilio Meroño de Larriva. and Alfonso García-Ferrer performed the experiments; Francisco Javier Mesas-Carrascosa, Fernando Pérez Porras, Carlos Mena Frau, Francisco Agüera-Vega, Fernando Carvajal-Ramírez. and Patricio Martinez-Carricondo analyzed the data; Francisco Javier Mesas-Carrascosa wrote the paper.

Conflicts of Interest: The authors declare no conflict interest.

References

1. Alexandratos, N.; Bruinsma, J. World Agriculture Towards 2030/2050: The 2012 Revision; Agriculture Development Economics Division Food and Agriculture Organization of the United Nations: 2012. Publisher: Publication (Rome, Italy). Avaliable online: http://www.fao.org/docrep/016/ap106e/ap106e.pdf (accessed on 16th April 2018.)
2. McCalla, A.F. Challenges to world agriculture in the 21st century. UPDATE Agric. Resour. Econ. 2001, 4. Available online: https://giannini.ucop.edu/publications/are-update/issues/2001/4/3/challenges-to-world-agric/ (accessed on 16th April 2018)
3. Stafford, J.V. Implementing precision agriculture in the 21st century. J. Agric. Eng. Res. 2000, 76, 267–275.
4. Miao, Y.; Mulla, D.J.; Randall, G.W.; Vetsch, J.A.; Vintila, R. Combining chlorophyll meter readings and high spatial resolution remote sensing images for in-season site-specific nitrogen management of corn. Precis. Agric. 2009, 10, 45–62.
5. Mulla, D.J. Twenty five years of remote sensing in precision agriculture: Key advances and remaining knowledge gaps. Biosyst. Eng. 2013, 114, 358–371.

6. Goetz, A.F.H. Three decades of hyperspectral remote sensing of the earth: A personal view. Remote Sens. Environ. 2009, 113, S5–S16.
7. Anderson, K.; Gaston, K.J. Lightweight unmanned aerial vehicles will revolutionize spatial ecology. Front. Ecol. Environ. 2013, 11, 138–146.
8. Berni, J.A.J.; Zarco-Tejada, P.J.; Sepulcre-Cantó, G.; Fereres, E.; Villalobos, F. Mapping canopy conductance and cwsi in olive orchards using high resolution thermal remote sensing imagery. Remote Sens. Environ. 2009, 113, 2380–2388.
9. Colomina, I.; Molina, P. Unmanned aerial systems for photogrammetry and remote sensing: A review. ISPRS J. Photogramm. Remote Sens. 2014, 92, 79–97.
10. McBratney, A.; Whelan, B.; Ancev, T.; Bouma, J. Future directions of precision agriculture. Precis. Agric. 2005, 6, 7–23.
11. Lin, Y.; Hyyppa, J.; Jaakkola, A. Mini-uav-borne lidar for fine-scale mapping. IEEE Geosci. Remote Sens. Lett. 2011, 8, 426–430.
12. Wallace, L.; Lucieer, A.; Watson, C.; Turner, D. Development of a uav-lidar system with application to forest inventory. Remote Sens. 2012, 4, 1519–1543.
13. Torres-Sánchez, J.; Peña, J.M.; de Castro, A.I.; López-Granados, F. Multi-temporal mapping of the vegetation fraction in early-season wheat fields using images from uav. Comput. Electron. Agric. 2014, 103, 104–113.
14. López-Granados, F.; Torres-Sánchez, J.; Serrano-Pérez, A.; de Castro, A.I.; Mesas-Carrascosa, F.-J.; Peña, J.-M. Early season weed mapping in sunflower using uav technology: Variability of herbicide treatment maps against weed thresholds. Precis. Agric. 2016, 17, 183–199.
15. Mesas-Carrascosa, F.-J.; Torres-Sánchez, J.; Clavero-Rumbao, I.; García-Ferrer, A.; Peña, J.-M.; Borra-Serrano, I.; López-Granados, F. Assessing optimal flight parameters for generating accurate multispectral orthomosaicks by uav to support site-specific crop management. Remote Sens. 2015, 7, 12793–12814.
16. Candiago, S.; Remondino, F.; De Giglio, M.; Dubbini, M.; Gattelli, M. Evaluating multispectral images and vegetation indices for precision farming applications from uav images. Remote Sens. 2015, 7, 4026–4047.
17. Zarco-Tejada, P.J.; Guillén-Climent, M.L.; Hernández-Clemente, R.; Catalina, A.; González, M.R.; Martín, P. Estimating leaf carotenoid content in vineyards using high resolution hyperspectral imagery acquired from an unmanned aerial vehicle (uav). Agric. Forest Meteorol. 2013, 171–172, 281–294.
18. Hruska, R.; Mitchell, J.; Anderson, M.; Glenn, N.F. Radiometric and geometric analysis of hyperspectral imagery acquired from an unmanned aerial vehicle. Remote Sens. 2012, 4, 2736–2752.
19. Baluja, J.; Diago, M.P.; Balda, P.; Zorer, R.; Meggio, F.; Morales, F.; Tardaguila, J. Assessment of vineyard water status variability by thermal and multispectral imagery using an unmanned aerial vehicle (uav). Irrig. Sci. 2012, 30, 511–522.

20. Gonzalez-Dugo, V.; Zarco-Tejada, P.; Nicolás, E.; Nortes, P.A.; Alarcón, J.J.; Intrigliolo, D.S.; Fereres, E. Using high resolution uav thermal imagery to assess the variability in the water status of five fruit tree species within a commercial orchard. Precis. Agric. 2013, 14, 660–678.
21. Fereres, E.; Soriano, M.A. Deficit irrigation for reducing agricultural water use. J. Exp. Bot. 2007, 58, 147–159.
22. Calderón, R.; Navas-Cortés, J.A.; Lucena, C.; Zarco-Tejada, P.J. High-resolution airborne hyperspectral and thermal imagery for early detection of verticillium wilt of olive using fluorescence, temperature and narrow-band spectral indices. Remote Sens. Environ. 2013, 139, 231–245.
23. Zarco-Tejada, P.J.; González-Dugo, V.; Berni, J.A.J. Fluorescence, temperature and narrow-band indices acquired from a uav platform for water stress detection using a micro-hyperspectral imager and a thermal camera. Remote Sens. Environ. 2012, 117, 322–337.
24. Gonzalez-Dugo, V.; Hernandez, P.; Solis, I.; Zarco-Tejada, P.J. Using high-resolution hyperspectral and thermal airborne imagery to assess physiological condition in the context of wheat phenotyping. Remote Sens. 2015, 7, 13586–13605.
25. Chapman, S.C.; Merz, T.; Chan, A.; Jackway, P.; Hrabar, S.; Dreccer, M.F.; Holland, E.; Zheng, B.; Ling, T.J.; Jimenez-Berni, J. Pheno-copter: A low-altitude, autonomous remote-sensing robotic helicopter for high-throughput field-based phenotyping. Agronomy 2014, 4, 279–301.
26. Gallo, M.A.; Willits, D.S.; Lubke, R.A.; Thiede, E.C. Low-cost uncooled ir sensor for battlefield surveillance. Proceed. SPIE 1993, 2020, pp 351–362.
27. Krupiński, M.; Bareła, J.; Firmanty, K.; Kastek, M. Test stand for non-uniformity correction of microbolometer focal plane arrays used in thermal cameras. Proceed. SPIE Int. Soc. Opt. Eng. 2013, 8896, doi:10.1117/12.2028633.
28. Huawei, W.; Caiwen, M.; Jianzhong, C.; Haifeng, Z. An adaptive two-point non-uniformity correction algorithm based on shutter and its implementation. In Proceedings of the 2013 Fifth International Conference on Measuring Technology and Mechatronics Automation, Hong Kong, China, 16–17 January 2013; pp 174–177.
29. Olbrycht, R.; Więcek, B. New approach to thermal drift correction in microbolometer thermal cameras. Quant. InfraRed Thermogr. J. 2015, 12, 184–195.
30. Mudau, A.E.; Willers, C.J.; Griffith, D.; Roux, F.P.J.L. Non-uniformity correction and bad pixel replacement on lwir and mwir images. In Proceedings of the 2011 Saudi International Electronics, Communications and Photonics Conference (SIECPC), Riyadh, Saudi Arabia, 24–26 April 2011; pp 1–5.
31. King, S.R.; Rekow, M.N.; Carlson, P.S.; Heinke, T.; Warnke, S.H.; Brest, B. Shutterless Infrared Imager Algorithm with Drift Correction. Google Patents US8067735B2, 2011.

32. Tempelhahn, A.; Budzier, H.; Krause, V.; Gerlach, G. Shutter-less calibration of uncooled infrared cameras. J. Sens. Sensor Syst. 2016, 5, doi:10.5194/jsss-5-9-2016.
33. Mizrahi, U.; Fraenkel, A.; Kopolovich, Z.; Adin, A.; Bikov, L. Method and System for Measuring and Compensating for the Case Temperature Variations in a Bolometer Based System. US Patent No. US 7807968 B2, 2010.
34. Harris, J.G.; Yu-Ming, C. Nonuniformity correction of infrared image sequences using the constant-statistics constraint. IEEE Trans. Image Process. 1999, 8, 1148–1151.
35. Zuo, C.; Chen, Q.; Gu, G.; Sui, X.; Ren, J. Improved interframe registration based nonuniformity correction for focal plane arrays. Infrared Phys. Technol. 2012, 55, 263–269.
36. Berni, J.A.J.; Zarco-Tejada, P.J.; Suarez, L.; Fereres, E. Thermal and narrowband multispectral remote sensing for vegetation monitoring from an unmanned aerial vehicle. IEEE Trans. Geosci. Remote Sens. 2009, 47, 722–738.
37. Zalameda, J.N.; Winfree, W.P. Investigation of uncooled microbolometer focal plane array infrared camera for quantitative thermography. J. Nondestruct. Eval. 2005, 24, 1–9.
38. Gómez-Candón, D.; Virlet, N.; Labbé, S.; Jolivot, A.; Regnard, J.-L. Field phenotyping of water stress at tree scale by uav-sensed imagery: New insights for thermal acquisition and calibration. Precis. Agric. 2016, 17, 786–800.
39. Jensen, A.M.; McKee, M.; Chen, Y. Procedures for processing thermal images using low-cost microbolometer cameras for small unmanned aerial systems. In Proceedings of the 2014 IEEE Geoscience and Remote Sensing Symposium, Quebec City, QC, Canada, 13–18 July 2014; pp 2629–2632.
40. Lowe, D.G. Distinctive image features from scale-invariant keypoints. Int. J. Comput. Vis. 2004, 60, 91–110.
41. Zarco-Tejada, P.J.; Berni, J.A.J.; Suárez, L.; Sepulcre-Cantó, G.; Morales, F.; Miller, J.R. Imaging chlorophyll fluorescence with an airborne narrow-band multispectral camera for vegetation stress detection. Remote Sens. Environ. 2009, 113, 1262–1275.
42. Torres-Rua, A. Vicarious calibration of suas microbolometer temperature imagery for estimation of radiometric land surface temperature. Sensors 2017, 17, 1499.
43. Honkavaara, E.; Saari, H.; Kaivosoja, J.; Pölönen, I.; Hakala, T.; Litkey, P.; Mäkynen, J.; Pesonen, L. Processing and assessment of spectrometric, stereoscopic imagery collected using a lightweight uav spectral camera for precision agriculture. Remote Sens. 2013, 5, 5006–5039.
44. Bellvert, J.; Zarco-Tejada, P.J.; Girona, J.; Fereres, E. Mapping crop water stress index in a 'pinot-noir' vineyard: Comparing ground measurements with thermal remote sensing imagery from an unmanned aerial vehicle. Precis. Agric. 2014, 15, 361–376.

45. Akaike, H. A new look at the statistical model identification. IEEE Trans. Autom. Control 1974, 19, 716–723.

5 CAPÍTULO 2

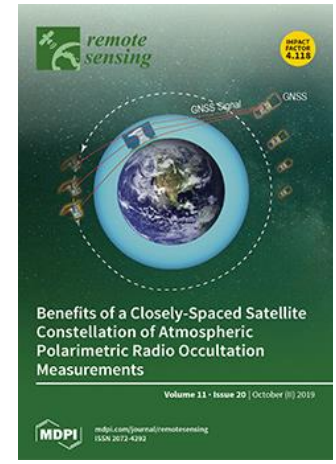

Open Access Article

Project-Based Learning Applied to Unmanned Aerial Systems and Remote Sensing

by Francisco Javier Mesas-Carrascosa *, Fernando Pérez Porras, Paula Triviño-Tarradas, Jose Emilio Meroño de Larriva and Alfonso García-Ferrer

Department of Graphic Engineering and Geomatics, University of Cordoba, Campus de Rabanales, 14071 Córdoba, Spain
* Author to whom correspondence should be addressed.

Remote Sens. **2019**, *11*(20), 2413; https://doi.org/10.3390/rs11202413

Received: 19 September 2019 / Revised: 5 October 2019 / Accepted: 16 October 2019 / Published: 17 October 2019

(This article belongs to the Special Issue Teaching and Learning in Remote Sensing)

Publicado en: **Remote Sensing, 2019, 11(20), 2413**

https://doi.org/10.3390/rs11202413

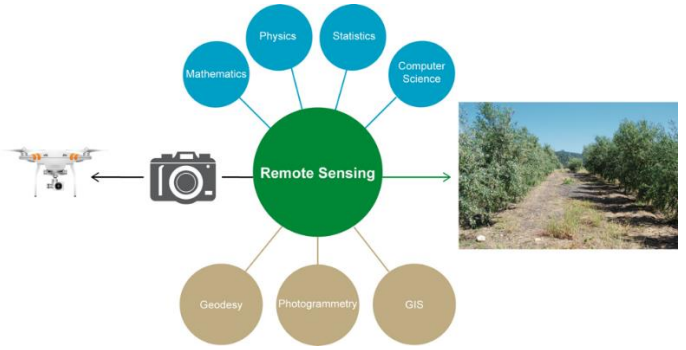

Project-Based Learning Applied to Unmanned Aerial Systems and Remote Sensing

Francisco-Javier Mesas-Carrascosa [1,*], Fernando Pérez Porras [1], Paula Triviño-Tarradas[1], Jose Emilio Meroño de Larriva [1] and Alfonso García-Ferrer [1]

[1] Department of Graphic Engineering and Geomatics, University of Cordoba, Campus de Rabanales, 14071 Córdoba, Spain; *o12pepof@uco.es(F.P.P.)*; *ig2trtap@uco.es(P.T-T.)*; *ir1melaj@uco.es(J.E.M.)*; *agferrer@uco.es(A.G-F.)*

***** Correspondence: *fjmesas@uco.es*

Received: 19 September 2019; Accepted: 16 October 2019; Published: date

Abstract: The development of unmanned aerial vehicle (UAV) technology and the miniaturization of sensors have changed the way remote sensing (RS) is used, popularizing this geoscientific discipline in other fields, such as precision agriculture. This makes it necessary to implement the use of these technologies in teaching RS alongside the classical platforms (satellite and manned aircraft). This manuscript describes how The Higher Technical School of Agricultural Engineering at the University of Córdoba (Spain) has introduced UAV RS into the academic program by way of project-based learning (PBL). It also presents the basic characteristics of PBL, the design of the subject, the description of the teacher-guided and self-directed activities, as well as the degree of student satisfaction. The teaching and learning objectives of the subject are to learn how to determine the vigor, temperature, and water stress of a crop through the use of RGB, multispectral, and thermographic sensors onboard a UAV platform. From the onset, students are motivated, actively participate in the tasks related to the realization of UAV flights, and subsequent processing and analysis of the registered images. Students report that PBL is more engaging and allows them to develop a better understanding of RS.

Keywords: educational assessment; motivation; unmanned aerial vehicle; agriculture

1. Introduction

Universities are tasked with improving student learning and demonstrating program effectiveness. Even though numerous teaching tools are available, teaching and learning are not singularly dependent on technology. However, as technology enhances student access to resources, we may witness a portentous shift in their learning patterns [1]. One of the primary components of effective teaching, and likewise critical to learning, is student engagement [2,3]. In Europe, as defined by the new paradigm of European Higher Education within the Bologna process, lecturers are agents that create working environments to stimulate students. In this scenario, lecturers should create and generate resources to facilitate an adequate context for learning [4]. The main factor in the learning process is the willingness to learn [5], which is dependent on the student. However, the lecturer can help students by guiding and supporting their autonomous learning. One major objective is to realize the vision of "learning to learn", in which students are trained in methods to acquire information, critical thinking, and life-long learning skills.

Remote sensing (RS) is a rapidly growing technology integrated with other disciplines, such as photogrammetry, geographic information systems (GIS), and computer science. New Earth observation programs like Copernicus [6], acquisition platforms like unmanned aerial systems (UAS) or cloud-based platforms for geospatial analysis like Google Earth Engine [7], have placed the geoscientific community, and in particular RS, in an essential position. Its importance has been recognized by different organizations [8,9] and has been identified as one of the three most important emerging disciplines [10]. Geosciences are linked to technologies related to the Earth's surface, with GIS, RS, and Global Navigation Systems (GNSS) being of key import. These technologies are joined under the term geomatics, defined as the branch of science that deals with the collection, analysis, and interpretation of data, especially instrumental data, relating to the Earth's surface.

The contents and methodologies used in educational programs for remote sensing have changed radically. At the beginning of the 1980s, most of the courses offered in the United States were provided as service courses at an introductory level [11]. However, in 2013, a review of technical education in Europe on aerospace and RS was carried out and [12]

education programs were organized into three main categories: a) "Aerospace hardware", b) "Remote sensing and image/data processing", and c) "Aerospace environmental application". The first category is focused on aircraft or satellite structure as the main objective to study construction, propulsion, motion, aerodynamics, and flight mechanics of the platforms. Included in "remote sensing and image/data processing", authors highlight programs related to data capture and processing as the main topics for RS. These are classical courses focused on the optical and radar sensors and satellite principles and the main image processing techniques. Additionally, in some cases, the educational scope is multimedia data processing, with RS being a possible application. Finally, "Aerospace environmental applications" are focused on RS for environmental purposes. The use of satellite images to create maps to monitor forests, oceans, glaciers or urban areas are some of the typical topics of courses like this. Independent of the geographic area, new technological developments in RS and photogrammetry areas demand changes in the educational programs, requiring adaptation and application of improved teaching methods [13]. Active learning methods have been proved to better motivate students, increasing their knowledge compared to traditional ways of teaching [14,15]. Active learning involves students in doing things and thinking about what they are doing [16]. In this framework, different approaches were adopted in the remote sensing field like podcasts created by students [17], inquiry-based educational experiments [18], internet-based seminars [19], and interactive online tools [20]. A successful inquiry-based educational experiment is "ESF goes to space" (College of Environmental Science and Forestry, New York, USA), where students design, build, and launch a helium balloon for acquiring images [18].

Commercial opportunities through UAS are on the rise as platform and sensor technologies are becoming more affordable. This fact is reflected in the increase of bibliographic references in recent years. Different terms fall under UAS: Unmanned aerial vehicle (UAV), remotely piloted aircraft systems (RPAS) or drone [21]. Bibliometric census using the scientific database Scopus (Figure 1) shows an increase in the number of appearances year by year (up to 15 April 2019), with UAV being the term most used. This trend also appears when adding the keyword "agriculture" to this analysis, showing the interest of its use in agronomy. Equally of note, precision agriculture (PA) is one of the most economically important sectors in the UAS market [22,23]. As such, the development of UAS in the last decade has marked a new era in RS and has become a serious "game-

changer" in PA [24], providing data of unprecedented spatial, spectral, and temporal resolution [21].

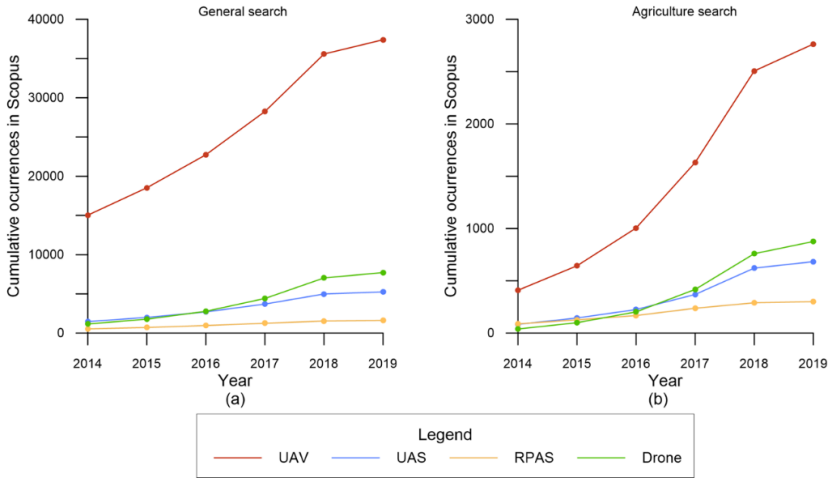

Figure 1. Cumulative of UAS technology items added to Scopus from 2014 to 2019: (**a**) General search and (**b**) Agriculture search.

Given this scenario, universities should expand their education programs, including UAV-based geomatics operations and application developments [25]. New curriculums are mainly focused, to date, on photogrammetry applications [26,27]. As a result of the interest generated by UAV applications, it is likely beneficial to introduce UAV-RS learning in those university studies related to agriculture. The goal of this manuscript is to show the teaching methodology used to do so in the Faculty of Agriculture and Forestry Engineering (Escuela Técnica Superior de Ingeniería Agronómica y de Montes, ETSIAM) at the University of Córdoba (Spain).

2. Project-Based Learning: Characteristics and Goals

One of the main objectives of engineering programs is "to produce broad-based, flexible graduates who can think integratively, solve problems, and be life-long learners" [28]. As such, it is accepted that if a combination of theory and practice are implemented into the educational programs, the educational outputs are positive for the student's learning process. Learning methods, like project-based learning (PBL), are adequate supplements to traditional teaching methods. PBL is considered an approach to teaching where students respond to real-world questions [29], providing a context of learning through problems or questions linked to

real-world practices [30], and dealing with problems that approximate real situations [31]. Therefore, the main goal of PBL is to provide students the opportunities to apply knowledge instead of simply acquiring it, with a focus on problem formulation as well as problem-solving [32]. In this context, the practice of PBL is supported by three major principles in learning:

- The constructive process: Aiding the processing of new information and developing connections to previous learning is a basic requirement for teaching and learning [33]. PBL supports learning as an act of discovery as students assess the problem, research its background, analyze a possible solution, develop a proposal, and finally generate a final result [31].
- Metacognition: The monitoring and control of thought [34]. With PBL, students are able to detect when they understand new information or not. Therefore, PBL provides the opportunity to monitor and evaluate the learning progress.
- Social and cultural factors: Learning focused on real-world context. PBL is focused on articulating problems and solving them by simulating real-world RS research and development.

As per Barrows [35], PBL characteristics are: "a) learning is student-centered, b) learning occurs in small student groups, c) lecturers are facilitators or guides, d) problems form the organizing focus and stimulus for learning, e) problems are a vehicle for the development of clinical problem-solving skills and f) new information is acquired through self-directed learning". PBL is a learning model where students actively work, plan, implement, and evaluate projects that have real-world applications [36], which is not to be confused with problem-based learning where students are focused on resolving specific problems. Therefore, PBL is a broader category of learning, where in addition to solving a specific problem, students also address other areas that are not explicit in the problem. From the lecturer's point of view, PBL has authentic objectives and uses real assessment, while the teacher acts as a coach with explicit educational objectives [37]. On the other hand, from the student's point of view, PBL stimulates collaborative and cooperative learning, allows continuous improvement in their presentations or products among others, and is designed for the student to participate actively in the resolution of the task [37]. Accordingly, the success of PBL is based on the design of adequate problems to motivate self-study. In this context, RS and GIS are areas of knowledge that allow the incorporation of new pedagogical methodologies, such as, in this case, PBL [38–40].

3. UAV-RS in Agricultural Engineering at ETSIAM (University of Cordoba)

The Higher Technical School of Agricultural Engineering (Escuela Técnica Superior de Ingenieros Agrónomos, ETSIA) at the University of Córdoba (Spain) began its academic activity in 1968, providing a degree in agricultural engineering with various specialties. In 1989, it was authorized to provide studies in forestry engineering. As a result, the school was called the Higher Technical School of Agricultural and Forestry Engineering (Escuela Técnica Superior Ingeniería Agronómica y de Montes, ETSIAM). ETSIAM offers: three bachelor programs—Agrifood Engineering and Rural Environment, Forestry Engineering, and Enology; two professional master's degrees—Agricultural Engineering, and Forestry Engineering; and eight specialized master's courses can be studied at ETSIAM. Since its inception, ETSIAM has opted to incorporate the latest technological advances in its academic programs. As an example, in 2018, a master's degree in digital transformation in the agri-food sector was implemented, where the students learn aspects related to big data, cloud computing, IoT, and others as applied to agriculture.

Since 2012, the Department of Graphic Engineering and Geomatics of ETSIAM has established UAV-RS as one of its key areas of focus with emphasis on research and teaching. Our own UAV-RS research allows our department to consolidate areas of interest in agriculture which, thereby, in terms of education, permits personal experience to form part of the educational content. In addition, our research activity through projects financed both publicly and privately, allows us to have the knowledge, experience, and materials related to UAV technology, such as flight platforms, sensors, and software. These three components are then made available to students studying UAV-RS.

Three categories of students participate in UAV-RS programs: bachelor students, master students, and PhD students. Bachelor students do not study UAV-RS, however, in recent years, some have requested an overview of these technologies, likely due to expectations and novelty. In these cases, students do their final year project on RS-UAV in agriculture. Master students have the opportunity to take a course on UAV-RS. PhD students use UAV technology in their research activities.

RS is a discipline studied throughout the programs offered by ETSIAM, while UAV studies are offered as an elective subject titled, "UAVs in the Agroforest Sector" in the second course of the master's degree in agricultural engineering. This course has four ECTS (European Credit Transfer and Accumulation System) with 40 hours of teacher-guided activities and 60 hours of self-directed activities. The activity distribution is summarized in Table 1. The purpose of this course is to provide students an opportunity to work with UAS applied to precision agriculture using RS techniques. Applying PBL, students process and analyze data that they have registered themselves using RGB, multispectral, and thermal sensors onboard UAV platforms. The main goal of this is for students to apply RS methods in orthomosaics generated from images that have been registered by sensors onboard UAV and to generate crop information to support decision making.

Table 1. Type and duration of teacher-guided and self-directed activities for "UAVs in the Agroforest Sector".

Teacher-guided activities	Time duration [hours]	Self-directed activities	Time duration [hours]
Master class	5	Analysis	20
Fieldwork	10	Study	10
Seminar	5	Group work	30
Group work	10		
Team work	10		

Figure 2 summarizes all the knowledge areas that students use together with RS in this subject. In the Bachelor of Agrifood Engineering and Rural Environment in ETSIAM, students have previously studied geodesy, photogrammetry, GIS, and RS. Specifically, the courses in photogrammetry and RS emphasize manned aerial and satellite platforms, respectively and therefore, students have previously studied the fundamentals of both geomatic disciplines. Through their academic training, students have additionally studied mathematics, physics, and statistics. Moreover, they have worked with R-commander developing scripts as a statistical tool. Due to this preparation, students are ready to work on the specific characteristics of the UAV-RS by using and applying the knowledge previously acquired in earlier courses.

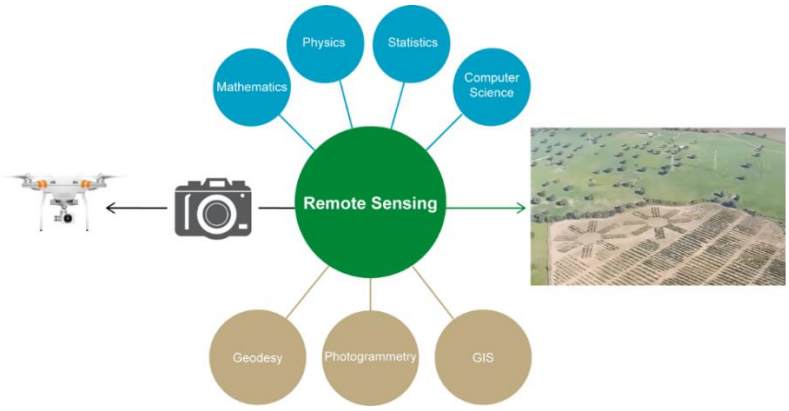

Figure 2. Knowledge areas involved in UAV-RS to transform a collection of UAV-images into useful information.

4. Systems Design and Educational Activities

The application of UAV-RS in agriculture is relatively novel. UAV-RS shares many technical and methodological aspects with satellite and manned platforms. However, it is necessary to adapt to the specific particularities that UAV-RS presents to the users. This explains the large number of scientific publications in recent years, as shown in Figure 1. In the "UAVs in the Agroforest Sector" course, students are required to generate information about the state of a crop in terms of its vigor and water needs, linking that information to the characteristics of the plot, such as soil characteristics, topography or irrigation dose. It is, therefore, not only a question of generating maps through RS but also of assessing the "why" of the results obtained. For PBL to be successful, it is essential that students collect their own data, which necessitates having the adequate materials available. Figure 3 and Table 2 summarizes all the materials with which the students work with: three flight platforms, four sensors to register images, auxiliary materials for geometric and atmospheric corrections, as well as different software solutions for the treatment of images. In addition, ETSIAM manages a "nature classroom" with different crops. Among them, there is an orchard with an area equal to 10 hectares of high-density hedgerow olive trees (north latitude 37°56′05″, west longitude 4°42′59″, WGS 84) (Figure 4) with four different variables to be analyzed: phenotype, density, orientation, and irrigation dose together with soil characteristics. This provides students a real-world case study where they can collect data via RS techniques and then convert them into information useful for assisting decision-making. This "nature classroom"

or plot, then, is the central element on which the PBL methodology is designed.

Figure 3. Materials provided to students: (**a**) UAV platforms, (**b**) sensors, (**c**) auxiliary materials and (**d**) software.

Table 2. Technical characteristics of the UAV platforms, sensors, auxiliary materials, and software used by students.

Material	Description
UAV Platforms	
Multirotor MD4-1000	Quadcopter with a maximum payload equal to 1.2 kg. Maximum flight time 30 minutes.
DJI Mavic Pro2	Quadcopter with a Hasselblad RGB sensor. Maximum flight time 30 minutes.
Elimco E-300	Fixed wind UAV with a maximum payload equal to 4 kg. Maximum flight time 90 minutes.
Sensors	
Sony Nex7	RGB sensor.
Tetracam Mini MCA-6	Multispectral sensor with six individual sensors, one for each band, arranged in a 2 × 3 array. Spectral bands equal to 450 nm, 530 nm, 670 nm, 700 nm, 740 nm, and 780 nm.
Xeneth Gobi 640	Uncooled thermal sensor. It delivers raw digital images at 16 bits. Dynamic range from –20 ºC to 120 ºC, spectral resolution equal to 0.05 ºC.
Parrot Sequoia	Multispectral sensor with an RGB sensor and four individual spectral bands at 550 nm, 660 nm, 735 nm, and 790 nm, and a sunshine sensor.
Auxiliary material	
ASD HandHeld-2	Portable spectroradiometer. Spectral range from 325 nm to 1075 nm.
Calibration panels	0.5 × 0.5 m reflectance targets.
Flir E60	Heat gun. Dynamic range from –20 ºC to 120 ºC. Resolution equal to 0.05 ºC
Leica GS15	GNSS multi-frequency receiver. Horizontal accuracy 8 mm +0.5 ppm at real-time kinematic measurement.
Vantage Pro2	Wireless weather station to measure temperature and relative humidity of the air, direction, and speed of the wind and atmospheric pressure.
Software	
Pix4D	Photogrammetry software suite for UAV mapping.
R	Software for statistical computing and computing.
QGIS	Desktop Geographic Information System

Figure 4. Location of the "nature classroom".

While students learn UAV RS, PBL allows them to acquire other competencies grouped into three classes: basic, general, and specific. Basic competencies are those referring to transversal competencies, transferable to many functions and tasks (communication, teamwork, etc.). While general competencies are those referring to successful integration into social and working life (language, new technologies, etc.). Finally, specific competencies are those directly related to a particular area of knowledge. Regarding the first group, each student learns in a highly personalized and independent way within their development and often close to the context of the research. In addition, they solve problems in new or unfamiliar environments related to their area of study, such as programming. Likewise, they acquire skills that will allow them to continue studying autonomously. For general competencies, students develop the ability to apply the acquired knowledge to solve problems, analyze the information, and synthesize it to facilitate the decision-making process. In addition, the ability to transmit information and conclusions using new communication channels is developed. Finally, and with specific character, students acquire knowledge and skills to be applied in the agricultural sector.

Table 3 summarizes teacher-guided activities and Figure 5 shows the temporal distribution. Lectures have a total duration of five hours. Firstly, students are given the rationale for learning these technologies and their applications to precision agriculture, advantages and disadvantages in terms of spatial and temporal resolution compared to other platforms, as well as when their use is justified (Table 3, L1). In addition, the student learns the legislative aspects that regulate the use of this type of platform, highlighting that today, the current legislation only allows the use of RPAS. Once the RPAS concept is introduced, the student learns what a UAS is and

the different sub-systems that it is composed of: the flight platform, sensors, and the control station (Table 3, L2). Flight platforms are analyzed from different points of view, such as architecture, autonomy, weight, and maximum flight height, providing an overview of their individual capabilities, features, and versatilities. In another session, the student learns the different sensors of interest in agriculture to be onboard a UAV (Table 3, L3): RGB, multi/hyper-spectral, thermographic, and LiDAR. An overview of the current state of sensors is made, assessing development level, possibilities, and opportunities for improvement. Finally, concepts in photogrammetry are reviewed as this was studied in the bachelor's degree (Table 3, L4) and only needs to be extended conceptually to unmanned platforms. Overall, depending on the type of sensor onboard the UAV and our experience with it, particularities and suggestions are detailed for the students.

Three seminars based on UAV-RS applications in agriculture using RGB, multispectral and thermal sensors, and one on diffusing information form part of the course. Based on scientific articles, web pages, and our own results from UAV flights, students learn different indexes and their usefulness in agriculture, such as color indices, isolating vegetation based on RGB sensors, determining the water needs through vegetation, temperature indices and so forth. These seminars are combined over time with fieldwork as the different applications of the sensor type are studied, thereby allowing students to put into practice what they have learned in the classroom. Each fieldwork assignment starts with a UAV flight. Thus, students plan the flight, use GNSS receivers to measure ground control points for geometric correction, use a thermographic gun and spectroradiometer to measure calibration panels, and then perform an atmospheric correction using the empirical line method.

The transformation of the UAV collected data to useful information for the farmer implies the generation of a series of products, such as maps or graphs, that have to be clear and easy to interpret. Today, aside from the classic analogical maps, it is necessary to provide this information digitally. For this reason, the last seminar (Table 3, S4) has been designed to present different tools for publishing geographic information through web services and applications.

Finally, three workshops are organized throughout the course. The first (Table 3, W1) is focused on the generation of digital surface models (DSM), digital elevation models (DEM) and orthomosaics from an image collection obtained from a UAV flight. The second (Table 3, W2) focuses on statistical treatments of images, atmospheric correction, and generation of

indices using R-commander. In the last workshop (Table 3, W3), students learn to automate spatial analysis processing using QGIS and the Python programming language.

Table 3. Type and duration of teacher-guided activities for "UAVs in the Agroforest Sector".

	Time duration [hours]
Lectures	
L1: Introduction and legal regulation.	1
L2: UAS and UAVs	1
L3: Sensors	1
L4: Flight planning and processing a UAV flight	2
Seminars	
S1: RGB sensor applications	1
S2: Multispectral sensor applications	1,5
S3: Thermal sensor applications	1,5
S4: Diffusion	1
Fieldwork	
F1: UAV flight RGB sensor	3
F2: UAV flight multispectral sensor	3,5
F3: UAV flight thermal sensor	3,5
Workshop	
W1: UAV flight processing	2
W2: Manage raster images using R-commander	4
W3: Process automation using QGIS	4

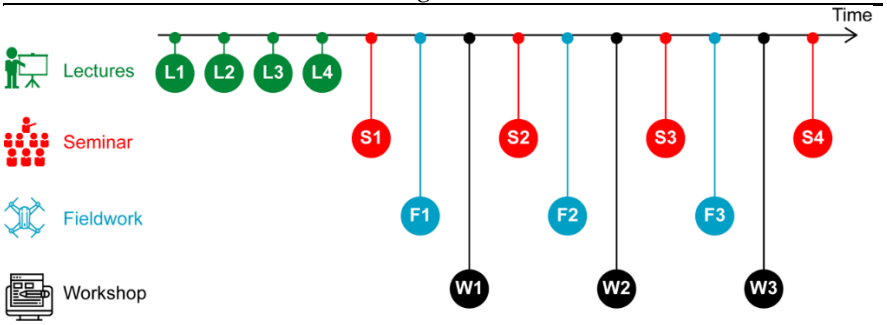

Figure 5. Temporal distribution of teacher-guided activities, lectures, seminars, fieldwork, and workshops for "UAVs in the Agroforest sector".

Teacher-guided activities support self-directed activities with the main objective being that the students are able to independently provide information about crops. Table 4 summarizes self-directed activities according to the sensor used. All in-course UAV flights have a common goal, to generate a DSM, a DEM, and an orthomosaic. Upon completion of the UAV flight, the students measure auxiliary data to perform geometric corrections from the measurements of the ground control points (GCPs) obtained from the GNSS receivers and atmospheric corrections obtained from the spectroradiometer or thermographic gun. In addition, environmental parameters such as air temperature, relative humidity, and atmospheric pressure are measured for each UAV flight. A true- color ortho-mosaic is produced using RGB images from the RGB UAV flight (F1), which is used to isolate hedgerow olive trees by a color filter. Scientific references, such as [41], are provided to the students so that they may reproduce the processing by developing an R-Commander script. Different color filters, like ExG or ExR, are implemented to later assess which one provides the best results in terms of isolating vegetation from the soil. In addition, these results are applied again in the multispectral and thermographic orthomosaics to extract the information only from the crop.

For the multispectral UAV flight (F2), once the spectral orthomosaic for each spectral band is generated, the students apply an atmospheric correction using the empirical line method. An R-Commander script is developed by the students to calculate a lineal model to relate image values and spectroradiometer measurements for each spectral band, which is later applied to generate a new set of atmospheric-corrected orthomosaics. Using these atmospheric-corrected orthomosaics, students have to calculate five vegetation indexes (VIs). NDVI and SAVI are obligatory while the students are free to calculate the rest. The calculation of these VIs is done through a script developed in Python and QGIS. Subsequently, the value of the VI relative to the crop is isolated using the mask generated from the RGB UAV flight in the previous activity and each hedgerow is statistically characterized. In addition, every tree is analyzed individually since the plantation pattern is known. This is carried out for each VI calculated so that the students once again have to automate the whole process through Python and QGIS.

Finally, a thermal orthomosaic is generated using images from a thermographic UAV flight (F3). After, atmospheric correction is applied through the empirical line method using in-field temperature measurements of panel calibrations. For that, students use the R-Commander script developed previously. Then, every hedgerow and the individual trees are thermally characterized using basic statistics.

Moreover, a crop water stress index (CWSI) model from scientific literature is applied [42].

As a result of the application of RS techniques, the student characterizes the crop, both at the level of hedgerow and individual trees. It is then necessary for the student to learn tools that agilely show the results obtained. As the final step, currently, the student learns Carto (*www.carto.com*) as a cloud-based GIS tool to present their results on different devices (tablets, smartphones or laptops). With all the information collected from the crop, the student analyzes the causes that explain the differential behavior in terms of vigor, temperature, and water stress, and generate a final report with all the results obtained.

Table 4. Input data and results of each of the self-directed activities carried out by students linked to fieldwork and seminars.

Teacher-guided activity	Input data	Results
F1: RGB UAV flight	• RGB images • GCPs	• Orthomosaic, DSM and DEM • Vegetation masks • Analysis and interpretation
F2: Multispectral UAV flight	• MSI images • GCPs • Spectroradiometer measurements	• Spectral-orthomosaic • Atmospheric correction • Vegetation indexes processing • Crop line characterization • Single tree characterization • Analysis and interpretation
F3: Thermographic UAV flight	• Thermal images • GCPs • Heat gun measurements • Weather station measurement	• Thermal-orthomosaic • Atmospheric correction • Crop Water Stress Index

		• Crop line characterization • Single tree characterization • Analysis and interpretation
S4: Diffusion	• Orthomosaics from F1, F2 and F3.	• Geographic data viewer web

5. Results

Students participate actively in the learning process by collecting field data, developing scripts, and analyzing results (Figure 6). As such, from the beginning the students are motivated and involved in the learning process, awakening the desire to learn new tools, methodologies, and RS methods with direct application in agriculture. This mainly stems from two aspects. Firstly, students have access to and use of sensors, flight platforms, and scientific-professional instruments acquired by the research group over the years. Secondly, being able to do real fieldwork on an experimental farm allows the results from RS to be subsequently validated.

(a)

(b)

Figure 6. Some teacher-guided activities: (**a**) learning about UAV platforms and (**b**) fieldwork to measure temperature and spectral signature for atmospheric corrections.

As a result of the learning process, some of the products produced by students are presented as examples in Figure 7. Using multispectral sensors, students calculate different vegetation indices (Figure 7a). Once these differences associated with the vigor of the tree have been detected, the student must analyze the cause. In the same manner, the students analyze the results obtained in the thermographic orthomosaic (Figure 7b). As in the previous case, they validate the results obtained in the field. Being able to work in the "nature classroom" allows students to personally check the characteristics of the soil or the development of the crop. In the case of Figure 7b, a relationship is shown between the temperature map and the photographs of the crop that explain and justify these differences. Finally, Figure 7c shows part of a water stress map. In this case, the students found out which area of the plot was under deficit irrigation.

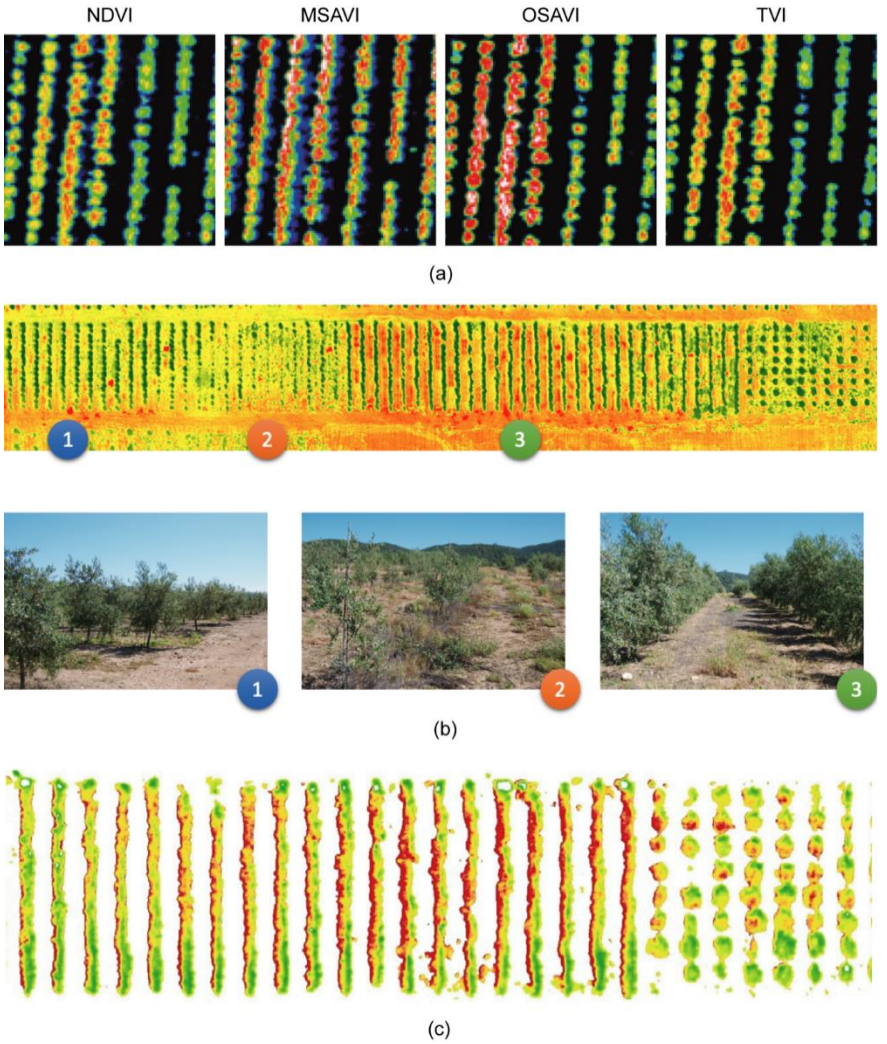

Figure 7. Examples of student results: (**a**) comparison of results of different vegetation indices, (**b**) analysis of the relationship between thermographic UAV and field inspection, and (**c**) a water stress map.

To date (2018/19 academic year), the course "UAVs in the Agroforest Sector" has been taught over four academic years. In these four editions, the University of Córdoba has surveyed students through the teaching quality system, currently with full data from the first three courses. Table 5 summarizes a total of 21 questions evaluated between 0 (lowest qualification) and 5 (highest qualification) represented in three sections including course planning, course development, and learning evaluation. Since the course's inception, students have evaluated the subject positively, marking high qualifications, close to 5 in all sections. Regarding the

"Course Planning" section, students know from the first day of the course how the subject is planned, what they are intended to do, and what capacities are to be developed and achieved throughout the course.

As related to the "Course Development" section, students evaluate whether adequate resources have been used, if the bibliography and other sources of information are useful, if the lecturer explains the contents with clarity, and if the students are interested in the subject. This section, having scored 4.56 out of 5 in the first year, is the one that has improved the most. This improvement is the sum of several factors. Firstly, the research of the teaching staff in UAV-RS is directly projected in the quality of the subject. In addition, having access to adequate instruments is an added benefit that students value positively.

In the "Learning Evaluation" section, students answer two questions: a) Do I know what will be required of me to pass the subject? and b) Are the criteria and evaluation systems adequate? The feedback received from the students encourages the department to continue with this teaching system. Year by year, students score this section higher demonstrating that students favor PBL to traditional methods, which in turn, leads to greater student engagement.

Table 5. Results of the student satisfaction survey (Values in the range between 0 and 5).

Section	2015/16	2016/17	2017/18
Course Planning	4,25	5,00	4,83
Course Development	4,56	4,69	4,77
Learning Evaluation	4,67	4,71	4,81

In addition to the results of the quality survey, our personal impression is that students value this teaching method. Being able to use these technologies in a real world-simulation field they can visit whenever they want makes them feel involved in the learning process, which results in stronger educational drivers. Of all the content of the subjects, the development of scripts is the most difficult task for them. Even so, each year students are more receptive to this kind of challenge, likely because they are progressively more aware of the undergoing technological changes in agriculture.

Although the results are positive, in order to improve the quality of the subject it is important to keep the subject dynamic, adapted, and updated in content. For this reason, the research group will start working with hyperspectral sensors in 2019. Once the knowledge and experience

acquired are adequate, these sensors will be introduced into the learning process. Furthermore, additional crops will be introduced and students will be distributed into workgroups. Each group will center on an assigned crop and the results obtained will be shared among the groups.

6. Conclusions

The university student has to acquire knowledge and skills adapted to what the labor market demands and, therefore, academic content must meet these standards. In this way, UAVs have to be introduced in higher education to teach future professional skills related to agricultural practices. This manuscript has shown how ETSIAM at the University of Cordoba has introduced UAV-RS in its educational activities using PBL. The results from the quality surveys conducted on our students have shown a very high degree of satisfaction. In our opinion this stems from the research activities of the professors and the selected teaching method. The research activity allowed our educators to gain experience and knowledge on UAV-RS and the possibility to acquire materials through privately and publicly financed projects. Moreover, PBL has shown to be conducive to the learning process. In this context, students are motivated to learn and engage in the subject from the beginning, as they see the link between the subject, their own professional interest, and what companies demand.

Active teaching methods, such as flipped classroom or team-based learning, are increasingly exposing students to new educational models, which are designed to aid students in fully understanding course material and their applications. These methods put greater emphasis on student learning and it gives them greater impetus in the process of learning. Therefore, the roles of students are changing from passive to active participants. What this means is that educators are constantly experimenting with teaching strategies and as such need to have platforms to share successes and failures in order to cultivate a more productive learning culture.

Author Contributions: Conceptualization, F-J.M-C. and A.G-F.; methodology, F-J.M-C., F.P.P., P.T-T., J.E.M.L., and A.G-F.; resources, F-J.M-C. and A.G-F.; writing—original draft preparation, F-J.M-C.; writing—review and editing, F.P.P. and P.T-T.

Funding:

Acknowledgments: The authors thank the support of the Higher Technical School of Agricultural and Forestry Engineering (Escuela

Técnica Superior Ingeniería Agronómica y de Montes) of the University of Córdoba, Spain.

Conflicts of Interest: The authors declare no conflict of interest.

References

1. Foresman, T.W.; Cary, T.; Shupin, T.; Eastman, R.; Estes, J.E.; Faust, N.; Jensen, J.R.; Kemp, K.K. Internet teaching foundation for the Remote Sensing Core Curriculum program. ISPRS J. Photogramm. Remote Sens. 1997, 52, 294–300, doi:10.1016/S0924-2716(97)00025-7.
2. Barkley, E.F. Student Engagement Techniques: A Handbook for College Faculty; John Wiley & Sons: 2009.
3. Coates, H. Student Engagement in Campus-Based and Online Education: University Connections; Routledge: 2006.
4. Romero, R.; Ferrer, A.; Capilla, C.; Zunica, L.; Balasch, S.; Serra, V.; Alcover, R. Teaching Statistics to Engineers: An Innovative Pedagogical Experience. J. Stat. Educ. 1995, 3, doi:10.1080/10691898.1995.11910481.
5. Behar Gutiérrez, R.; Grima Cintas, P. La Estadística en la Educación Superior ¿Formamos Pensamiento Estadístico? Ing. Compet. 2011, 5, 84–90, doi:10.25100/iyc.v5i2.2299.
6. Union, E. Copernicus. Europe's eyes on Earth. Available online: https://www.copernicus.eu/ (accessed on 15 April 2019).
7. Gorelick, N.; Hancher, M.; Dixon, M.; Ilyushchenko, S.; Thau, D.; Moore, R. Google Earth Engine: Planetary-scale geospatial analysis for everyone. Remote Sens. Environ. 2017, 202, 18–27, doi:10.1016/j.rse.2017.06.031.
8. Council, N.R. Future US Workforce for Geospatial Intelligence; National Academies Press: 2013.
9. United States Department of Labor. High Growth Industry Profile—Geospatial Technology; 2010.
10. Gewin, V. Mapping opportunities. Nature 2004, 427, 376–377, doi:10.1038/nj6972-376a.
11. Jensen, J.R.; Dahlberg, R.E. Status and content of remote sensing education in the United States. Int. J. Remote Sens. 1983, 4, 235–245, doi:10.1080/01431168308948543.
12. Dell'Acqua, F.; Pasca, L. Technical Education in the European University System on Aerospace and Remote Sensing: A Year 2013 Review [Education]. IEEE Geosci. Remote Sens. Mag. 2014, 2, 29–33, doi:10.1109/MGRS.2014.2304131.
13. Fras, M.K.; Grigillo, D. Implementation of active teaching methods and emerging topics in photogrammetry and remote sensing subjects. Int. Arch. Photogramm. Remote Sens. Spat. Inf. Sci. 2016, 41, doi:10.5194/isprsarchives-XLI-B6-87-2016

14. Azzalis, L.; Sato, S.; de Mattos, M.; Fonseca, F.; Giavarotti, L. Active learning versus traditional teaching. Rev. Ensino Bioquím. 2009, 7, 2.
15. Weltman, D. A Comparison of Traditional and Active Learning Methods: An Empirical Investigation Utilizing a Linear Mixed Model; University of Texas: Austin, TX, USA, 2008.
16. Bonwell, C.C.; Eison, J.A. Active Learning: Creating Excitement in the Classroom; ERIC Digest: 1991.
17. Guida, R. Introduction of podcasts in remote sensing education. In Proceedings of the 2010 IEEE International Geoscience and Remote Sensing Symposium, Honolulu, HI, USA, 25–30 July 2010; pp. 1104–1106.
18. Mountrakis, G.; Triantakonstantis, D. Inquiry-Based Learning in Remote Sensing: A Space Balloon Educational Experiment. J. Geogr. High. Educ. 2012, 36, 385–401, doi:10.1080/03098265.2011.638707.
19. Baldina, E.A.; Chalova, E.R.; Knizhnikov, Y.F.; Tutubalina, O.V. Remote sensing education using Internet—Prospects of the Inter-University Aerospace Centre. In Proceedings of the IEEE International Geoscience and Remote Sensing Symposium, Toronto, Canada, 24–28 June 2002.
20. Joyce, K.E.; Boitshwarelo, B.; Phinn, S.R.; Hill, G.J.E.; Kelly, G.D. Interactive online tools for enhancing student learning experiences in remote sensing. J. Geogr. High. Educ. 2014, 38, 431–439, doi:10.1080/03098265.2014.933404.
21. Colomina, I.; Molina, P. Unmanned aerial systems for photogrammetry and remote sensing: A review. ISPRS J. Photogramm. Remote Sens. 2014, 92, 79–97, doi:10.1016/j.isprsjprs.2014.02.013.
22. Singh, K.K.; Frazier, A.E. A meta-analysis and review of unmanned aircraft system (UAS) imagery for terrestrial applications. Int. J. Remote Sens. 2018, 39, 5078–5098, doi:10.1080/01431161.2017.1420941.
23. Mazur, M.; Wisniewski, A.; McMillan, J. Clarity from Above. PwC Global Report on the Commercial Application of Drone Technology; 2016.
24. Maes, W.H.; Steppe, K. Perspectives for Remote Sensing with Unmanned Aerial Vehicles in Precision Agriculture. Trends Plant Sci. 2019, 24, 152–164, doi:10.1016/j.tplants.2018.11.007.
25. Al-Tahir, R. Integrating UAV into geomatics curriculum. Int. Arch. Photogramm. Remote Sens. Spat. Inf. Sci. 2015, 40, 387.
26. Elaksher, A. Modernizing the Photogrammetry Curricula with Small Unmanned Aerial Systems. Surv. Land Inf. Sci. 2018, 77, 75–84.
27. Pereira, E.R.; Zhou, S.; Gheisari, M. Integrating the use of UAVs and photogrammetry into a construction management course: Lessons learned. In the International Symposium on Automation and Robotics in Construction; IAARC Publications: 2018; pp. 1–8.
28. Matthew, R.G.S.; Hughes, D.C. Getting at deep learning: A problem-based approach. Eng. Sci. Educ. J. 1994, 3, 234–240.

29. Lattimer, H.; Riordan, R. Project-Based Learning Engages Students in Meaningful Work. Middle Sch. J. 2011, 43, 18–23, doi:10.1080/00940771.2011.11461797.
30. Wurdinger, S.; Haar, J.; Hugg, R.; Bezon, J. A qualitative study using project-based learning in a mainstream middle school. Improving Sch. 2007, 10, 150–161, doi:10.1177/1365480207078048.
31. Delisle, R. How to Use Problem-Based Learning in the Classroom; 1997.
32. Brodeur, D.R.; Young, P.W.; Blair, K.B. Problem-based learning in aerospace engineering education. In Proceedings of the 2002 American Society for Engineering Education Annual Conference and Exposition, Montreal, Canada.
33. Gijselaers, W.H. Connecting problem-based practices with educational theory. New Dir. Teach. Learn. 1996, 1996, 13–21, doi:10.1002/tl.37219966805.
34. Martinez, M.E.J.P.d.k. What is metacognition? 2006, 87, 696–699.
35. Barrows, H.S. Problem-based learning in medicine and beyond: A brief overview. 1996, 68, 3–12, doi:10.1002/tl.37219966804.
36. Harwell, S. Project-Based Learning. Promising Practices for Connecting High School to the Real World; 1997; Volume 2328.
37. Martí, J.A.; Heydrich, M.; Rojas, M.; Hernández, A. Aprendizaje basado en proyectos. Rev. Univ. EAFIT 2010, 46.
38. Drennon, C. Teaching Geographic Information Systems in a Problem-Based Learning Environment. J. Geogr. High. Educ. 2005, 29, 385–402, doi:10.1080/03098260500290934.
39. Botti, J.A.; Myers, R. Exploring the environment: A problem-based approach to learning about global change. In Proceedings of the 1995 International Geoscience and Remote Sensing Symposium, IGARSS'95. Quantitative Remote Sensing for Science and Applications, Firenze, Italy, 10–14 July 1995.
40. Croft, S.K.; Myers, R.J. Helping students and teachers make sense of remote sensing via the Internet. In Proceedings of the IGARSS'96. 1996 International Geoscience and Remote Sensing Symposium, Lincoln, NE, USA, 31 May 1996.
41. Guijarro, M.; Pajares, G.; Riomoros, I.; Herrera, P.J.; Burgos-Artizzu, X.P.; Ribeiro, A. Automatic segmentation of relevant textures in agricultural images. Comput. Electron. Agric. 2011, 75, 75–83, doi:10.1016/j.compag.2010.09.013.
42. Egea, G.; Padilla-Díaz, C.M.; Martinez-Guanter, J.; Fernández, J.E.; Pérez-Ruiz, M. Assessing a crop water stress index derived from aerial thermal imaging and infrared thermometry in super-high density olive orchards. Agric. Water Manag. 2017, 187, 210–221, doi:10.1016/j.agwat.2017.03.030.

6 CAPÍTULO 3

remote sensing

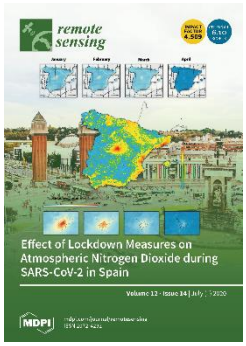

Article

Effect of Lockdown Measures on Atmospheric Nitrogen Dioxide during SARS-CoV-2 in Spain

Francisco-Javier Mesas-Carrascosa *, Fernando Pérez Porras, Paula Triviño-Tarradas, Alfonso García-Ferrer and Jose Emilio Meroño-Larriva

Department of Graphic Engineering and Geomatics, Campus de Rabanales, University of Cordoba, 14071 Córdoba, Spain; o12pepof@uco.es (F.P.P.); ig2trtap@uco.es (P.T.-T.); agferrer@uco.es (A.G.-F.); ir1melaj@uco.es (J.E.M.-L.)
* Correspondence: fjmesas@uco.es

Received: 1 June 2020; Accepted: 8 July 2020; Published: 10 July 2020

Publicado en: **Remote Sensing, 2020, 12(14), 2210**

https://doi.org/10.3390/rs12142210

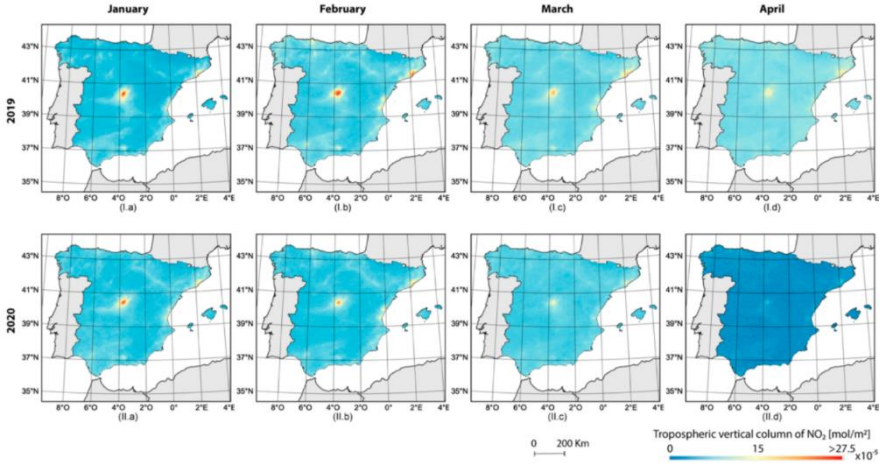

Article

Effect of Lockdown Measures on Atmospheric Nitrogen Dioxide During SARS-CoV-2 in Spain

Francisco-Javier Mesas-Carrascosa *, Fernando Pérez Porras, Paula Triviño-Tarradas, Alfonso García-Ferrer and Jose Emilio Meroño-Larriva

Department of Graphic Engineering and Geomatics, Campus de Rabanales, University of Cordoba, 14071 Córdoba, Spain; o12pepof@uco.es (F.P.P.); ig2trtap@uco.es (P.T.-T.); agferrer@uco.es (A.G.-F.); ir1melaj@uco.es (J.E.M.-L.)

* Correspondence: fjmesas@uco.es

Received: 01 June 2020; Accepted: 08 July 2020; Published: date

Abstract: The disease caused by SARS-CoV-2 has affected many countries and regions. In order to contain the spread of infection, many countries have adopted lockdown measures. As a result, SARS-CoV-2 has negatively influenced economies on a global scale and has caused a significant impact on the environment. In this study, changes in the concentration of the pollutant Nitrogen Dioxide (NO_2) within the lockdown period were examined as well as how these changes relate to the Spanish population. NO_2 is one of the reactive nitrogen oxides gases resulting from both anthropogenic and natural processes. One major source in urban areas is the combustion of fossil fuels from vehicles and industrial plants, both of which significantly contribute to air pollution. The long-term exposure to NO_2 can also cause severe health problems. Remote sensing is a useful tool to analyze spatial variability of air quality. For this purpose, Sentinel-5P images registered from January to April of 2019 and 2020 were used to analyze spatial distribution of NO_2 and its evolution under the lockdown measures in Spain. The results indicate a significant correlation between the population's activity level and the reduction of NO_2 values.

Keywords: nitrogen dioxide; SARS-Cov-2; Sentinel-5P; air pollution

1. Introduction

Clean air is an essential requirement for human health, and as such air pollution is a major threat to human well-being. Air pollution is the largest environmental health risk in many regions around the world. The World Health Organization estimates that air pollution kills 7 million people worldwide every year, making it necessary to monitor air pollution and improve air quality [1]. The environmental impact is more evident in areas where population density is high, being particularly severe in megacities where high population density, extensive motor vehicle use and strong industrial expansion are combined [2]. Poor air quality is not exclusive to megacities; even small cities with populations around 150,000 can have this problem [3]. Therefore, the economic development of cities with expanding industrial areas is associated with increasing population size and environmental degradation of the surrounding areas [4]. In addition, the high levels of motor vehicle activity [5] and their inappropriate use [6] cause an increase of air pollutants in city centers [7]. As a result, quality of life and human health is worsening specifically in cardiovascular, neurological, and respiratory diseases [8–10] and even results in higher mortality rates [11,12]. As a consequence of this, developed and developing countries are more and more attentive to urban air quality, developing guidelines, directives and standards to inform and support policymakers [13,14] to reduce the health impacts of air pollution.

Common pollutants in the troposphere, the innermost layer of Earth's atmosphere, include ozone (O_3), carbon monoxide (CO), sulfur dioxide (SO_2), nitrogen dioxide (NO_2) and aerosols. NO_2, specifically, has been correlated with mortality in studies in different parts of the world [15,16]. It is true, however, that there is no clear evidence to establish that NO_2 acts as an independent agent causing increases in the mortality rate [17]. Rather, it is widely believed that NO_2 could act as a substitute component for others that are not currently being monitored or, more broadly, as a mixture of pollutants [18]. The result is that NO_2 is included in the multi-pollutant health indexes [19]. Epidemiological research and studies have shown how NO_2 is related to adverse health effects like lung cancer [20,21], asthma exacerbations [22,23] and cardiopulmonary mortality [24,25]. Mainly, NO_2 forms from ground-level emissions caused by the burning of fossil fuels from industrial sources, vehicles and power plants. It contributes to ground-level ozone formation and it is linked to negative effects on respiration. For example, NO_x reacts with moisture, ammonia and other compounds to form small particles that can penetrate into sensitive parts of the lungs.

Traditionally, air pollution is monitored using a networks of sensors, such as gas chromatograph-mass spectrometers [26] or ultraviolet sensors [27], among others, which are distributed over a territory and provide quality information on a wide range of pollutants. The traditional instrumentation used for air quality monitoring is expensive, large, location dependent and yields extremely low spatial and temporal resolution [28]. For this reason, portable environmental sensor systems have been developed using Wireless Sensor Network technology at a lower cost, offering data with a higher frequency over time. They are also easier to relocate and provide better coverage of the area of interest due to allowing the use of a larger number of nodes [29,30], permitting the development of more efficient and accurate air quality models [31]. Despite these advantages, however, it is not possible to map a broad region. Advances in atmosphere remote sensing have opened new avenues for measuring and monitoring atmospheric pollution at local, regional, continental or global scales [32], providing new challenges and opportunities for environmental health research [33]. The ability to observe and monitor air pollutants from sensors onboard satellite platforms has improved in the last two decades. From the first ultraviolet-visible spectrometer, the Global Ozone Monitor Experiment (GOME), with a spatial resolution equal to 40 × 320 km^2 [34], followed by the SCanning Imaging Absorption SpectroMeter for Atmospheric CHartography (SCIAMACHY), with a pixel size of 30 × 60 km^2 [35], and GOME-2, 40 × 80 km^2 [36] to the Ozone Monitoring Instrument, 13 × 24 km^2 [37] it has been possible to study the distribution of pollutants at urban scales. Recently, the European Space Agency launched the Sentinel-5 Precursor (S5P) to provide data on air quality, the climate and the ozone layer using the TROPOspheric Monitoring Instrument (TROPOMI) as its payload [38] providing a significant improvement in data quality and spatial resolution now at 7 × 7 km^2 [39]. The spectral bands of the spectrometer TROPOMI ranges from ultraviolet, visible, near infrared and shortwave infrared, allowing the observation of the prevalence of aerosols in the atmosphere, cloud characteristics, concentrations of carbon monoxide (CO), formaldehyde (CH_2O), nitrogen dioxide (NO_2), ozone (O_3), sulphur dioxide (SO_2) and methane (CH_4). The Tropospheric Vertical Column Density (VCD) data of these components are measured from space by sensors like TROPOMI which serves as an accurate proxy at ground level in many air quality applications [40]. The VCD is defined as the number of molecules of a certain atmospheric gas between the on-board sensor of the satellite platform and the Earth's surface per unit area. Tropospheric and stratospheric column densities are separated using a data assimilation system based on the three-dimensional global Tracer chemical Transport

Model (TM5-MP), after which they are converted to VCD by a look-up table of altitude dependent air-mass factors and information on the vertical distribution of NO_2 [41]. For NO_x, VCD measurements have been successfully used to estimate trends and variations in atmospheric concentration [42,43], infer surface emissions [44,45] and monitor emission changes at a given location [46,47].

Since mid-February 2020, all efforts of many countries were directed towards combating SARS-CoV-2. However, at the beginning of 2020, the risk of a pandemic from a virus was not among the perceived risks worldwide. This year was the first time that the World Economic Forum's Global Risk Report showed how climate change and environmental risks were among the top positions [48]. However, both problems are associated, the origin of new pathogens, such as SARS-CoV-2, may be explained by environmental degradation. The coronaviruses have been known about since 1930 [49]. They are transmitted from animals [50] and have been increasing in number over the last decades [51]. The degradation of natural spaces from human activity is increasing the rate of contact between wild spaces and humans, resulting in new diseases and facilitating their expansion [52–54]. Nevertheless, while many believe that the climate, and therefore the environment is changing, some think this is not attributable to human activity [55], which may be due to their perception of cultural values [56] or ideologically and politically motivated actors [57].

Unfortunately, the spread of the coronavirus SARS-Cov-2 has been unstoppable and has become a pandemic [58], with dramatic results in countries like Spain, Italy and the United Kingdom [59] in Europe's case. Interventions like quarantine or isolation have shown to be effective in reducing the number of SARS-CoV-2 infections [60]. In addition, some countries and regions have deemed it necessary to impose lockdown measures on economic activities and with unprecedented travel restrictions [61,62]. Under this lockdown period, changes in air pollution can provide valuable information on air quality improvement when there are restrictions on emissions. In this manuscript, using Sentinel S5P images, we analyze the spatial and temporal variation of NO_2 concentrations during Spain's SARS-Cov-2 lockdown phase which took place in March and April 2020, and how these variations are related to city-scale demographics.

2. Materials and Methods

2.1. Study Area

Spain has just over 47 million inhabitants as of 1 January 2020. Although unevenly distributed throughout the territory, the average population density is equal to 82 habitants per km^2. Figure 1 shows population density using the European Environment Agency 10 × 10 km grid as a reference. There are areas with highly concentrated populations next to areas of demographic voids. The factors that explain this unbalanced population distribution in Spain are both natural and historical. Regarding natural factors areas with flat and low-lying relief, with a temperate and humid climate and access to the sea and rivers are the most populated. As far as historical factors are concerned, the distribution of the population is related to the economic structure of the country and the development of transport and communication infrastructure. As a result, the average population density in Spain is 416 inhabitants per square kilometer, with very high density areas, over 750 habitants per square kilometer, compared to others with very low densities.

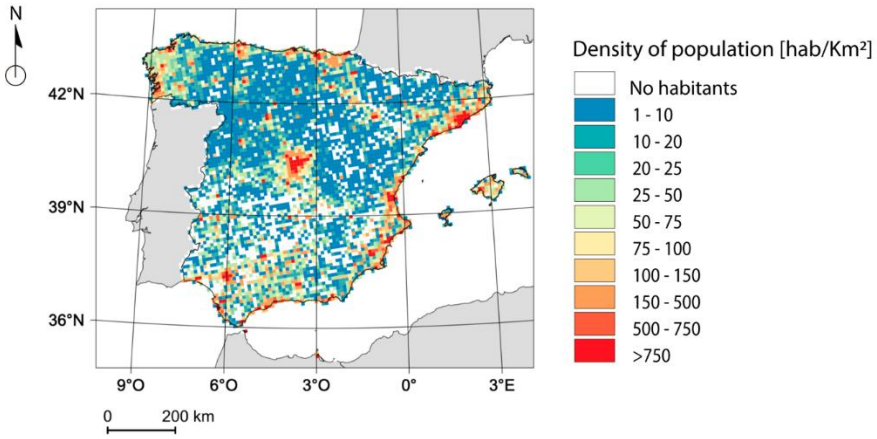

Figure 1. Distribution of population density in Spain on a 10 × 10 km grid.

Figure 2 shows the location of cities with more than 275,000 inhabitants, with the highest concentrations in Madrid, having more than 3 million inhabitants, and Barcelona, with just over 1.6 million. The relationship between the number of inhabitants in these eleven cities and the variation of NO_2 VCD under the lockdown measures is the focus of this analysis.

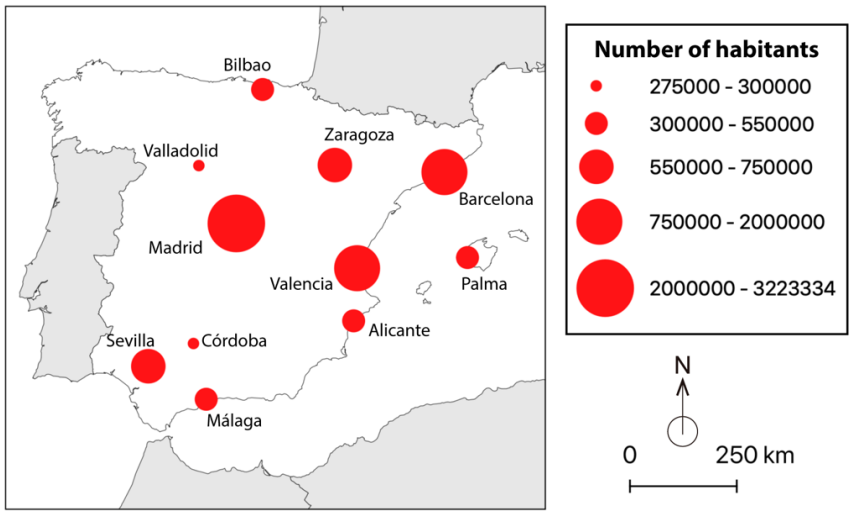

Figure 2. Location of the eleven most populated cities in Spain.

2.2. Remote Sensing Image Collections

The TROPOMI on-board the Sentinel-5 Precursor (Sentinel-5P) was used to collect data on NO_2 concentration. The Sentinel-5P mission, launched by the European Space Agency in 2017, is a low-orbit polar satellite used to monitor Earth's atmosphere with a high spatio-temporal resolution using the TROPOMI. Concretely, it is a multispectral sensor that registers reflectance values at ultraviolet-visible (250–500 nm), near-infrared (675–775 nm) and short-wave infrared (2305–2385 nm) wavelengths which measures concentrations of ozone, methane, formaldehyde, aerosols, carbon monoxide, nitrogen oxide and sulphur dioxide as well as cloud characteristics like cloud fraction, cloud base and pressure.

Image processing was performed with the Google Earth Engine, a cloud-based platform for geospatial analysis with high computational capabilities [63]. A total of 1637 Sentinel 5P Nitrogen Dioxide level-3 scenes of Spain from January to April of 2019 were used and 1636 scenes from the same period were used from 2020 (Table 1). Thus, Sentinel 5P Level-2 data [64] are processed to obtain a single grid per orbit, which allows the Google Earth Engine to process the data. In addition, the data are previously filtered, resulting in pixels with quality assurance values less than 75% being removed, such as cloud or partially snow-covered pixels, errors and or problematic retrievals. First, for each month and year a median image was generated to represent the time series of the images, obtaining an individual image for each time period. Thus, each pixel in the output image

was equal to the median value of all the images at that location. On the NO_2 median images, once masked for the geographical space of Spain, the statistics corresponding to maximum, minimum, median, and 2nd and 3rd quartile were determined. This allowed a space-time comparison of the NO_2 VCD throughout the year and between years.

In addition, the variation of NO_2 VCD before and after the lockdown measures was determined. Thus, taking 15 March 2020 as a time reference, the day on which the lockdown measures became effective in Spain, a median image was calculated to represent the NO_2 VCD one month before and after the adoption of these measures, and the variation of this component was then determined. For the most populated cities in Spain, the average value of variation of NO_2 VCD was determined in order to analyze its relationship with the number of inhabitants per city.

Table 1. Number of Sentinel-5P scenes used per month and year.

Month	2019	2020
January	426	424
February	382	379
March	426	426
April	403	407
Total	1637	1636

3. Results

European countries have established differing lockdown measures in order to control the spread of the SARS-CoV-2 outbreak. These measures, imposed at varying degrees, were implemented at different moments during the second half of March 2020 and have restricted freedom of movement and outlawed public meetings. Italy and Spain were the first countries in Europe to implement these measures on 11 and 14 March 2020, respectively. Taking 15 March 2020 as a time reference, Figure 3 shows the evolution of NO_2 VCD in the troposphere at a European scale one month before and after the adoption of the lockdown measures and compares it to the concentration in the same period during the year 2019. At this scale of detail, it can be seen that the highest NO_2 VCD distribution values appears in central Europe, large European cities and some urban areas of the Mediterranean basin. One month before March 15, both in 2019 (Figure 3a.I) and 2020 (Figure 3b.I), the regional distribution of the average NO_2 VCD around Milan, Paris, Madrid, London showed values higher than 0.0002 mol m^{-2}. Likewise, between 15 March and 15 April 2019 (Figure 3a.II), NO_2 VCD distribution was maintained around the previously

described urban areas. However, for the same period in 2020 (Figure 3b.II) these extreme values greatly declined, coinciding with the lockdown period.

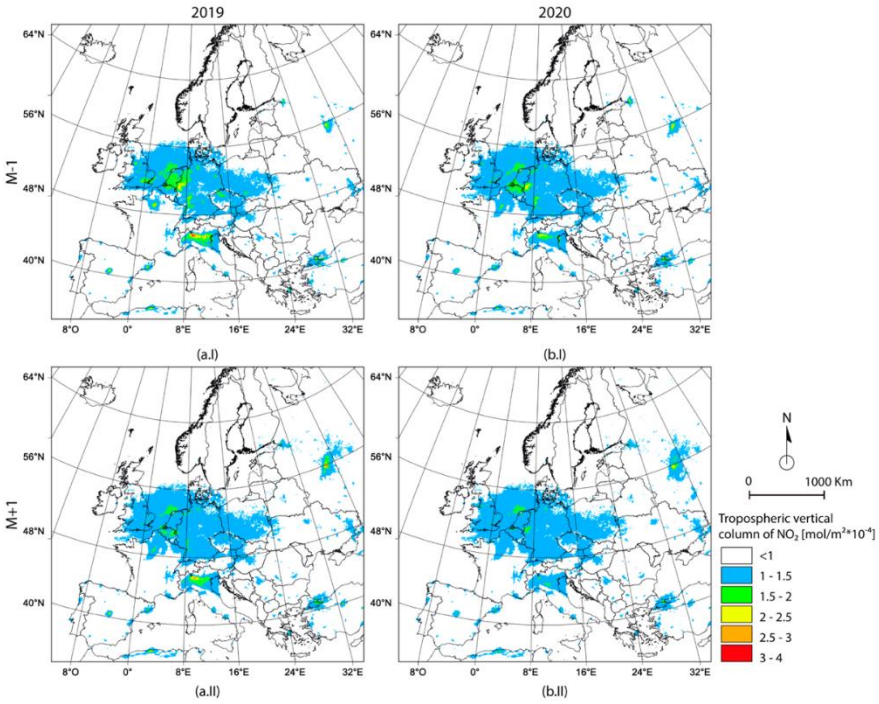

Figure 3. Comparison in Europe of the evolution of the average NO_2 content in the troposphere one-month (**I**) before and (**II**) after March 15, (**a**) 2019 and the same period in (**b**) 2020.

Figure 4 shows the box and whisker plot and Table 2 the statistic description of NO_2 VCD in Spain for 2019 and 2020 from January to April. A wide range of NO_2 VCD values were observed (Figure 4a), especially in January and February of both years. The maximum values were reduced in March and April, especially in 2020, and declined sharply in April 2020, coinciding with mobility restrictions. On the other hand, the minimum values did not fluctuate, maintaining similarity throughout the months of both years. Median, quartile 25% and 75% values were closer to the minimum values, showing the presence of geographical areas with higher values of NO_2 VCD than the rest. Figure 4.a shows how the range of NO_2 was reduced in March and April in the two years. However, while in 2019 the distribution was very similar, this was not the case in 2020. In March 2020, the reduction in the range of NO_2 VCD was more pronounced than in the same month of the previous year. In April 2020, the reduction was much

more pronounced, coinciding with mobility restrictions. Figure 4b shows in detail the evolution of the distribution of NO_2 VCD around the median values. During 2019, the median values were similar, ranging from 2.08 × 10^{-5} to 2.19 × 10^{-5} mol m^{-2} in January and February, respectively. Contrariwise, in 2020, the median values of NO_2 did not show the same stable behavior of the previous year. January 2020 showed the highest value, 2.75 × 10^{-5} mol m^{-2}, reducing slightly in February, although it was still higher than the previous year's values. However, in the month of March 2020 there was a very pronounced reduction of NO_2 in April 2020, with a median value equal to 1.65 × 10^{-5} mol m^{-2}, the lowest value of all the months analyzed. In addition, the interquartile range in the months of March and April 2020 was smaller and therefore the distribution of NO_2 was more homogeneous throughout the territory.

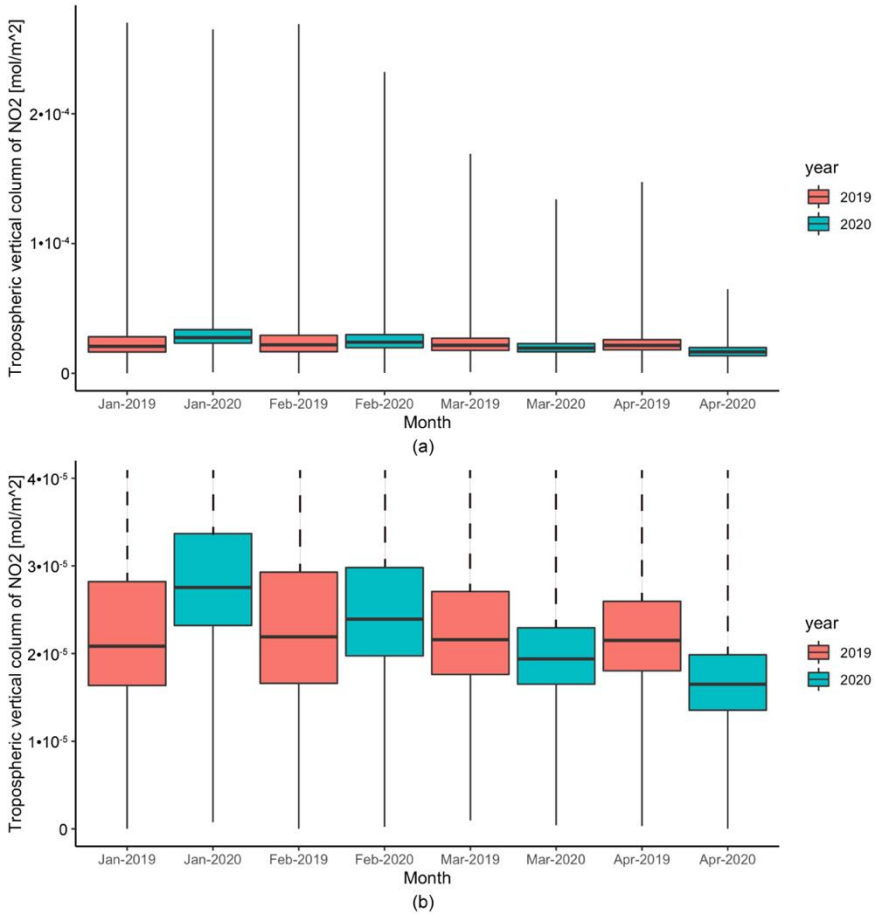

Figure 4. Whisker box plot with the monthly evolution of NO_2 in 2019 and 2020 taking into account (**a**) the whole range of values and (**b**) zoom on the median values.

Table 2. Descriptive statistics of NO_2 concentration by month and year.

Month	Year	Minimum	Maximum	Q25	Median	Q75
January	2019	1.46×10^{-9}	0.00027	1.64×10^{-5}	2.08×10^{-5}	2.82×10^{-5}
	2020	7.63×10^{-7}	0.000265	2.32×10^{-5}	2.75×10^{-5}	3.37×10^{-5}
February	2019	7.41×10^{-9}	0.000269	1.66×10^{-5}	2.19×10^{-5}	2.93×10^{-5}
	2020	2.4×10^{-7}	0.000232	1.97×10^{-5}	2.39×10^{-5}	2.98×10^{-5}
March	2019	9.56×10^{-7}	0.000169	1.76×10^{-5}	2.16×10^{-5}	2.71×10^{-5}
	2020	4.12×10^{-7}	0.000134	1.65×10^{-5}	1.94×10^{-5}	2.29×10^{-5}
April	2019	3.32×10^{-7}	0.000148	1.8×10^{-5}	2.15×10^{-5}	2.6×10^{-5}
	2020	1.25×10^{-8}	6.49E-05	1.35×10^{-5}	1.65×10^{-5}	1.99×10^{-5}

Figure 5 shows the temporal evolution of the spatial distribution of NO_2 VCD in the January–April period for the years 2019 and 2020 in Spain. During the year 2019 (Figure 5I.x), Madrid and the surrounding metropolitan area was the one with the highest values of NO_2 VCD. In addition, the metropolitan areas of Barcelona and Valencia, in the Mediterranean basin, and Seville in southern Spain, stand out in NO_2 VCD values, although much lower than Madrid. These areas correspond to the areas with the highest NO_2 VCD values represented in the box and whisker plot of Figure 4a. As shown in this figure, these urban areas appear more highlighted in the months of January (Figure 5I.a) and February (Figure 5I.b) than in the months of March (Figure 5I.c) and April (Figure 5I.d) in 2019, although these areas presented higher values than the rest of Spain. In 2020 (Figure 5II.x), the distribution of NO_2 VCD was similar to that of 2019 in the months of January (Figure 5II.a) and February (Figure 5II.b), with the same urban areas standing out as in 2019 due to their increase in NO_2. In March 2020, coinciding with the middle of the month in which mobility restriction measures were adopted, a reduction in NO_2 VCD was

observed throughout the country, with only the geographical area around Madrid showing higher values than the rest of Spain, although lower than in previous months. Finally, in April 2020 (Figure 5II.d), where the mobility restrictions measures were applied throughout the month, there was a very marked reduction in NO_2 VCD throughout the totally of Spain, with strongly homogeneous behavior and hardly any variation.

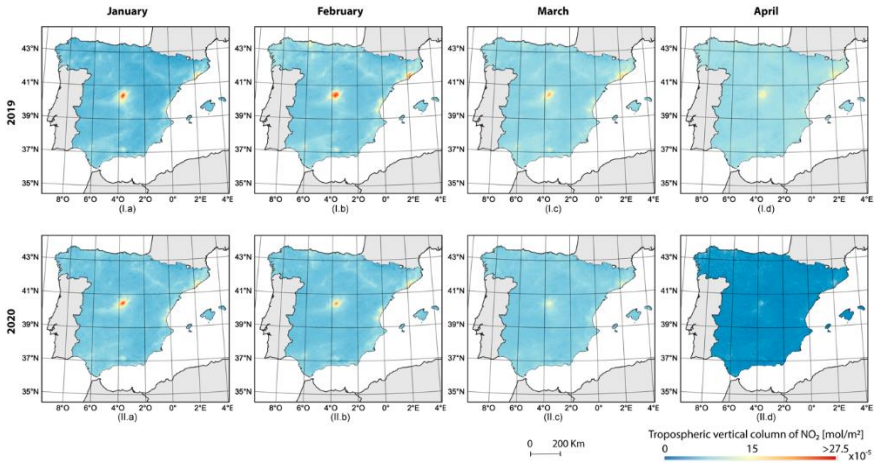

Figure 5. Monthly maps of average values of Tropospheric vertical column of NO_2 in Spain for the years (**I**) 2019 and (**II**) 2020 during the months of (**a**) January, (**b**) February, (**c**) March and (**d**) April.

Figure 6 presents the evolution in detail of NO_2 VCD over the three most populated cities in Spain, Madrid (Figure 6a.x), Barcelona (Figure 6b.x) and Valencia (Figure 6c.x), between January and April 2020. Of the three cities, Madrid presented the highest NO_2 VCD values at the beginning of 2020. In the month of January, both Madrid (Figure 6a.I) and Barcelona (Figure 6b.I), due to the size of their metropolitan areas and number of inhabitants, showed higher values in the center of these areas, reducing radially as the distance increases from the central area. In February, there was a reduction in NO_2 in the city of Madrid (Figure 6a.II), but not in the cities of Barcelona (Figure 6b.II) and Valencia (Figure 6c.II). These geographical areas presented higher values than the surrounding areas. In March, coinciding with the limitation of mobility and activity in the middle of the month, a reduction in NO_2 was observed in the three urban areas. In the case of Madrid (Figure 6a.III), the highest NO_2 values appeared around the city and not in the metropolitan area. A similar NO_2 spatial distribution occurred in Barcelona (Figure 6b.III). On the other hand, the city of Valencia and its metropolitan area (Figure 6c.III) present very similar NO_2 values. The effect of mobility restrictions is very evident in the month of April 2020.

All analyzed urban areas showed a drastic decrease in NO_2 VCD, only Madrid (Figure 6a.IV) and, to a lesser extent, Barcelona (Figure 6b.IV) showed a very slight increase in values with respect to the surrounding areas for the same period, making it practically impossible to identify a pattern associated with the urban area. In the case of Valencia (Figure 6c.IV) this difference vanished completely. Thus, after 30 days of limitations and restrictions in mobility and activity, the values of NO_2 CDV in these urban areas were similar to those of non-urban areas.

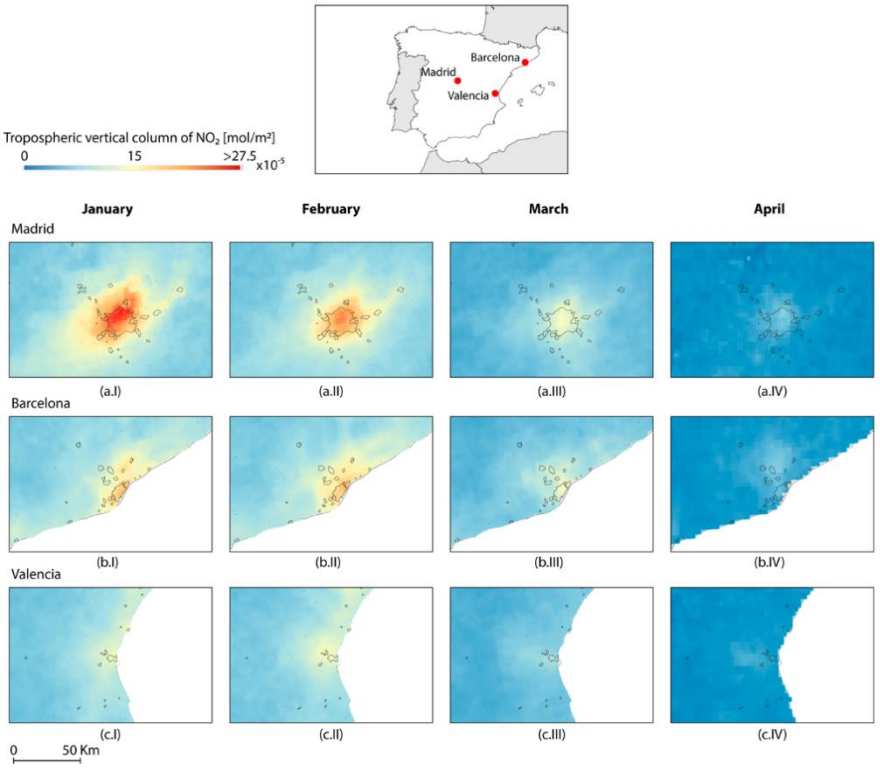

Figure 6. Monthly maps of average values of Tropospheric vertical column of NO_2 in (**a**) Madrid, (**b**) Barcelona and (**c**) Valencia for 2020 during the months of (**I**) January, (**II**) February, (**III**) March and (**IV**) April.

Figure 7 shows the variation of NO_2 VCD from one month before to one month after 15 March 2020 in Spain. The highest NO_2 VCD reductions are represented in red, while a severe reduction is represented in yellow. On the other hand, those areas with a low reduction are represented in green and those areas with no discernible variation are in cyan. Throughout the territory, a decrease can be observed after the lockdown measures, with

some areas showing a more pronounced decrease than others. The variation of NO_2 followed the same spatial distribution as the population density distribution presented in Figure 1. The city of Madrid, the most densely populated city in Spain, showed a marked reduction in NO_2 concentration, reaching values of -1.56×10^{-4} mol m^{-2}. Slightly lower values were found in areas such as Barcelona, Valencia and some coastal urban areas with a lower population density than Madrid. On the other hand, all these areas were surrounded by metropolitan areas where the reduction in NO_2 was much less pronounced but also important, with values around -0.08×10^{-4} mol m^{-2}. Similar values were found in cities such as Seville and its metropolitan area, Valladolid and the Ebro River corridor. The rest of the territory, with lower population densities presented a reduction between 0.04×10^{-4} and 0.01×10^{-4} mol m^{-2}, lower than metropolitan areas. Therefore, the most densely populated areas with high NO_2 concentrations showed the greatest reductions compared to those areas with low density populations. As a result, the distribution of NO_2 VCD in Spain was more homogeneous than in previous months (Figure 5II.d).

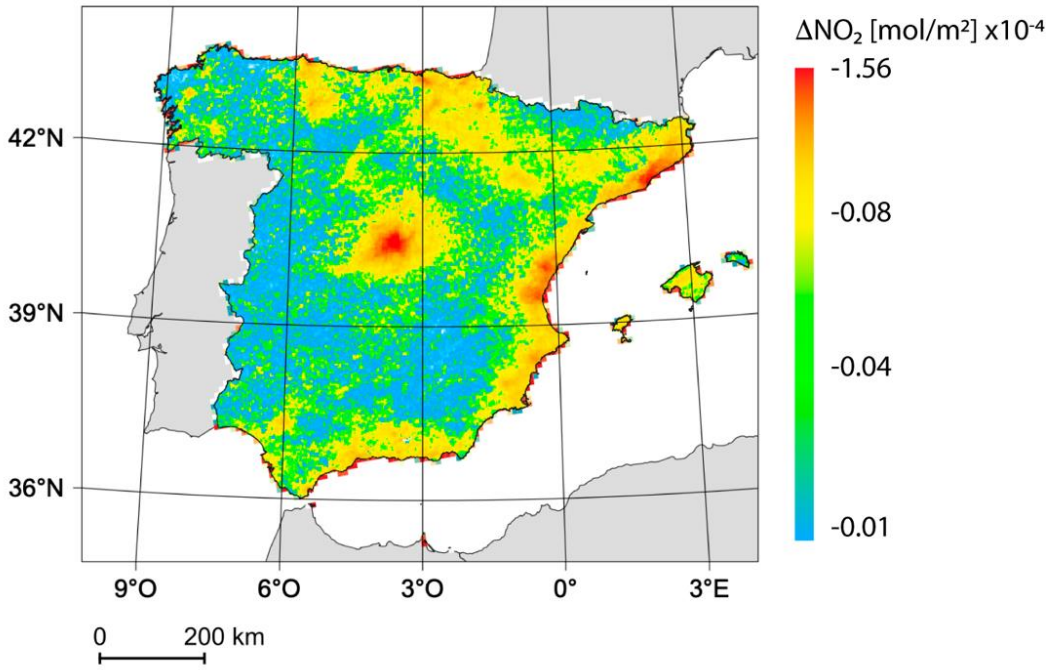

Figure 7. Mean variation of NO_2 VCD between one month before and after 15 March 2020 in Spain.

Figure 8 shows the average value of tropospheric VCD of NO_2 reduction in relation to the number of inhabitants, resulting in nine categories. In general, as the number of inhabitants increases, NO_2 decreases. Cities with less than 50,000 inhabitants had least significant reduction, with an average value of -2.99×10^{-5} mol m^{-2}. On the other hand, those cities with more than 600,000 inhabitants were those that presented the greatest reduction, with average values of less than -1.05×10^{-4} mol m^{-2}. Considering the first three categories with the lowest number of inhabitants, the factor of increase in the reduction of tropospheric VCD of NO_2 was equal to 1.28 per 50,000 inhabitants. On the other hand, it decreased slightly among the categories of 150,000 to 600,000 inhabitants, being equal to 1.03 per 50,000 inhabitants.

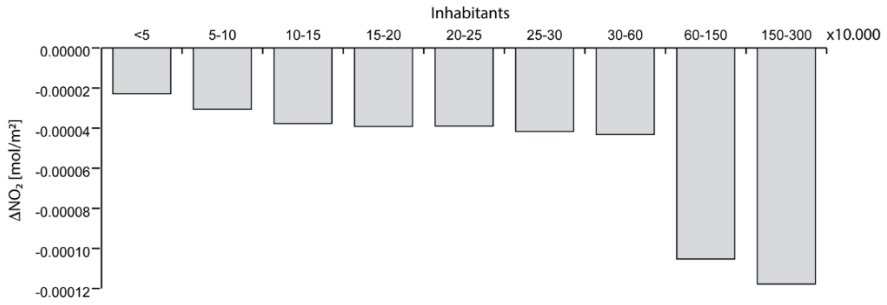

Figure 8. Number of inhabitants versus variation of tropospheric vertical column of NO_2.

The 11 cities with more than 275,000 inhabitants in Spain, are plotted in Figure 9 which shows a negative lineal relationship between population size and NO_2 reduction with a correlation coefficient equal to 0.73 (p-value 0.00004). A negative relationship was expected between population activity and NO_2 levels, where greater activity leads to a higher level. This component is one of the most important in urban air pollution, with the burning of fossil fuels such as coal, oil and gas being one of the main sources of NO_2. It is estimated that about 86% of nitrogen dioxide in European cities are caused by fossil fuels emitted from motor vehicles [65]. That means that as populations increase, NO_2 also increases. With the lockdown measures in effect there has been almost no vehicle traffic and in turn the concentration of NO_2 has been reduced.

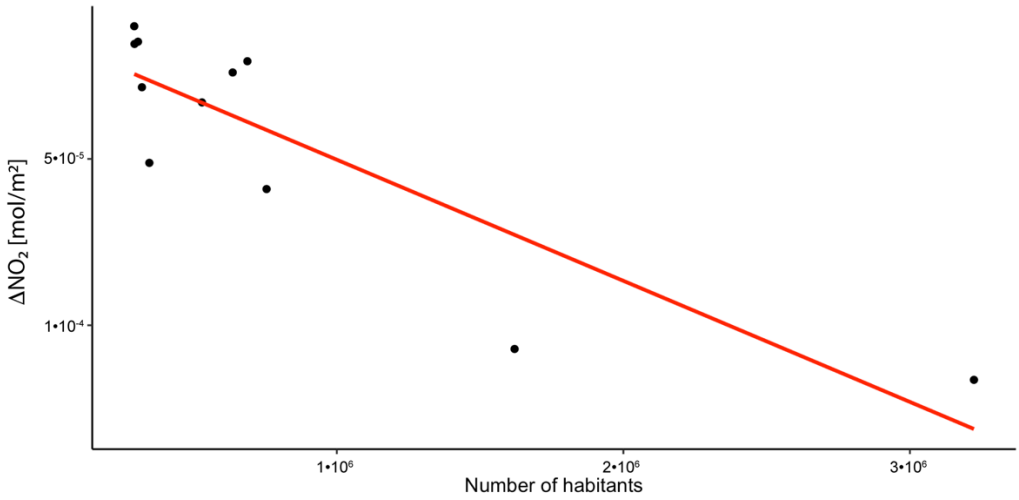

Figure 9. Number of inhabitants versus variation of tropospheric vertical column of NO_2. The red line is the fitted linear function.

4. Discussion

NO_2 concentrations in megacities exceed recommendations from the World Health Organization [13]. To control the spread of coronavirus the large majority of people have been staying at home, maintaining social distancing practices and working remotely [66]. As expected, the direct consequence of industries and transportation systems shutting down was a sudden drop in air pollutant emissions. The lockdowns have provided researchers the opportunity to set up singular experiments based on real data and not simulations to answer the question of what would happen if individual transport based on fuel combustion were removed and only those linked to public service and supply were active. Under this scenario, around the world, many cities have looked into how air quality has improved since the lockdown measures took place. Particularly in Europe, NO_2 emissions were highly reduced over northern Italy, Spain and the United Kingdom [67]. It is well known there is a positive association between NO_2 concentration and population size [68]. As in other studies in other countries [69], in Spain, NO_2 concentrations are located around urban areas, being higher as population size increases, indicating anthropogenic sources, mainly produced by vehicles. The situation caused by the SARS-CoV-2 pandemic has led, in the case of Spain, to an 80% reduction in traffic and a reduction of fuel sales by 83% [70].

Urban planners, engineers and policymakers should take the studies that have capitalized on the unique conditions presented by the pandemic

into account to promote new strategies to reduce air pollution and consolidate existing ones. To this end, it is necessary to consider how the expansion of urban areas and the complex use of land, transport patterns and socio-economic development directly factor into our living conditions. The expansion of urban areas has led to an increase in residential areas on the outskirts of cities, resulting in disproportionate distances between residential housing and places of work, generating an imbalance in transport with a high dependence on private vehicles [71]. To date, there is not a sufficient number of studies taking into account the integration of transport systems and urban planning to reduce air pollution [72,73].

Regardless of the positive impact on the reduction of air pollutants, climate effects are still present today and should not be understood as a substitute for climate change. In this way, we would like to express that in this manuscript we characterized the changes produced on air quality during the lockdown. We have not tried to attribute specifically nor quantify the effects of the lockdown since other factors may have influenced the changes, such as meteorology and regional and long-range transport of pollutants. An in-depth analysis is required to obtain this information accurately.

In addition to the impact of lockdown measures on air quality, future work should aim to study the impact of the absence of tourists on the appearance of beaches and water quality, or the reduction of noise pollution. Moreover, the massive use of personal protective equipment such as masks or gloves has increased worldwide, and probably recycling and waste management policies should be analyzed and redesigned.

5. Conclusions

Lockdown measures due to SARS-CoV-2 have provoked a singular and unique opportunity to evaluate the contribution and impact of human activity on the environment. In this manuscript, the effect on air pollution due to the pandemic response in Spain has been shown by evaluating and analyzing the concentration of tropospheric NO_2 from 1 January to 30 April in 2019 and 2020. In this study, data from the TROPOMI on-board the Sentinel-5P satellite platform were used to analyze the spatial-temporal variation in Spain and its relationship with population size and lockdown measures.

The satellite scenes showed a high concentration of NO_2 in the city of Madrid, which has the largest number of inhabitants in Spain. Other hotspots with high concentrations of NO_2 also appeared over cities with a large number of inhabitants. Previous lockdown measures, the relationship

between the population density map of Spain and the NO_2 distribution followed the same pattern. Furthermore, as a result of the concentration of the population in very specific points within the Spanish territory and the source of NO_2, mainly related to vehicle traffic, the distribution of this pollutant presented a wide range of values in the air, clearly differentiating between areas with a high population density and those without.

Just two weeks of lockdown measures and the mobility restrictions were reflected in a reduction of NO_2, mainly in those areas with larger populations. One month later, the NO_2 reduction was more evident, and not only in the populated areas, adopting a homogeneous distribution throughout the territory. The comparison between the NO_2 concentration values before and after the lockdown measures shows a strong relationship with the number of inhabitants.

These results should be taken into account by governments and policymakers to develop effective NO_2 emissions reduction and air pollution prevention policies. These policies should be based on adopting local measures within a global project.

Author Contributions: F.-J.M.-C., A.G.-F. and J.E.M.-L. conceived and designed the experiment, F.-J.M.-C., F.P.P. and P.T.-T. performed the experiment; F.-J.M.-C., F.P.P. and P.T.-T. analyzed the data and F.-J.M.-C. wrote the paper and A.G.-F. and J.E.M.-L. collaborated in the discussion of the results and revised the manuscript. All the authors have read and approved the manuscript.

Funding: This research received no external funding.

Conflicts of Interest: The authors declare no conflict of interest.

References

1. World Health Organization Air pollution. Available online: (accessed on).
2. Gurjar, B.R.; Lelieveld, J. New Directions: Megacities and global change. *AtmEn* **2005**, *39*, 391–393.
3. CAI-Asia Center. *Indonesia: Air Quality Profile*; Clean Air Initiative for Asian Cities (CAI-Asia) Center: Pasig, Philippines, 2010.
4. Khandelwal, S.; Goyal, R.; Kaul, N.; Mathew, A. Assessment of land surface temperature variation due to change in elevation of area surrounding Jaipur, India. *Egypt. J. Remote Sens. Space Sci.* **2018**, *21*, 87–94.
5. Dadhich, P.N.; Hanaoka, S. Spatial investigation of the temporal urban form to assess impact on transit services and public transportation access. *Geo Spat. Inf. Sci.* **2012**, *15*, 187–197.
6. Ravindra, K.; Mor, S.; Ameena; Kamyotra, J.S.; Kaushik, C.P. Variation in Spatial Pattern of Criteria Air Pollutants Before and During Initial Rain of Monsoon. *Environ. Monit. Assess.* **2003**, *87*, 145–153.

7. Marsh, W.M.; Grossa, J., Jr. *Environmental Geography: Science, Land Use, and Earth Systems*, 2nd ed.; John Wiley and Sons, Ed.; John Wiley and Sons: New York, NY, USA, 2002; ISBN 0471503967.
8. Pasqua, L.A.; Damasceno, M.V.; Cruz, R.; Matsuda, M.; Martins, M.A.G.; Marquezini, M.V.; Lima-Silva, A.E.; Saldiva, P.H.N.; Bertuzzi, R. Exercising in the urban center: Inflammatory and cardiovascular effects of prolonged exercise under air pollution. *Chemosphere* **2020**, *254*, 126817.
9. Shmuel, S.; White, A.J.; Sandler, D.P. Residential exposure to vehicular traffic-related air pollution during childhood and breast cancer risk. *Environ. Res.* **2017**, *159*, 257–263.
10. Kopnina, H. Vehicular air pollution and asthma: Implications for education for health and environmental sustainability. *Local Environ.* **2017**, *22*, 38–48.
11. Tang, G.; Zhao, P.; Wang, Y.; Gao, W.; Cheng, M.; Xin, J.; Li, X.; Wang, Y. Mortality and air pollution in Beijing: The long-term relationship. *Atmos. Environ.* **2017**, *150*, 238–243.
12. He, G.; Fan, M.; Zhou, M. The effect of air pollution on mortality in China: Evidence from the 2008 Beijing Olympic Games. *J. Environ. Econ. Manag.* **2016**, *79*, 18–39.
13. World Health Organization. *WHO Air Quality Guidelines for Particulate Matter, Ozone, Nitrogen Dioxide and Sulfur Dioxide: Global Update 2005: Summary of Risk Assessment*; World Health Organization: Geneva, Switzerland, 2006.
14. UNION, P. Directive 2008/50/EC of the European Parliament and of the Council of 21 May 2008 on ambient air quality and cleaner air for Europe. *Off. J. Eur. Union* **2008**, *152*, 1–44.
15. Yebin, T.; Wei, H.; Xiaoliang, H.; Liuju, Z.; Shou-En, L.; Yi, L.; Lingzhen, D.; Yuanhang, Z.; Tong, Z. Estimated Acute Effects of Ambient Ozone and Nitrogen Dioxide on Mortality in the Pearl River Delta of Southern China. *Environ. Health Perspect.* **2012**, *120*, 393–398.
16. MacIntyre, E.A.; Gehring, U.; Mölter, A.; Fuertes, E.; Klümper, C.; Krämer, U.; Quass, U.; Hoffmann, B.; Gascon, M.; Brunekreef, B.; et al. Air Pollution and Respiratory Infections during Early Childhood: An Analysis of 10 European Birth Cohorts within the ESCAPE Project. *Environ. Health Perspect.* **2014**, *122*, 107–113.
17. Hesterberg, T.W.; Bunn, W.B.; McClellan, R.O.; Hamade, A.K.; Long, C.M.; Valberg, P.A. Critical review of the human data on short-term nitrogen dioxide (NO_2) exposures: Evidence for NO_2 no-effect levels. *Crit. Rev. Toxicol* **2009**, *39*, 743–781.
18. Ilan, L.; Cristian, M.; Gang, L.; Julie, N.; Brook J.R. Evaluating Multipollutant Exposure and Urban Air Quality: Pollutant Interrelationships, Neighborhood Variability, and Nitrogen Dioxide as a Proxy Pollutant. *Environ. Health Perspect.* **2014**, *122*, 65–72.
19. Stieb, D.M.; Burnett, R.T.; Smith-Doiron, M.; Brion, O.; Shin, H.H.; Economou, V. A New Multipollutant, No-Threshold Air Quality Health Index Based on

Short-Term Associations Observed in Daily Time-Series Analyses. *J. Air Waste Manag. Assoc.* **2008**, *58*, 435–450.

20. Filleul, L.; Rondeau, V.; Vandentorren, S.; Le Moual, N.; Cantagrel, A.; Annesi-Maesano, I.; Charpin, D.; Declercq, C.; Neukirch, F.; Paris, C.; et al. Twenty five year mortality and air pollution: Results from the French PAARC survey. *Occup. Environ. Med.* **2005**, *62*, 453–460.
21. Chen, X.; Zhang, L.; Huang, J.; Song, F.; Zhang, L.; Qian, Z.; Trevathan, E.; Mao, H.; Han, B.; Vaughn, M.; et al. Long-term exposure to urban air pollution and lung cancer mortality: A 12-year cohort study in Northern China. *Sci. Total Environ.* **2016**, *571*, 855–861.
22. Gauderman, W.J.; Avol, E.; Lurmann, F.; Kuenzli, N.; Gilliland, F.; Peters, J.; McConnell, R. Childhood Asthma and Exposure to Traffic and Nitrogen Dioxide. *Epidemiology* **2005**, *16*, 737–743.
23. Kowalska, M.; Skrzypek, M.; Kowalski, M.; Cyrys, J. Effect of NOx and NO_2 Concentration Increase in Ambient Air to Daily Bronchitis and Asthma Exacerbation, Silesian Voivodeship in Poland. *Int. J. Environ. Res. Public Health* **2020**, *17*, 754.
24. Beelen, R.; Hoek, G.; Van Den Brandt, P.A.; Goldbohm, R.A.; Fischer, P.; Schouten, L.J.; Jerrett, M.; Hughes, E.; Armstrong, B.; Brunekreef, B. Long-Term Effects of Traffic-Related Air Pollution on Mortality in a Dutch Cohort (NLCS-AIR Study). *Environ. Health Perspect.* **2008**, *116*, 196–202.
25. Eum, K.-D.; Kazemiparkouhi, F.; Wang, B.; Manjourides, J.; Pun, V.; Pavlu, V.; Suh, H. Long-term NO_2 exposures and cause-specific mortality in American older adults. *Environ. Int.* **2019**, *124*, 10–15.
26. Amorim, L.C.A.; Carneiro, J.P.; Cardeal, Z.L. An optimized method for determination of benzene in exhaled air by gas chromatography–mass spectrometry using solid phase microextraction as a sampling technique. *J. Chromatogr. B* **2008**, *865*, 141–146.
27. Ma, Y.; Richards, M.; Ghanem, M.; Guo, Y.; Hassard, J. Air pollution monitoring and mining based on sensor grid in London. *Sensors* **2008**, *8*, 3601–3623.
28. Richards, M.; Ghanem, M.; Osmond, M.; Guo, Y.; Hassard, J. Grid-based analysis of air pollution data. *Ecol. Model.* **2006**, *194*, 274–286.
29. Boubrima, A.; Bechkit, W.; Rivano, H. Optimal WSN Deployment Models for Air Pollution Monitoring. *IEEE Trans. Wirel. Commun.* **2017**, *16*, 2723–2735.
30. Patil, D.; Thanuja, T.C.; Melinamath, B.C. *Air Pollution Monitoring System Using Wireless Sensor Network (WSN) BT-Data Management, Analytics and Innovation*; Balas, V.E., Sharma, N., Chakrabarti, A., Eds.; Springer: Singapore, Singapore, 2019; pp. 391–400.
31. Yi, W.Y.; Lo, K.M.; Mak, T.; Leung, K.S.; Leung, Y.; Meng, M.L. A survey of wireless sensor network based air pollution monitoring systems. *Sensors* **2015**, *15*, 31392–31427.

32. Zheng, Z.; Yang, Z.; Wu, Z.; Marinello, F. Spatial Variation of NO_2 and Its Impact Factors in China: An Application of Sentinel-5P Products. *Remote Sens.* **2019**, *11*, 1939.
33. Nate, S. Remote-Sensing Applications for Environmental Health Research. *Environ. Health Perspect.* **2014**, *122*, A268–A275.
34. Burrows, J.P.; Weber, M.; Buchwitz, M.; Rozanov, V.; Ladstätter-Weißenmayer, A.; Richter, A.; DeBeek, R.; Hoogen, R.; Bramstedt, K.; Eichmann, K.-U.; et al. The Global Ozone Monitoring Experiment (GOME): Mission Concept and First Scientific Results. *J. Atmos. Sci.* **1999**, *56*, 151–175.
35. Bovensmann, H.; Burrows, J.P.; Buchwitz, M.; Frerick, J.; Noël, S.; Rozanov, V.V.; Chance, K.V.; Goede, A.P.H. SCIAMACHY: Mission Objectives and Measurement Modes. *J. Atmos. Sci.* **1999**, *56*, 127–150.
36. Callies, J.; Corpaccioli, E.; Eisinger, M.; Hahne, A.; Lefebvre, A. GOME-2-Metop's second-generation sensor for operational ozone monitoring. *ESA Bull.* **2000**, *102*, 28–36.
37. Levelt, P.F.; Van Den Oord, G.H.J.; Dobber, M.R.; Malkki, A.; Visser, H.; De Vries, J.; Stammes, P.; Lundell, J.O.V.; Saari, H. The ozone monitoring instrument. *IEEE Trans. Geosci. Remote Sens.* **2006**, *44*, 1093–1101.
38. Veefkind, J.P.; Aben, I.; McMullan, K.; Förster, H.; De Vries, J.; Otter, G.; Claas, J.; Eskes, H.J.; De Haan, J.F.; Kleipool, Q.; et al. TROPOMI on the ESA Sentinel-5 Precursor: A GMES mission for global observations of the atmospheric composition for climate, air quality and ozone layer applications. *Remote Sens. Environ.* **2012**, *120*, 70–83.
39. Griffin, D.; Zhao, X.; McLinden, C.A.; Boersma, F.; Bourassa, A.; Dammers, E.; Degenstein, D.; Eskes, H.; Fehr, L.; Fioletov, V.; et al. High-Resolution Mapping of Nitrogen Dioxide With TROPOMI: First Results and Validation Over the Canadian Oil Sands. *Geophys. Res. Lett.* **2019**, *46*, 1049–1060.
40. Lamsal, L.N.; Duncan, B.N.; Yoshida, Y.; Krotkov, N.A.; Pickering, K.E.; Streets, D.G.; Lu, Z.U.S. NO_2 trends (2005–2013): EPA Air Quality System (AQS) data versus improved observations from the Ozone Monitoring Instrument (OMI). *Atmos. Environ.* **2015**, *110*, 130–143.
41. Van Geffen, J.H.G.M.; Eskes, H.J.; Boersma, K.F.; Maasakkers, J.D.; Veefkind, J.P. TROPOMI ATBD of the Total and Tropospheric NO_2 Data Products. *Minist. Infrastruct. Water Manag.* **2019**. Available online: https://sentinel. esa. int/documents/247904/2476257/Sentinel-5P-TROPOMI-ATBD-NO2-data-products (accessed on 10 January 2020).
42. Curier, R.L.; Kranenburg, R.; Segers, A.J.S.; Timmermans, R.M.A.; Schaap, M. Synergistic use of OMI NO_2 tropospheric columns and LOTOS–EUROS to evaluate the NOx emission trends across Europe. *Remote Sens. Environ.* **2014**, *149*, 58–69.
43. Castellanos, P.; Boersma, K.F. Reductions in nitrogen oxides over Europe driven by environmental policy and economic recession. *Sci. Rep.* **2012**, *2*, 265.

44. Ghude, S.D.; Pfister, G.G.; Jena, C.; Van Der A., R.J.; Emmons, L.K.; Kumar, R. Satellite constraints of nitrogen oxide (NOx) emissions from India based on OMI observations and WRF-Chem simulations. *Geophys. Res. Lett.* **2013**, *40*, 423–428.
45. Streets, D.G.; Canty, T.; Carmichael, G.R.; De Foy, B.; Dickerson, R.R.; Duncan, B.N.; Edwards, D.P.; Haynes, J.A.; Henze, D.K.; Houyoux, M.R.; et al. Emissions estimation from satellite retrievals: A review of current capability. *Atmos. Environ.* **2013**, *77*, 1011–1042.
46. Wang, S.W.; Zhang, Q.; Streets, D.G.; He, K.B.; Martin, R.V.; Lamsal, L.N.; Chen, D.; Lei, Y.; Lu, Z. Growth in NOx emissions from power plants in China: Bottom-up estimates and satellite observations. *Atmos. Chem. Phys.* **2012**, *12*, 4429.
47. Kim, S.-W.; Heckel, A.; McKeen, S.A.; Frost, G.J.; Hsie, E.-Y.; Trainer, M.K.; Richter, A.; Burrows, J.P.; Peckham, S.E.; Grell, G.A. Satellite-observed U.S. power plant NOx emission reductions and their impact on air quality. *Geophys. Res. Lett.* **2006**, *33*.
48. World Economic Forum The Global Risks Report 2020. 2020. Available online: (accessed on).
49. Ye, Z.-W.; Yuan, S.; Yuen, K.-S.; Fung, S.-Y.; Chan, C.-P.; Jin, D.-Y. Zoonotic origins of human coronaviruses. *Int. J. Biol. Sci.* **2020**, *16*, 1686–1697.
50. Ahmad, T.; Khan, M.; Haroon; Musa, T.H.; Nasir, S.; Hui, J.; Bonilla-Aldana, D.K.; Rodriguez-Morales, A.J. COVID-19: Zoonotic aspects. *Travel Med. Infect. Dis.* **2020**, doi:10.1016%2Fj.tmaid.2020.101607
51. Mackenzie, J.S.; Chua, K.B.; Daniels, P.W.; Eaton, B.T.; Field, H.E.; Hall, R.A.; Halpin, K.; Johansen, C.A.; Kirkland, P.D.; Lam, S.K.; et al. Emerging viral diseases of Southeast Asia and the Western Pacific. *Emerg. Infect. Dis.* **2001**, *7*, 497–504.
52. Olsen, B.; Munster, V.J.; Wallensten, A.; Waldenström, J.; Osterhaus, A.D.M.E.; Fouchier, R.A.M. Global Patterns of Influenza a Virus in Wild Birds. *Science* **2006**, *312*, 384–388.
53. Fergus, R.; Fry, M.; Karesh, W.B.; Marra, P.P.; Newman, S.; Paul, E. Migratory Birds and Avian Flu. *Science* **2006**, *312*, 845–846.
54. Petersen, L.R.; Marfin, A.A. Shifting Epidemiology of Flaviviridae. *J. Travel Med.* **2008**, *12*, s3–s11.
55. Leviston, Z.; Leitch, A.; Greenhill, M.; Leonard, R.; Walker, I. Australians' views of climate change. *Canberra CSIRO* **2011**.
56. Price, J.C.; Walker, I.A.; Boschetti, F. Measuring cultural values and beliefs about environment to identify their role in climate change responses. *J. Environ. Psychol.* **2014**, *37*, 8–20.
57. Van Der Linden, S.L.; Leiserowitz, A.A.; Feinberg, G.D.; Maibach, E.W. The Scientific Consensus on Climate Change as a Gateway Belief: Experimental Evidence. *PLoS ONE* **2015**, *10*, e0118489.

58. Callaway, E. Time to use the p-word? Coronavirus enter dangerous new phase. *Nature* **2020**, *579*, 10–38.
59. Remuzzi, A.; Remuzzi, G. COVID-19 and Italy: What next? *Lancet* **2020**, *395*, 1225–1228.
60. Hou, C.; Chen, J.; Zhou, Y.; Hua, L.; Yuan, J.; He, S.; Guo, Y.; Zhang, S.; Jia, Q.; Zhao, C.; et al. The effectiveness of quarantine of Wuhan city against the Corona Virus Disease 2019 (COVID-19): A well-mixed SEIR model analysis. *J. Med. Virol.* **2020**, *92*, 841–848.
61. Lau, H.; Khosrawipour, V.; Kocbach, P.; Mikolajczyk, A.; Schubert, J.; Bania, J.; Khosrawipour, T. The positive impact of lockdown in Wuhan on containing the COVID-19 outbreak in China. *J. Travel Med.* **2020**, *27*, doi:10.1093/jtm/taaa037.
62. Peto, J.; Alwan, N.A.; Godfrey, K.M.; Burgess, R.A.; Hunter, D.J.; Riboli, E.; Romer, P. Universal weekly testing as the UK COVID-19 lockdown exit strategy. *Lancet* **2020**, *395*, 1420–1421.
63. Gorelick, N.; Hancher, M.; Dixon, M.; Ilyushchenko, S.; Thau, D.; Moore, R. Google Earth Engine: Planetary-scale geospatial analysis for everyone. *Remote Sens. Environ.* **2017**, *202*, 18–27.
64. Eskes, H.J.; Eichmann, K.U. *S5P Mission Performance Centre Nitrogen Dioxide [L2__NO2___]*. 2019. Available online: (accessed on).
65. Degraeuwe, B.; Pisoni, E.; Peduzzi, E.; De Meij, A.; Monforti-Ferrario, F.; Bodis, K.; Mascherpa, A.; Astorga-Llorens, M.; Thunis, P.; Vignati, E. *Urban NO_2 Atlas*; Publications Office of the European Union: Brussels, Belgium, 2019; ISBN 978-92-76-10386-8.
66. Harapan, H.; Itoh, N.; Yufika, A.; Winardi, W.; Keam, S.; Te, H.; Megawati, D.; Hayati, Z.; Wagner, A.L.; Mudatsir, M. Coronavirus disease 2019 (COVID-19): A literature review. *J. Infect. Public Health* **2020**, *13*, 667–673.
67. Ficetola, G.F.; Rubolini, D. Climate affects global patterns of COVID-19 early outbreak dynamics. *MedRxiv* **2020**, doi:10.1101/2020.03.23.20040501.
68. Zhu, Y.; Price, O.R.; Kilgallon, J.; Qi, Y.; Tao, S.; Jones, K.C.; Sweetman, A.J. Drivers of contaminant levels in surface water of China during 2000–2030: Relative importance for illustrative home and personal care product chemicals. *Environ. Int.* **2018**, *115*, 161–169.
69. Zhu, Y.; Zhan, Y.; Wang, B.; Li, Z.; Qin, Y.; Zhang, K. Spatiotemporally mapping of the relationship between NO2 pollution and urbanization for a megacity in Southwest China during 2005–2016. *Chemosphere* **2019**, *220*, 155–162.
70. De Tráfico, D.G.; Del, I.M. Evolución del Tráfico por el efecto COVID-19. Available online: http://www.dgt.es/Galerias/covid-19/Evolucion-Intensidades-dia-02-04-2020-Periodo-Coronavirus.pdf (accessed on 9 May 2020).
71. Banister, D. Energy, quality of life and the environment: The role of transport. *Transp. Rev.* **1996**, *16*, 23–35.

72. Camagni, R.; Gibelli, M.C.; Rigamonti, P. Urban mobility and urban form: The social and environmental costs of different patterns of urban expansion. *Ecol. Econ.* **2002**, *40*, 199–216.
73. Ambarwati, L.; Verhaeghe, R.; Van Arem, B.; Pel, A.J. The influence of integrated space–transport development strategies on air pollution in urban areas. *Transp. Res. Part D Transp. Environ.* **2016**, *44*, 134–146.

Conclusiones

Las características de los vehículos aéreos no tripulados por su baja altitud de vuelo, su bajo coste y gran flexibilidad, ofrecen nuevas oportunidades para las aplicaciones de agricultura de precisión aumentando la resolución espacial y temporal con datos de múltiples fuentes. Aun así, uno de los puntos débiles de los UAV comerciales y de bajo coste es hasta ahora la autonomía de vuelo, lo que implica la miniaturización máxima de la electrónica de las cargas de pago, para aumentar el rendimiento de la autonomía lo máximo posible.

A pesar de que las plataformas no tripuladas con sensores son fácilmente accesibles en la actualidad y se han usado ampliamente en una gran cantidad de proyectos con éxitos diversos, todavía es necesario seguir trabajando en el pre-procesamiento de los datos capturados por las distintas fuentes con objeto de poder realizar análisis concluyentes sobre los mismos.

Por otro lado, la reducción en tamaño de los componentes electrónicos genera problemas que son necesarios resolver con metodologías estandarizadas para su posterior aplicación sobre los cultivos agrarios. Cada tipo de sensor pasivo miniaturizado necesita de correcciones para ofrecer resultados similares a los sensores embarcados en plataformas aéreas tripuladas o satelitales. Las técnicas tradicionales de pre-procesado y corrección de captura de datos se están actualizando por procedimientos más avanzados a partir de modelos matemáticos que explican y corrigen su comportamiento.

En general, como se ha comprobado con los resultados obtenidos en el capítulo 1 de la tesis, una nueva metodología de pre-procesamiento de datos ha sido aplicada a los datos termográficos capturados por el sensor embarcado en el UAV. Una vez que los datos han sido pre-procesados se han aplicado metodologías clásicas para las correcciones atmosféricas, que en este caso si han surtido efecto. En definitiva, los datos capturados por plataformas UAV menores de 25 kg con pequeños sensores necesitan de un pre-procesado para posteriormente aplicar sobre ellos técnicas clásicas de teledetección.

Cada vez es más importante divulgar este tipo de pre-procesado de datos en todos los ámbitos, académico, empresarial, industrial, etc. Debido a la velocidad a la que avanza la tecnología, es necesario que se transfiera

de forma rápida este conocimiento como se ha visto en el capítulo 2, para que las técnicas aplicadas sobre los datos capturados de UAV sean las correctas e incorporen esta fase en el procesamiento.

Una vez que se han corregido los datos capturados por estos sensores de UAV a partir de este nuevo concepto para la modelización de la deriva térmica, el flujo de trabajo para generar productos a través de teledetección sigue una estructura fija y estandarizada que permite a partir de datos capturados por un sensor y datos terreno, generar modelos predictivos.

Finalmente, en el capítulo 3 de la tesis, se ha seguido un flujo de trabajo para la predicción de variables ambientales desde satélite de forma análoga a como se realiza a partir de datos capturados por sensores de UAV, una vez pre-procesados. Esto es de gran importancia ya que identifica un flujo de trabajo estándar para teledetección donde la única diferencia entre el procesado de datos desde UAV y satélite, sólo implica un pre-procesado inicial en los datos capturados desde plataformas no tripuladas.